The Astrophysical Journal Supplement Series, 224:3 (36pp), 2016 May doi:10.3847/0067-0049/224/1/3

LIGHT CURVES OF 213 TYPE Ia SUPERNOVAE FROM THE ESSENCE SURVEY

G. Narayan[1,2,3], A. Rest[4], B. E. Tucker[5], R. J. Foley[6], W. M. Wood-Vasey[7], P. Challis[2], C. Stubbs[2,3], R. P. Kirshner[2], C. Aguilera[8], A. C. Becker[9], S. Blondin[10], A. Clocchiatti[11,26], R. Covarrubias[9], G. Damke[12], T. M. Davis[13], A. V. Filippenko[14], M. Ganeshalingam[14], A. Garg[2], P. M. Garnavich[15], M. Hicken[3], S. W. Jha[16], K. Krisciunas[17], B. Leibundgut[18], W. Li[14,27], T. Matheson[1], G. Miknaitis[19], G. Pignata[20], J. L. Prieto[21], A. G. Riess[4,22], B. P. Schmidt[5], J. M. Silverman[23], R. C. Smith[7], J. Sollerman[24], J. Spyromilio[18], N. B. Suntzeff[17], J. L. Tonry[25], and A. Zenteno[8]

[1] National Optical Astronomy Observatory, 950 North Cherry Avenue, Tucson, AZ 85719, USA; gnarayan@noao.edu
[2] Harvard-Smithsonian Center for Astrophysics, 60 Garden Street, Cambridge, MA 02138, USA
[3] Deptartment of Physics, Harvard University, 17 Oxford Street, Cambridge, MA 02138, USA
[4] Space Telescope Science Institute, 3700 San Martin Drive, Baltimore, MD 21218, USA
[5] The Research School of Astronomy and Astrophysics, Australian National University, Mount Stromlo Observatory, via Cotter Road, Weston Creek, ACT 2611, Australia
[6] Department of Astronomy, University of Illinois at Urbana-Champaign, 1002 W. Green Street, Urbana, IL 61801, USA
[7] Department of Physics and Astronomy, University of Pittsburgh, Pittsburgh, PA 15260, USA
[8] Cerro Tololo Inter-American Observatory, National Optical Astronomy Observatory, Casilla 603, La Serena, Chile
[9] Department of Astronomy, University of Washington, Box 351580, Seattle, WA 98195-1580, USA
[10] Aix Marseille Université, CNRS, LAM (Laboratoire dÁstrophysique de Marseille) UMR 7326, F-13388, Marseille, France
[11] Pontificia Universidad Catolica de Chile, Instituto de Astrofisica, Casilla 306, Santiago 22, Chile
[12] Department of Astronomy, University of Virginia, Charlottesville, VA 22904-4325, USA
[13] School of Mathematics and Physics, University of Queensland, Brisbane, QLD 4072, Australia
[14] Department of Astronomy, 601 Campbell Hall, University of California, Berkeley, CA 94720-3411, USA
[15] Department of Physics, University of Notre Dame, 225 Nieuwland Science Hall, Notre Dame, IN 46556-5670, USA
[16] Department of Physics and Astronomy, Rutgers, The State University of New Jersey, Piscataway, NJ 08854, USA
[17] Department of Physics and Astronomy, Texas A & M University, College Station, TX 77843-4242, USA
[18] European Southern Observatory, Karl-Schwarzschild-Strasse 2, D-85748 Garching, Germany
[19] Fermilab, P.O. Box 500, Batavia, IL 60510-0500, USA
[20] Departamento de Ciencias Fisicas, Universidad Andres Bello, Avda. Republica 252, Santiago, Santiago RM, Chile
[21] Astronomy Nucleus, Faculty of Engineering, Universidad Diego Portales, Ejército 441, Santiago, Santiago RM, Chile
[22] Johns Hopkins University, 3400 North Charles Street, Baltimore, MD 21218, USA
[23] Department of Astronomy, University of Texas, Austin, TX 78712-0259, USA
[24] Oskar Klein Centre, Department of Astronomy, AlbaNova, Stockholm University, SE-10691, Stockholm, Sweden
[25] Institute for Astronomy, University of Hawaii, 2680 Woodlawn Drive, Honolulu, HI 96822, USA
[26] Millennium Institute of Astrophysics, Chile
Received 2015 May 26; accepted 2015 December 22; published 2016 May 6

ABSTRACT

The ESSENCE survey discovered 213 Type Ia supernovae at redshifts $0.1 < z < 0.81$ between 2002 and 2008. We present their *R*- and *I*-band photometry, measured from images obtained using the MOSAIC II camera at the CTIO Blanco, along with rapid-response spectroscopy for each object. We use our spectroscopic follow-up observations to determine an accurate, quantitative classification, and precise redshift. Through an extensive calibration program we have improved the precision of the CTIO Blanco natural photometric system. We use several empirical metrics to measure our internal photometric consistency and our absolute calibration of the survey. We assess the effect of various potential sources of systematic bias on our measured fluxes, and estimate the dominant term in the systematic error budget from the photometric calibration on our absolute fluxes is ∼1%.

Key words: cosmology: observations – methods: data analysis – supernovae: general – surveys

1. INTRODUCTION

We present the calibrated photometry of 213 Type Ia supernovae (SN Ia) measured by the Equation of State: Supernovae trace Cosmic Expansion (ESSENCE) survey between 2002 and 2008. Our report more than doubles the sample presented by Miknaitis et al. (2007) and Wood-Vasey et al. (2007). We have made a significant effort to improve the photometric calibration of the survey. As ESSENCE observed in only two passbands, our measurements of luminosity distance are strongly correlated with extinction in the host galaxy of the SN Ia and are very sensitive to the systematic error budget from photometry. In particular, the light curves in this work are computed using data taken only with the 4 m Blanco Telescope at the Cerro Tololo Inter-American Observatory, eliminating cross-telescope systematics present in the calibration by Miknaitis et al. (2007). A companion work (B. E. Tucker et al. 2014, in preparation) will report on properties of the host galaxies of our SN Ia sample. In future work, we will use this sample along with low-redshift SN Ia from the literature to perform a full cosmological analysis and improve constraints on the nature of the dark energy.

Since the discovery of the luminosity–width–color relation (Phillips 1993), SN Ia have been our most precise standardizable candles at cosmological distances. The initial Calán-Tololo sample of 29 SN in 4 colors (Hamuy et al. 1996) enabled the development of various algorithms capable of correcting the dispersion in the intrinsic brightness of SN Ia, and inferring the luminosity distances to ∼10% per object

[27] Deceased 2011 December 12.

(Riess et al. 1996; Phillips et al. 1999; Goldhaber et al. 2001). These light curve fitters have been refined as the size of the nearby sample has increased and its photometric precision has improved; current algorithms can determine the luminosity distance to well observed SN Ia to ∼5% (Guy et al. 2007; Jha et al. 2007; Conley et al. 2008; Mandel et al. 2011).

The distance moduli derived for these SN Ia indicated that the universe is *accelerating* (Riess et al. 1998; Perlmutter et al. 1999). SN Ia observations have remained our most sensitive cosmological probe of the expansion history. The accelerating expansion has been modeled by introducing a fluid with negative pressure, called the dark energy, into the Friedmann equation:

$$h(a)^2 = h_0^2\left(\frac{\Omega_M}{a^3} + \frac{\Omega_\nu}{a^4} + \frac{\Omega_k}{a^2} + \Omega_{\rm DE}\exp[3(1+w)]\right), \quad (1)$$

where h is the Hubble parameter, $h_0 = H_0/100$ km s^{-1} Mpc^{-1}, a is the scale factor, and Ω is the total energy density of matter (M), photons (ν), curvature (k), and the dark energy (DE), respectively. Several groups have focused on measuring the ratio of pressure to density—the equation of state of this fluid, $w = P/(\rho c^2)$—to distinguish between different models of the dark energy.

High-redshift SN Ia surveys (Riess et al. 2007; Wood-Vasey et al. 2007; Guy et al. 2010; Betoule et al. 2014; Sako et al. 2014) have independently reported measurements of w consistent with -1, in good agreement with a classical cosmological constant. However, despite the rapidly growing number of SN Ia, the precision of the measurement of w has stubbornly remained at the 10% level, dominated by various sources of systematic uncertainty. Several groups have attempted to reduce the effect of systematic errors in SN Ia measurements on the dark energy figure of merit (FoM; Albrecht et al. 2006), by either incorporating new sources of data, or improving the calibration of existing data.

Early work by Krisciunas et al. (2000) demonstrated uniformity in the evolution of near infrared (NIR) colors of SN Ia, and the potential of NIR measurements for cosmology (Krisciunas et al. 2004). Using increasingly large and better calibrated samples of nearby SN Ia with JHK_s measurements, Wood-Vasey et al. (2008), Mandel et al. (2009), and Barone-Nugent et al. (2012) have shown that the NIR light curves of SN Ia span a smaller range in luminosity than in the optical. Because distance moduli derived from NIR measurements are less susceptible to host galaxy dust absorption, the residual scatter in a Hubble diagram generated from infrared light curves alone is comparable to the scatter derived from *light-curve-shape-corrected* optical data. Consequently, high-z surveys have increasingly attempted to probe further into the rest-frame infrared. Freedman et al. (2009) presented the first IR Hubble diagram to $z \sim 0.7$, but were limited by a relatively small sample size, systematic uncertainties in their photometric calibration, and the difficulty of obtaining IR data at high-z, where it is redshifted to even longer wavelengths. Future high-redshift surveys, such as RAISIN (R.P. Kirshner—*Hubble Space Telescope (HST)* Proposal 13046), will provide valuable high-redshift SN Ia measurements that probe the rest-frame NIR.

Kelly et al. (2010) illustrated that in addition to demographic differences between SN Ia from passive and star-forming hosts, the Hubble diagram residuals are correlated with derived host galaxy size and stellar mass. This correlation indicates that the empirical luminosity shape relations employed by SN Ia light curve fitters do not fully account for the spread in intrinsic luminosity. In an effort to reduce this dispersion, Lampeitl et al. (2010) employed a simple linear correction based on host galaxy stellar mass and found an improvement in statistical fit to the SN Ia measurements. Sullivan et al. (2010) used different SN Ia absolute magnitudes for high- and low-mass hosts in their cosmological fits and found a significant improvement in χ^2 over using a relation expressed as a function of host galaxy stellar mass.

However, although metallicity, extinction properties, and specific star formation rate correlate with host galaxy mass, the fundamental relation underlying this correlation with SN Ia luminosity is not well understood. These relations may be an artifact of the treatment of SN Ia color by light curve fitters; Scolnic et al. (2014a) found that the strength of correlation of the host galaxy properties with Hubble residual was reduced by ∼20% when SN Ia are treated as having an intrinsic color scatter for a fixed luminosity distance, rather than an achromatic scatter in peak luminosity. In addition, there are challenges in deriving host galaxy properties from broadband optical photometry at high redshift in a manner that does not introduce additional systematic uncertainty into SN Ia measurements. ESSENCE has undertaken a significant effort to determine host galaxy morphology and properties for our sample, to appear in B. E. Tucker et al. (2014, in preparation).

Several authors (Wang et al. 2009; Blondin et al. 2011; Foley & Kasen 2011; Nordin et al. 2011; Walker et al. 2011; Silverman et al. 2012) have found that measurements from spectra of SN Ia correlate with the residual intrinsic color dispersion after light curve shape correction. They further find that these measurements, typically derived from pseudo equivalent widths of Ca or Si, can be used to improve the precision of distance moduli, although Blondin et al. (2011) find that the improvement is not statistically significant ($<2\sigma$). While promising, this approach is limited by the need for high signal-to-noise ratio (S/N) spectra of SN Ia. Additionally, the dependence on measuring the Si II 6355 Å feature limits its use at high-z, where the redshifted Si features are often not covered by the high-throughput, low-dispersion spectrographs used by SN Ia surveys.

Surveys such as ESSENCE, the Supernova Legacy Survey (SNLS), the Sloan Digital Sky Survey (SDSS), and the Panoramic Survey Telescope and Rapid Response System (Pan-STARRS) have now produced well over a thousand well sampled SN Ia light curves that span the redshift range over which the transition from cosmic deceleration to acceleration occurred. The crucial measurement for characterizing the nature of dark energy is mapping out luminosity distance versus redshift to constrain the parameters of Equation (1). The precision of photometric calibration is now the dominant term of the SN Ia survey systematic error budget. Wood-Vasey et al. (2007) found that systematic uncertainties from the photometry alone could lead to an ∼4% change in w. Exploiting the improved statistics from these large samples requires a corresponding improvement in the photometric calibration across diverse instruments, detectors and filters.

The most important aspect of this calibration challenge is to establish a well grounded understanding of flux measurements made in different broad optical passbands. This in turn requires adopting a spectrophotometric standard, which serves as the metrology basis for relating fluxes across the bands being used. In essence, we need to be able to distinguish cosmological

evolution in luminosity-distance-redshift relation from cross-band calibration issues.

There are two methods in use or in development for flux calibration at CCD wavelengths.

1. Adopt an astrophysical source, particularly Vega, as a celestial transfer standard, with ground-based blackbody emitters as the fundamental calibration sources. This is a long-standing method, and serves as the basis for Vega-based magnitudes (Oke & Schild 1970; Hayes & Latham 1975), and underpins the Landolt (1992) standard star network.
2. Use well-calibrated laboratory standards (such as silicon photodiodes from NIST) as the foundational metrology layer, and measure the system throughput in comparison to these devices. This was the approach explored advocated by Stubbs & Tonry (2006) and is now in various stages of implementation by Pan-STARRS (Tonry et al. 2012; Rest et al. 2014), SNLS (Regnault et al. 2009), the joint efforts of SDSS and SNLS (Betoule et al. 2013, 2014), and the Dark Energy Survey (DES) and the Large Synoptic Survey Telescope (LSST).

While the first method is well established, SN Ia surveys require a higher level of precision than is possible with existing standard star networks. The second method is still nascent, and systems to measure the atmospheric component of the throughput are under active development (Albert et al. 2014). No purely laboratory-standard-based magnitude system yet exists. Several surveys, including ESSENCE, have elected to use a combination of both methods; the first to determine the absolute flux calibration, and the second to determine precise relative system throughputs.

Kessler et al. (2009) demonstrated that measurements of w are extremely sensitive to the calibration of the U band at low redshift: inclusion of rest-frame U-band data at all redshifts causes a 0.12 mag shift in distance moduli, corresponding to an enormous 0.3 change in the equation of state parameter, w. The U-band anomaly might arise from differences between the spectral energy distribution (SED) of SN Ia that correlate with host galaxy properties or between objects at low and high redshift (Foley et al. 2012; Maguire et al. 2012). Additionally, U-band measurements of the same nearby SN Ia from different telescopes often exhibit differences that are inconsistent with the stated photometric uncertainties and system throughput measurements. Krisciunas et al. (2013) have demonstrated that careful modeling of the U-band transmission with appropriate S-corrections can resolve the differences between SN Ia measurements. The size of the systematics associated with the U-band, however, has led most high-z surveys to down weight, or discard rest-frame UV observations.

Larger, more precisely calibrated nearby samples (Ganeshalingam et al. 2010; Stritzinger et al. 2011; Hicken et al. 2012), along with better calibration of high-z SN Ia surveys, offer the most direct path to reducing the systematic uncertainty on the equation of state parameter of the dark energy. Wide-field deep surveys such as Pan-STARRS and DES will obtain SN Ia measurements over $0 < z < 1.2$ (Rest et al. 2014), further reducing systematic uncertainties from photometry by avoiding any errors associated with cross-telescope calibration and weakening the sensitivity of w to the overall photometric calibration of the survey (Scolnic et al. 2014b). Recognizing the need for precision calibration to reduce systematics (Stubbs & Tonry 2006; Tucker et al. 2007), and following the example set by the SDSS (Ivezić et al. 2007; Padmanabhan et al. 2008), current surveys have undertaken ambitious calibration programs. These efforts combine high-precision measurements of system throughput calibrated to laboratory standards, with atmospheric data and repeated observations of stellar standards to obtain <1% photometry over much of the sky (Stubbs et al. 2010; Schlafly et al. 2012; Tonry et al. 2012). This work details the calibration of the ESSENCE survey, with a focus on minimizing the systematic error budget from photometry.

Table 1
Primary ESSENCE Fields

Field	R.A. (J2000)	decl.	Number of Images
	h m s	° ′ ″	
waa	23:27:27	−09:51:00	172
wbb	01:12:00	−00:20:17	275
wcc	02:07:41	−04:55:00	289
wdd	02:28:36	−08:24:17	293

We provide a brief overview of the ESSENCE survey in Section 2, followed by our photometric data reduction and calibration in Section 3. We discuss our spectroscopic follow up and classification is Section 4. We illustrate our SN Ia light curves, compare and contrast our methodologies for light curve fitting, and detail the properties of the full ESSENCE six-year sample in Section 5. Our photometric error budget from various sources with systematic uncertainty is detailed in Section 6. We conclude in Section 7. The appendices contain further information on the computation of illumination corrections, the properties of the CTIO Blanco natural magnitude system employed in this work, tables containing the photometry of ESSENCE SN Ia and likely SN Ia without spectroscopic confirmation (hereafter, "Ia?") objects during the year of discovery, and light curve fit parameters using the two most common methodologies.

2. THE ESSENCE SURVEY

Previous ESSENCE publications have described the survey strategy, fields, data processing (Miknaitis et al. 2007, hereafter M07), spectroscopic selection criteria and follow up (Matheson et al. 2005; Foley et al. 2009), performed a preliminary cosmological analysis (Wood-Vasey et al. 2007, hereafter WV07), and scrutinized exotic cosmological models (Davis et al. 2007). The SN Ia search was carried out on the CTIO 4 m Blanco telescope (hereafter Blanco) over 197 half-nights in dark and graytime between September and January from 2002 to 2008. Science images were obtained using the 64 Mega pixel MOSAIC II camera with an Atmospheric Dispersion Corrector (ADC) through two primary filters (denoted R and I) similar to Cousins R_C and I_C. The field of view of the system is 0.36 deg^2 on the sky at the $f/2.87$ prime focus.

The imager consists of eight 2k × 4k CCDs arranged in two rows of four. Each CCD is bisected along its length, and each section is read out in parallel, resulting in 16 amplifier images for every science exposure. Readout times are approximately 100 s. Each pixel subtends 0.″27 at the center of the field. Optical distortions cause a radial variance of ∼8% in the pixel scale.

The survey covered a set of four primary fields (listed in Table 1, together with the number of times each field was observed), each consisting of eight sub-fields, clustered spatially. Fields were selected to be equatorial but outside the Galactic and ecliptic planes, in regions with low Milky Way extinction and minimal IR cirrus, and with coverage from existing surveys (including SDSS, the NOAO Deep Wide-Field Survey, and the Deep Lens Survey) where possible. The fields were spaced to ensure that science images could be taken at low airmass. Fields were divided into two sets and each set was imaged in both filters every other observing night, resulting in a typical cadence of four days. Science frames are exposed for 200 s in *R* and 400 s in *I*. The original *I* filter (NOAO code c6005) sustained significant damage on 2002 November 10, severely degrading the image quality of *I*-band data in CCDs 1 and 2 (amplifiers 1–4). The filter was replaced on 2003 May 25. CCD 3 failed shortly before the start of the 2003 observing season, resulting in a 12.5% loss in efficiency until it was replaced in 2004.

Survey images were reduced at CTIO using the "`photpipe`" pipeline developed for use on the CTIO Blanco by the SuperMACHO survey (Rest et al. 2005; Garg et al. 2007; Miknaitis et al. 2007) that operated contemporaneously with the ESSENCE survey. Each science image was calibrated and aligned with a fixed astrometric grid. We subtracted a reference template for each field, constructed using deep images from previous observations. Point-spread function (PSF) photometry from the resulting difference image was combined to identify sources that had varied over multiple epochs, while eliminating sources of contamination such as difference image artifacts and diffraction spikes from saturated stars. With limited time for spectroscopic follow up observations, we were forced to employ various cuts and selection criteria in order to determine the most promising candidates.

The spectroscopic follow-up observations of ESSENCE candidates is described in Section 4. All candidates were visually inspected to classify them and obtain redshifts. We produced a preliminary reduction of all spectra in real time, using standard `IRAF`[28] routines, and some custom `IDL` routines to facilitate data processing for the various instruments. Estimates of the redshift and classification were obtained on site using `SNID` (Blondin & Tonry 2007). When preliminary classifications were unclear, we relied on the experience of the observers to determine if additional spectroscopic follow up was warranted. Fields containing candidates with a clear classification as SN Ia were followed for the remainder of the observing season. Following survey operations, all data were transferred, initially to the Hydra Computing Cluster maintained by the Smithsonian Institution, and later to the Odyssey Compute Cluster hosted by the Research Computing Group at Harvard University for the analysis presented in this paper. All data is also available through the NOAO archive.[29]

3. DATA REDUCTION

3.1. Image De-trending

The eight CCDs of MOSAIC II were read out in pairs, through two amplifiers per chip, by four Arcon controllers. The cross-talk between the amplifiers is subtracted using the *xtalk* task from the *mscred* package for IRAF. All CCD images are de-biased and trimmed and masking was applied to bad pixels and columns. The mask is propagated through all subsequent reduction stages.

All science images are flat-field-corrected using dome flats. These flats accurately corrected for pixel-to-pixel variations but large-scale variations were introduced as a result of uneven illumination of the dome screen and stray light paths in the optical system. While the precision obtained from dome flat images alone is suitable for many projects, we required higher precision for SN Ia cosmology and strived to minimize potential systematic errors in our photometry. We therefore accounted for large-scale illumination variation by constructing an illumination correction from the science images, as described below.

We applied the nightly dome flat image to all science images to construct a temporary preliminary flattened image. The resulting images were masked to remove contamination from all astrophysical sources, normalized to have the same sky value, and then averaged. The derived calibration image was inverted, smoothed with a large kernel, and scaled to have a mean of unity. This illumination correction was applied to the dome flat images to take out residual large-scale gradients. The science images were reprocessed with this final flat-field image.

To estimate the night-to-night stability of the illumination correction, we took the ratio of the correction image between different nights of a single run—a period of time during which MOSAIC II was continuously mounted on the telescope, typically one lunation. We found that the gradient pattern (a representative example is shown in Figure 1) was very stable within a lunar cycle. The standard deviation of the ratio without sigma clipping was typically less that 0.1%, and the absolute value of the maximum difference between the ratio and the average of the ratio image was <0.003. Therefore, on nights with few science images of sparse fields or with excess stray light—either from insufficient baffling or around full moon—we exploited the stability of the gradient pattern to estimate the illumination correction from nearby nights. This estimation and temporal stability of the illumination corrections is examined in further detail in Appendix A.

Surveys that use master flats constructed for each run are susceptible to systematic trends, such as long period variations in amplifier gain. By contrast, our procedure avoids such effects: science frames were normalized with nightly flat frames and primarily used illumination corrections determined from the same, or at the least extrapolated only from nearby, nights.

3.2. Astrometric Calibration

In order to construct difference images to search for and measure the flux of variable and transient objects, we first imposed a consistent astrometric solution and warped all the science images to a consistent pixel coordinate system. The transformation between the local image pixel coordinate system and the FK5 World Coordinate System is dominated by optical distortions that are well described by a low-order polynomial in radius from the field center. We determined the polynomial terms of the distortion function from images of dense LMC fields using the `IRAF` task, `msctpeak`. The distortion terms were used in combination with the `IRAF` task `msccmatch` to derive a WCS solution for each field. The distortion terms were

[28] `IRAF` is distributed by the National Optical Astronomy Observatory, which is operated by AURA under cooperative agreement with the NSF.
[29] http://archive.noao.edu/nsa/

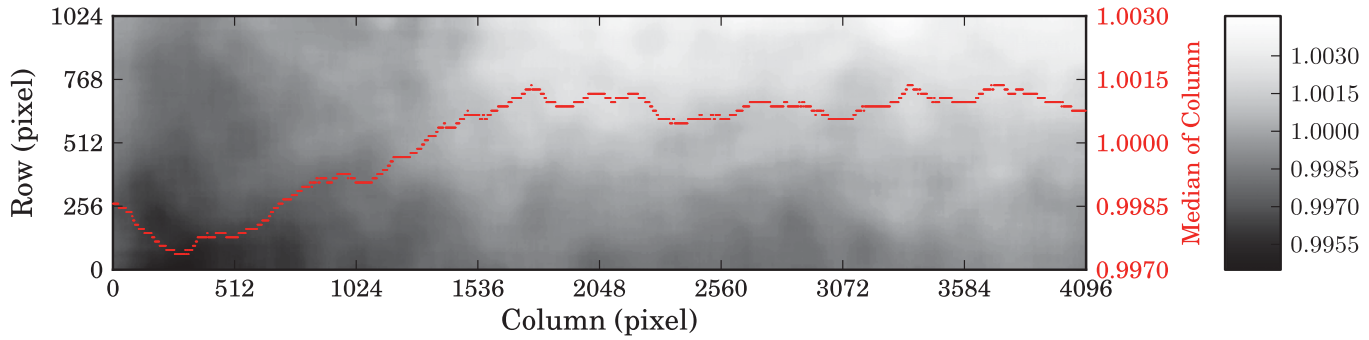

Figure 1. Representative *R*-band illumination correction for amplifier 6 of the MOSAIC II. The primary structure in the illumination correction is a ∼0.5% gradient from left to right and top to bottom. The median value of each column is indicated in red. The bar at right indicates the grayscale values.

re-computed monthly as they vary over timescales of six months. If left uncorrected, this variation would introduce systematic offsets at the ∼0.″01 level.

With the distortion modeled, the astrometric solution for any image with the equatorially mounted Blanco reduces to determining the linear rotation matrix with respect to the center. We used the `IRAF` task `mscmatch` from the `mscred` package to match pixel coordinates for objects in the image to an existing catalog of the field with precise astrometry. We generated an initial astrometric solution for the survey using reference catalogs derived from the Sloan Digital Sky Survey DR7 (Abazajian et al. 2009) wherever possible, and defaulting to astrometry from the USNO CCD Astrograph catalog 2 (UCAC; Zacharias et al. 2004) where SDSS coverage was unavailable. As the SDSS is itself tied to the UCAC, and as we only require precise *relative* astrometric calibration to precisely position the PSF and measure flux, errors caused by the differences of the astrometric solution between the two different reference catalogs are negligible. We used this initial solution to generate secondary astrometric catalogs using our multiple observations of each field.

Finally, we used the astrometric solution and the `SWarp` (Bertin et al. 2002) package to re-sample each image to a common pixel coordinate system using a flux-conserving, Lanczos-windowed sinc kernel. We generated weight maps for each image to account for the change in the noise properties produced by re-sampling. Some covariance between pixels is introduced as a result of the re-sampling process and we accounted for it during difference imaging.

3.3. Flux Measurement

We used the `DoPHOT` photometry package (Schechter et al. 1993) to identify and measure sources within the warped images. `DoPHOT` is appropriate for point source photometry. B. E. Tucker et al. (2014, in preparation) will report on photometry of extended sources.

3.4. Photometric Calibration

High-redshift SN Ia surveys typically report observations in their natural photometric system, relating magnitudes to measured flux via:

$$m_{T,i} = -2.5\log_{10}(\phi_{\mathrm{ADU},T,i}) + \mathrm{ZP}_{T,i}, \quad (2)$$

where m is the natural magnitude, ϕ the measured flux, and $\mathrm{ZP}_{T,i}$ is the instrumental zero point of the image, i, observed through passband T.

Natural magnitudes have several advantages: they allow surveys to schedule observations in different passbands independently, as the SN Ia colors at every epoch are not needed, and they avoid the additional photometric errors that arise from converting the observed supernova flux to a standard system. These transformations are non-trivial, as the simple linear transformations derived for stars are not directly applicable to SN Ia with their more complex SEDs. However, as these measurements are reported in a non-standard magnitude system, surveys must establish a network of stellar calibrators in the natural system of the telescope to derive accurate and precise zero points. In addition, an accurate model of the survey throughput in each passband is required so measurements in the natural system can be compared to synthetic fluxes generated from models derived from SN Ia measurements at low-redshift in the standard system. We have developed various metrics to quantify our internal photometric consistency, and verified our zero point consistency using the SDSS. We detail the improvements to the photometric calibration for the survey in the next subsections.

3.4.1. Aperture Corrections

The extended aureole of astrophysical objects has a surface brightness profile that roughly follows r^{-2}, and a large fraction of the flux is outside the seeing disk. Thus, an aperture larger than the seeing disk is necessary for the enclosed flux to be a reliable estimator of the true source flux. However, the larger the aperture, the higher the error from sky subtraction, and the higher the probability of enclosing contaminating sources. We follow the standard technique of addressing this trade off by measuring the flux in a fixed aperture, and determining an aperture correction to correct for its finite size.

Accurate aperture corrections are critical for establishing a consistent photometric system across the survey. We have significantly refined the algorithm used to generate aperture corrections for images. For each sub-field, we identified several isolated objects (typically 10–25 per amplifier) with $\mathrm{S/N} > 20$ that are consistent with a point-source PSF in multiple images. We took care to eliminate instances where we found flux measurements from isolated, but non-stellar objects in the growth curves computed for M07. We measured the flux of each star using aperture radii from 5 to 40 pixels, accounting for the weight map and any flux lost to masked pixels. We constructed differential growth curves for each image (a representative example is provided in Figure 2). The growth curves of individual stars that indicate contamination by a secondary source (cosmic rays, stray reflections, streaks) were

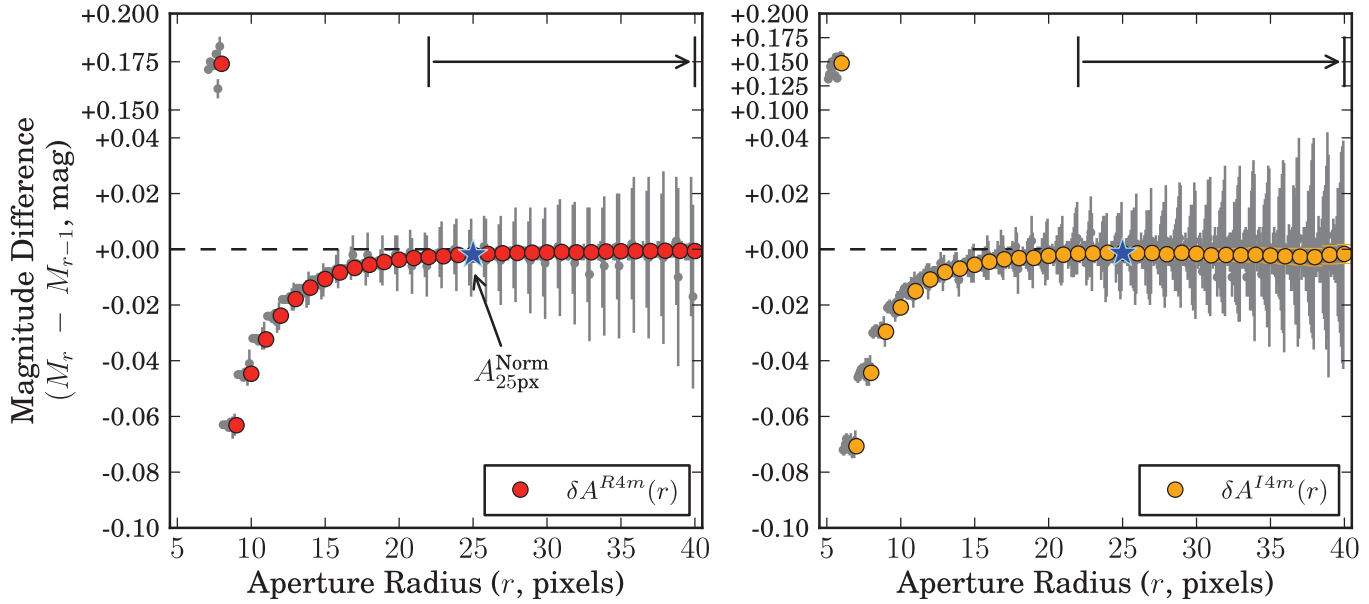

Figure 2. Typical differential curves of growth for *R* (left, red) and *I* (right, orange) on 20071103, for amplifier 4 (both randomly selected). The point at the smallest physical aperture is the difference between the DoPHOT magnitude of the object and magnitude with an aperture radius of 5 pixels. We have used a piecewise *y*-axis scale to show the full range of the data without compressing local variations. We have plotted the individual isolated stars in gray. We offset each individual star slightly from the aperture through which the flux is measured along the $-x$ direction for clarity. We checked that the growth curve is consistent with a constant for apertures larger than 22 pixels, indicated by vertical lines with an arrow in between. Errors in the average measurement at each aperture, δA, are typically smaller than the plot symbols. We propagated the covariance matrix between apertures to determine the final aperture correction at a radius of 25 pixels (indicated with a blue star, and labeled in the left panel).

removed. If more than 25% of the stars were clipped, the aperture correction for the image was flagged "bad." We checked that the growth curves asymptotically approached a constant value for all apertures larger than 22 pixels, and flagged those that did not. We measured the total aperture correction to an aperture radius of 25 pixels, or $\sim 13\farcs5$ in diameter, chosen to effectively enclose most of the flux of each object for all ESSENCE images, which have a typical FWHM of the PSF of $\sim 1\farcs2$ in both passbands (see Figure 3).

3.4.2. Choice of Standard Star Network and a Fundamental Spectrophotometric Standard

While several standard stellar catalogs report broadband magnitudes in different photometric systems through a range of passbands (Landolt 1983; Stetson 2000; Ivezić et al. 2007; Landolt & Uomoto 2007), the standard star network of Landolt (1992), extended by Stetson (2005), remains the most obvious choice to tie to the Johnson-Morgan-Cousins photometric system. The R_C and I_C Cousins filters are broadly similar to those used on the Blanco (see Figure 4), and the magnitudes reported by low-redshift SN Ia surveys are converted into the Johnson system using observations of the Landolt network stars. This allows us to minimize systematic uncertainties when comparing our data to the nearby sample.

The choice of standard star network and the transformation equations derived between the natural and standard system also play a critical role in determining the absolute throughput of each passband. This calibration enables SED models of SN Ia generated from low-redshift observations to be converted into the Blanco natural magnitude system via:

$$m_T = -2.5\log_{10}\left(\int F(\lambda)T(\lambda)\frac{\lambda}{hc}\,{\rm d}\lambda\right) + {\rm ZP}_T. \qquad (3)$$

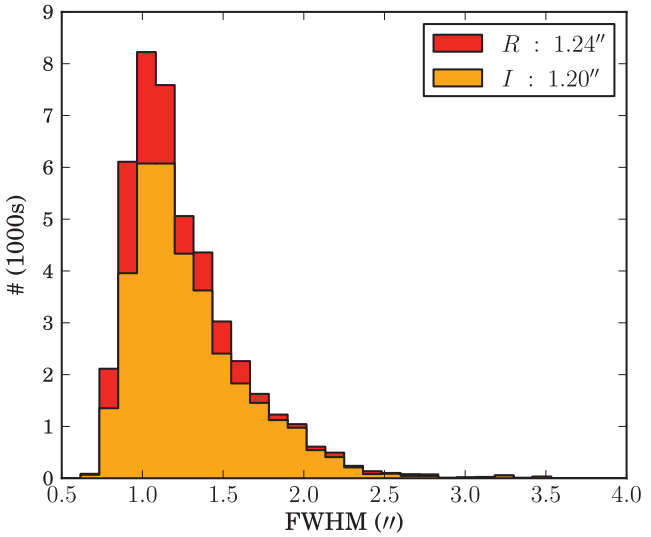

Figure 3. FWHM Distribution of *R* and *I* science images from the survey. The mean FWHM is $1\farcs24$ for the *R* band and $1\farcs2$ for *I*.

This equation is inverted to determine the zero point, $\rm ZP_T$, for the full optical system (detector, optics, filter, and atmosphere) with dimensionless total photon efficiency, $T(\lambda)$, using a star with a well-measured SED, $F(\lambda)$[30], whose magnitudes, m_T, are known in the natural system—a "fundamental spectrophotometric standard."

[30] The formalism employed throughout this work represents SEDs as power per unit wavelength as a function of wavelength, while the system throughput is represented as a dimensionless photon efficiency. The former is typically provided in erg s^{-1} cm^{-2} $Å^{-1}$. If the system throughput is provided in erg $Å^{-1}$, then the extra factor of the inverse energy, $\frac{\lambda}{hc}$, must be dropped to account for the Jacobian of the transformation.

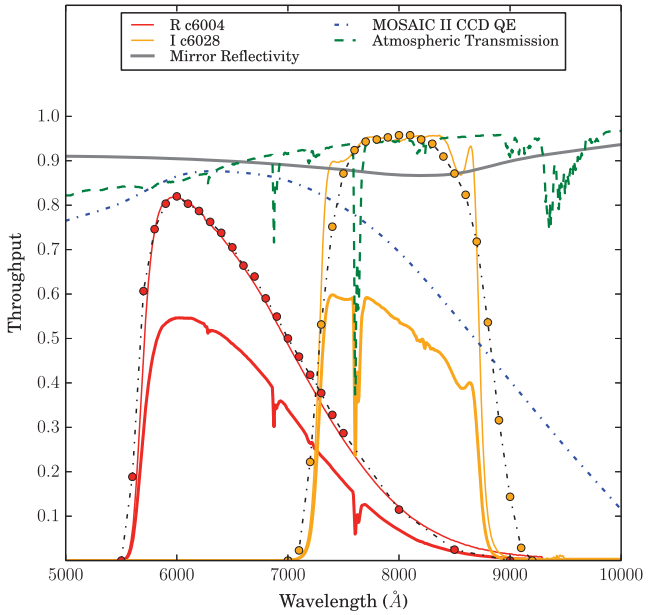

Figure 4. Throughput curves for CTIO Blanco *R* and *I* passbands (thick red and orange, respectively), representing full system throughput including wavelength dependence of CCD quantum efficiency (dot-dashed blue), aluminium reflectance of the mirrors (solid gray) in the Blanco telescope, the optical filters (thin red and orange), and a model of the atmosphere (dashed green) generated using the MODTRAN4 code at an airmass of 1 with 2 mm PMW of water vapor at an altitude of 2 km, and a contribution from aerosols, appropriate for the CTIO Blanco site. The measurement of the various components of the system throughput is discussed in Appendix B.1, and the response curves are listed in Table 9. The Bessell *R* and *I* filter curves (red and orange circles, joined by dot-dashed black lines, and normalized to have the same peak transmission) are shown for comparison.

Unfortunately, most well-measured spectrophotometric standards are too bright to be measured directly by the Blanco. We must therefore infer the Blanco natural magnitudes of the fundamental standard using the star's standard magnitudes. The most direct way of achieving this is to define the transformation equations such that the Landolt and natural system magnitudes agree at some color.

Historically, the choice for the fundamental standard for SN Ia surveys has been α Lyr (Vega), either implicitly when the rest-frame SN Ia model is constructed from low-z data, or explicitly, when defining the passband zero points for high-redshift surveys (Astier et al. 2006; Miknaitis et al. 2007; Hicken et al. 2009b, 2012; Contreras et al. 2010; Stritzinger et al. 2011). Vega was one of six A∅V stars used to establish the color zero point on the photometric system of Johnson & Morgan (1953) by defining the mean $U - B$ and $B - V$ colors of the six to be zero, and this definition was further extended to Cousins $R_C - I_C$. Vega's SED was tied to tungsten-ribbon filament lamps and laboratory blackbody sources employed as fundamental standards (Oke & Schild 1970; Hayes & Latham 1975). With the widespread adoption of the Landolt standard star network to tie instrumental photometry to the Johnson system, the use of Vega as the fundamental spectrophotometric standard became ubiquitous.

However, as discussed by Regnault et al. (2009), Vega is far from an ideal choice for the fundamental standard. Taylor (1986) found that in order for several sources of synthetic and observed Cousins $R_C - I_C$ measurements to agree, the I_C transmission curve had to be shifted to the red by 50–100 Å. With this shift, the synthetic color of Vega was found to be 0.006 mag. Fukugita et al. (1996) report a similar value. Furthermore, the Landolt $(R - I)_L$ color of Vega is significantly more blue than the average for the Landolt standard star network (with $(R - I)_L \sim 0.47$ mag), and consequently any systematic error in the color term or the Landolt $(R - I)_L$ color of Vega has a much larger systematic effect on the *RI* natural magnitudes than would a standard with a color closer to the average Landolt standard. Vega may exhibit some photometric variability (Fernie 1981). In addition, its SED is punctuated with several unusually shaped absorption lines. Vega has an excess of NIR emission longwards of 1–2 μm, likely a result of its dust ring (Bohlin 2014) and possibly its rapid rotation (Peterson et al. 2006). It also has an excess of UV emission relative to a 9400K model (a result of its rapid rotation (Bohlin et al. 2014)). These may introduce systematic errors when models are used to extend the observed SED of Vega into the UV and IR.

Following several groups including the SDSS (Ivezić et al. 2007) and the SNLS (Regnault et al. 2009), we instead select the sdF8 D star, BD+17°4708, as our fundamental spectrophotometric standard. At $(R - I)_L = 0.32$ mag, the color of BD+17°4708 is considerably closer to the average Landolt network star than Vega. The *HST* CALSPEC program has measured the SED of BD+17°4708 covering 0.17–1 μm with an uncertainty of <0.5% in the flux calibration derived from the three primary *HST* white dwarf standards and ~2% in the relative flux calibration over the entire wavelength range.

3.4.3. Transformation between Landolt Network and the CTIO Blanco Natural System

In order to calibrate the natural system of the Blanco, we obtained several images of three Landolt standard fields (L92, L95, Ru149) directly with the Blanco/MOSAIC II over 63 nights in 2006 and 2007. The images covered a wide range of airmass and exposure time and the calibration fields were dithered across the entire field of view. With this large data set, we robustly determined extinction and color terms between the Blanco and the Landolt network using the relations

$$\begin{aligned} R^{\rm Ins}_{4\,\rm m} + A_i &= R_L + k_{R_{4\,\rm m}}(X_i - 1) \\ &\quad + c^{R_{4\,\rm m}}_{(R-I)_L}((R - I)_L - 0.32) - Z_i \\ I^{\rm Ins}_{4\,\rm m} + A_i &= I_L + k_{I_{4\,\rm m}}(X_i - 1) \\ &\quad + c^{I_{4\,\rm m}}_{(R-I)_L}((R - I)_L - 0.32) - Z_i, \end{aligned} \quad (4)$$

where R and I denote the R- and I-band magnitudes in the Landolt (L) and CTIO Blanco instrumental (4 m) systems, and A, X, and Z denote the aperture correction, airmass, and zero point of an image, i respectively. These relations are defined such that at the color of BD+17°4708, the calibrated magnitudes of the Blanco system match those of Landolt.

We expect differences in the aperture corrections between science and calibration field frames. Images of the calibration fields were generally short exposures (<60 s) and often unguided, while science images are 200 s in *R* and 400 s in *I*. We found typical systematic differences of 1%–3% between the aperture corrections measured in the calibration fields and the mean aperture correction of all science fields observed on the same nights. The aperture correction differences are correlated with the PSF size and ellipticity measured in the calibration fields. We accounted for these aperture correction differences

while extrapolating zero points between images to construct the tertiary photometric catalogs in Section 3.5.

The average offset between Landolt magnitudes for catalog stars and measured instrumental magnitudes was calculated for each field, fitting for a single linear term in Landolt $0.3 < (R - I)_L < 0.8$ color. As there were insufficient stars covering the full color range in any single image, the weighted mean color term for all calibration field images with at least 20 stars in I and 50 stars in R was computed. Computing the color term image-by-image allowed us to look for trends in the color term with time and airmass. While this procedure leads to slightly higher statistical uncertainties than if a single color term was determined simultaneously for all images, it produces a robust estimate of the color term and, as shown in Section 6, the systematic uncertainties in the photometric calibration are dominated by the uncertainty in determining the absolute zero points.

We found color terms of $c^R_{R-I} = -0.030 \pm 0.001$ and $c^I_{R-I} = 0.022 \pm 0.001$. These values are in good agreement with measurements by observatory staff[31] for the Blanco. The dispersion about the fitted value is ∼2.5% in R and ∼1.5% in I. While this dispersion is significantly larger than the photon noise, this is not unexpected. We seek a single linear color term that is applicable over a range of color, and in a variety of observing conditions that reflect the conditions under which science images were acquired. As we compute these color terms image-by-image, the dispersion about the mean value reflects unmodeled variation in site conditions, as well as any variation in the sample of stars used to compute the color term for any given image. This procedure is preferable to one in which a subset of images are designated as having been acquired in "perfectly photometric" conditions, and are used for calibration, as any difference between conditions on photometric nights and the mean condition of science nights will lead to systematic errors in the photometric calibration.

The value in R is the same as that used by M07, while we find c^I_{R-I} to be lower by 0.008 ± 0.003 than that work. We attribute this difference to the different methodology used and the redder color range of stars selected for photometric calibration in the M07 analysis.

Several imagers show a strong radial dependence on the color term. Any relative error in the photometry between the center and periphery of the detector can affect the color term. Such effects can arise because of errors in the illumination correction or chromatic effects. Other wide-field imagers often include devices from different suppliers, and the quantum efficiency, and therefore the color term, is a function of position on the detector. Neither factor is a major consideration for MOSAIC II, and there is no evidence of this effect being a significant concern in other studies with this instrument. Nevertheless, we elected to look for any systematic CCD-to-CCD variation in the color terms. We found that the color term had a standard deviation of 0.005 in R and 0.003 in I about the mean. However, as standard fields were not observed over the full duration of the survey, and we might expect any low-level CCD-to-CCD variation to change as the instrument was mounted, unmounted, and cleaned, we cannot determine if this variance is systematic. Consequently elected to use a single color term for the entire imager, as in M07, and absorb this into our systematic error budget in Section 6.

[31] http://www.ctio.noao.edu/mosaic/ZeroPoints.html

We looked for systematic trends in the residuals between the image-by-image color terms and the mean color term over time, but found that these were not statistically significant. The increasing accumulation of dust on the optical surfaces leads to a changing zero point, but does not significantly affect the color terms.

The offset was re-fit with the color term fixed to this value and the aperture correction was added. Thus, the offset represents the average difference between the Landolt catalog magnitudes and our instrumental magnitudes through a consistent 25 pixel aperture. These aperture-corrected zero points were then regressed against the airmass to determine the slope of the extinction law and intercept.

We found no improvement in allowing the extinction term to vary between survey years. Rather, we found that we could sufficiently account for year-to-year changes in the overall transparency at the CTIO site by decomposing the survey zero point into a dominant constant term with a small night-to-night variation. We measured extinction law slopes of 0.104 mag airmass^{-1} and 0.058 mag airmass^{-1} in R and I, respectively, with dispersions of ∼0.02 mag about the fitted linear relation. The airmass relation and color terms determined are shown in Figure 5. Additionally, we used the RANSAC algorithm (Fischler & Bolles 1981) to determine both the extinction and color terms to ensure our fits were not sensitive to outliers. We found differences at the 10^{-5} level for the extinction coefficient, and typically at the 10^{-4} level for the image-by-image color terms, consistent with the uncertainties on these quantities.

3.5. Tertiary Catalogs and Zero Points

Having calibrated the amplifiers within the footprint of the Landolt standard field, we derived an extended standard catalog covering the entire field of view of MOSAIC II. As this catalog was generated by extrapolating the zero point to other amplifiers of the same image, we accounted for the differences in the aperture correction between amplifiers. This procedure prevented any systematic errors arising from PSF variation, a misestimation of the extinction coefficient, or short timescale variations in transparency from affecting the extended standard catalog.

The zero points were then re-determined using the extended catalog without any additional color correction applied. We extrapolated these zero points to science images on the same nights as the calibration images, adjusting for differences in exposure time, aperture correction, and airmass. For each star in the science fields, we determined the 3σ-clipped, error-weighted mean magnitudes to generate our final photometric reference catalog for each field. Stars with a high rms scatter relative to their mean magnitude errors were rejected as variable. The resulting catalogs typically have ∼30 stars per amplifier, with at least 3 observations in both filters, and a median of 8 observations each in R and 5 in I. A 0.4% uncertainty was added in quadrature to all stars, in order to make the average reduced χ^2 unity. The error-magnitude distribution of the reference catalog stars is shown in Figure 6.

These reference catalogs were used to determine zero points for all science images. To examine the temporal stability of the zero points, we adjusted them for differences in aperture correction, airmass, and exposure time, but not nightly variations in transparency or variation between different

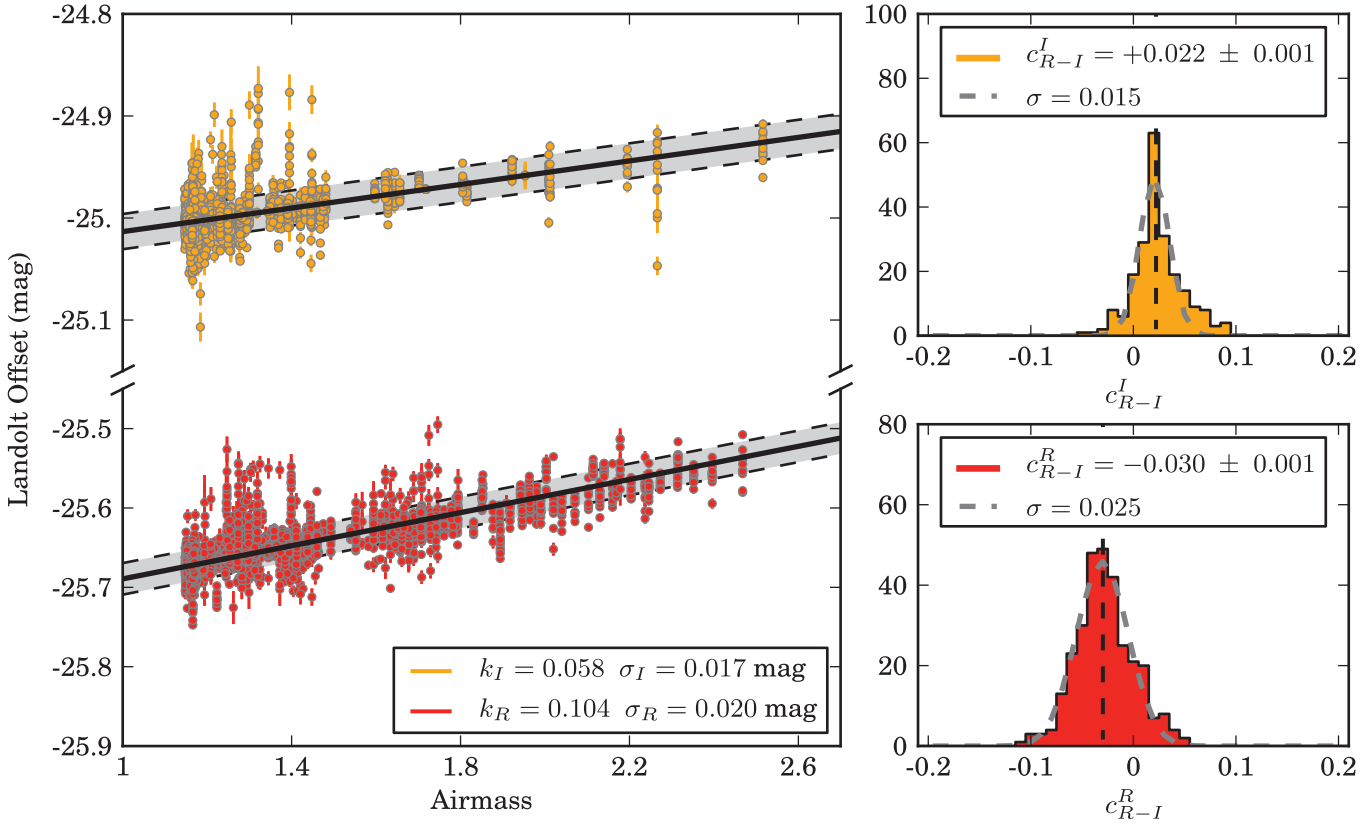

Figure 5. Left: Extinction relation for CTIO Blanco system in *R* and *I* using calibration data for three Landolt fields (L92, L95, and Ru149) imaged during the 2006 and 2007 observing seasons. The vertical axis is the difference between instrumental aperture magnitudes, and Landolt catalog magnitudes, corrected for exposure time and variation with Landolt $R - I$ color. We exclude any data taken in non-photometric conditions. We find extinction law slopes of 0.104 mag airmass^{-1} and 0.058 mag airmass^{-1} in *R* and *I*, respectively. Right: Distribution of color terms, determined per-image, to Landolt $R - I$ for the CTIO Blanco system in *I* (above) and *R* (below), using calibration data from 2006 to 2007. Only images with at least 50 stars in *R* and at least 20 stars in *I* were used in the analysis. As there are typically insufficient stars spanning the full color range in any single image, the weighted mean color term for all the images is computed (indicated by dashed vertical lines) and used for all further analysis. We find color terms of $c^{R_{4\,\mathrm{m}}}_{(R-I)_L} = -0.030 \pm 0.001$ and $c^{I_{4\,\mathrm{m}}}_{(R-I)_L} = 0.022 \pm 0.001$.

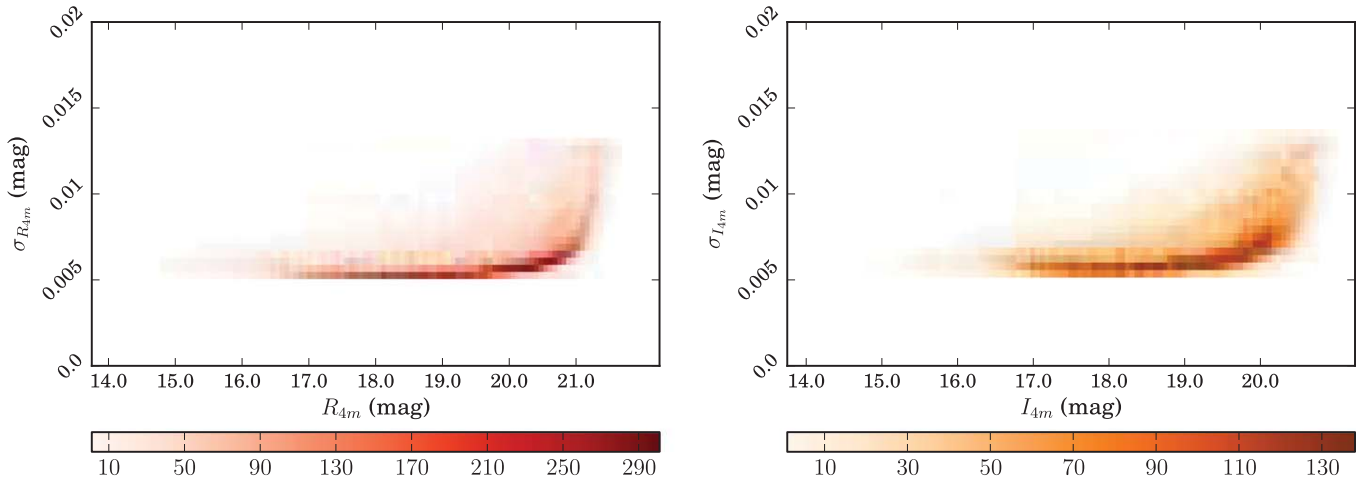

Figure 6. Uncertainty in the Blanco photometry of ESSENCE reference catalog stars as a function of magnitude for *R* and *I*. The color of each bin indicates the number of stars in that bin. Individual stars require at least three measurements in each filter. The systematic error arising from an error in the airmass or color term, determined in Section 6, has been added in quadrature with the statistical uncertainties.

amplifiers. The adjusted zero points of all available amplifiers were averaged together to construct the average adjusted zero point for a given image. In Figure 7, we plot this quantity as a function of the time since the start of the each year's observing season: the conditions at the Blanco remained very stable over the entire duration of the survey. We also constructed the nightly average zero point, and the histogram of residuals to the nightly average zero point is plotted in Figure 8. The residual scatter in the nightly zero point residuals is <2% in both *R* and *I*.

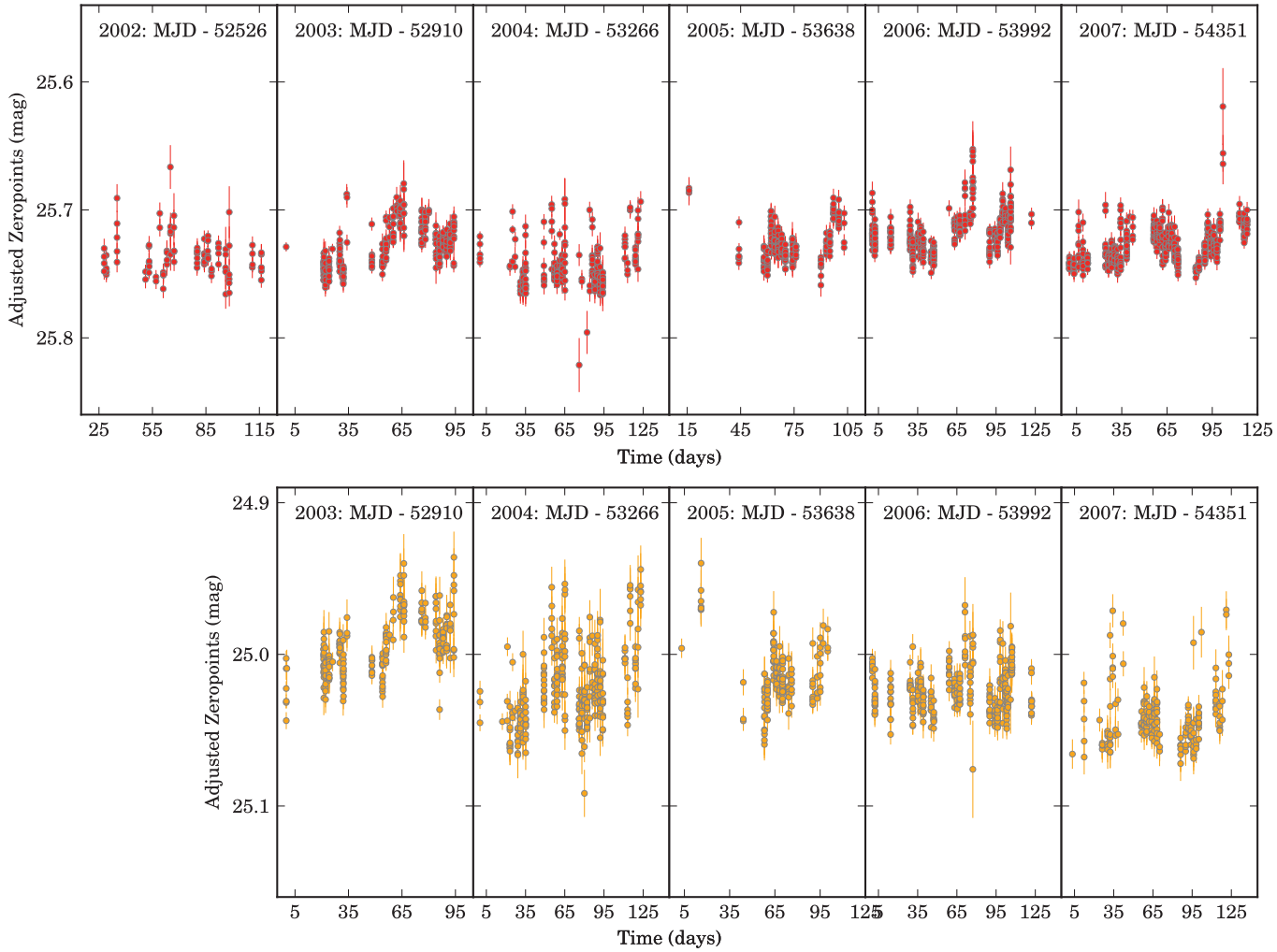

Figure 7. Average zero points for images adjusted for differences in exposure time, aperture correction, and airmass over the full duration of the ESSENCE survey in *R* (top) and *I*. In 2002, the *I* filter (NOAO code c6005) was damaged and replaced. The zero point evolution is correlated in both *R* and *I*, and the short timescale variations correspond to changes in weather conditions at CTIO, whereas the gradual drift in zero points is likely due to the increasing accumulation of dust in the optical system.

3.6. Image Subtraction

Having established zero points for each science image, we used image subtraction to remove the background light of the host galaxies. Prior to subtraction, the PSF of each image was first determined from field stars. We used the "High Order Transform Of PSF And Template Subtraction" (HOTPANTS)[32] package to determine the convolution kernel between each image and template pair. For each pair, the image with the narrower PSF was convolved to match the image with the broader PSF. All $N(N-1)/2$ possible pairs of image and reference templates from at least three observing seasons were used to create difference images for each object, following the algorithm of Barris et al. (2005). We used a version of DoPHOT (Schechter et al. 1993), modified to use the PSF and flux calibration of the image with the broader PSF, to measure flux in the difference image. The flux calibration of the difference image was adjusted by the normalization of the convolution kernel. The position of the supernova was measured by taking the weighted mean of all detections with a $S/N > 5$. The derived positions are accurate to $0\farcs02$. The flux in each difference image was measured with the PSF centroid fixed to the position of the supernova. A representative example of our image subtractions is provided in Figure 9.

As described in M07, the uncertainties in flux in our difference image are underestimated due to pixel–pixel covariance introduced during the re-sampling process. Rather than scale the noise in each image up by a constant factor of 1.2, as in M07, we determined a correction for each individual difference image using flux measurements across the frame. We convolved the PSF on a regular grid across the difference image, measured the standard deviation of the distribution of $\mathrm{flux}/\sigma_{\mathrm{flux}}$, and scaled each noise image by this factor. This process effectively accounts for the small residual pixel–pixel covariance introduced by deprojecting each image onto a common astrometric grid, and by the PSF convolution.

Additionally, we constructed a light curve for each object using a single deep reference image, observed in photometric conditions with excellent seeing, to identify any potential problems introduced in processing the thousands of difference images produced by the NN2 process. We found excellent

[32] https://github.com/acbecker/hotpants

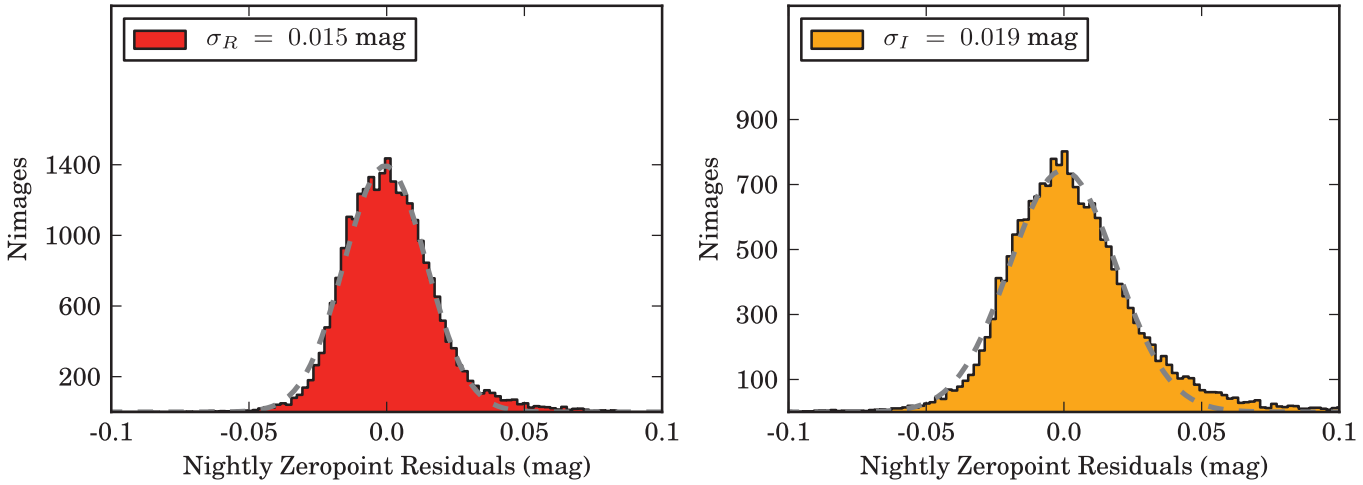

Figure 8. Histograms of the residuals of *R* (left) and *I* (right) zero points to the average nightly zero point, adjusted for differences in exposure time, airmass, and the aperture correction. The measured scatter in the nightly zero point residuals is <2% in both passbands, consistent with the standard deviations derived from a fit to a Gaussian distribution (dashed gray lines), and very comparable to the values found in M07, illustrating that zero points are very consistent from field to field.

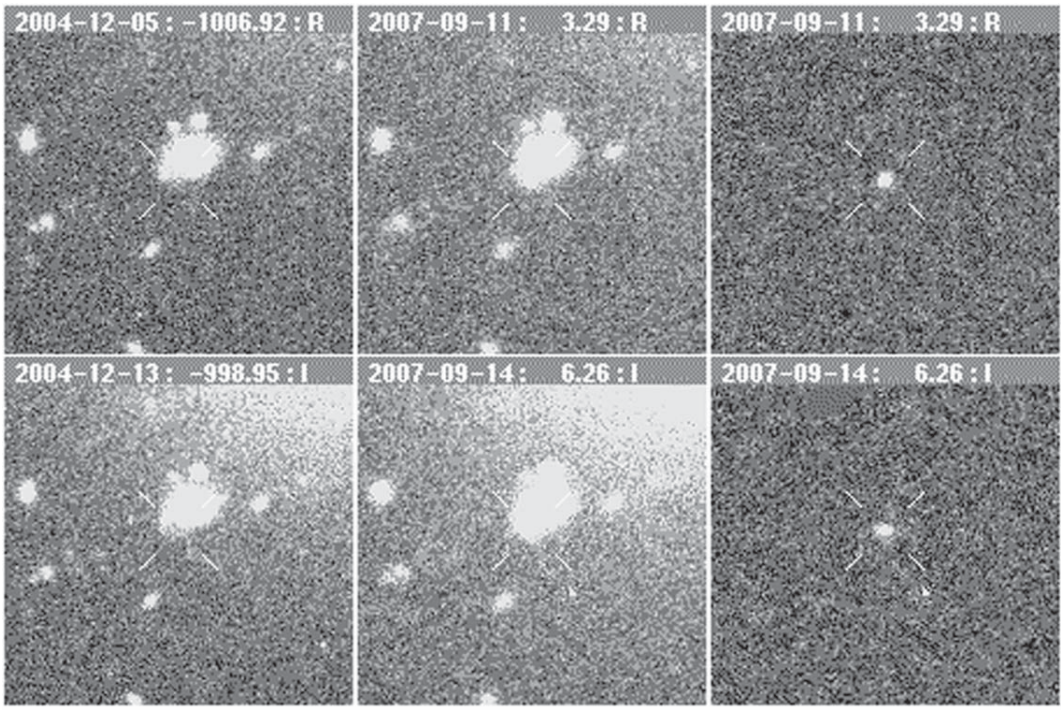

Figure 9. Representative difference imaging "postage stamps" in *R* (top) and *I* (bottom) for *x025*, a SN Ia at $z = 0.35$ near the median redshift of the survey. In this instance, HOTPANTS has convolved the PSF of the reference (left) to match the science image (middle). The reference is subtracted to produce the difference image (right). Despite the complex gradient in the background, and clear differences in PSF and depth between the reference and image, the difference image background is extremely uniform and free of artifacts.

agreement between the fluxes measured in the single template and in the NN2 process, with the uncertainty in the flux being lower in the latter, as is expected by the use of multiple images to measure the galaxy template and sky background at each epoch.

4. SPECTROSCOPY

Our full sample consists of all SN Ia for which we were able to obtain a positive spectroscopic identification. If possible, slits were aligned to obtain spectra of the host galaxies of the SN candidates in order to obtain a more accurate redshift. The first two years of spectroscopic data from ESSENCE were presented by Matheson et al. (2005), while M07 detailed our selection criteria and classification algorithms. The spectroscopic observations for the objects included in M07 were presented by Foley et al. (2009). The six-year spectroscopic sample from the ESSENCE survey is presented in this work, together with a summary of the spectroscopic observations, data reduction, and the process of candidate classification and redshift determination.

4.1. Selection Criteria for Candidates

As discussed in Section 2, over the six years of survey operation, ESSENCE detected thousands of objects exhibiting variability over multiple epochs, at a significance of $S/N > 5$. Given the limited spectroscopic resources for follow up, it was impossible to obtain spectra of all candidates. We employed various selection criteria to narrow the list of candidates from the imaging search to the subset with the most promise of being SN Ia. The first set of these selection criteria was implemented as software cuts in our search pipeline. We required the following.

1. Candidates detected in differences images have the same PSF as stellar objects in the source image that was convolved by HOTPANTS.
2. Candidates exhibit no significant negative flux (<30% of the total number of pixels within an aperture of radius 1.5× FWHM around the detection) to select against difference image artifacts, such as dipoles resulting from slight image misalignment.
3. Candidates did not exhibit significant variability in ESSENCE data from previous years to reject variable stars and active galactic nuclei (AGNs).
4. Candidates in the difference image are not within 1 pixel (0.″27) of objects in the template image, as these are frequently AGNs and spectra of such candidates suffer from excessive host galaxy contamination, making classification very uncertain.
5. Candidates exhibit at least two coincident detections with $S/N > 5$, in at least two passbands or within a five-night window in a single passband, to reject moving objects within the solar system.
6. Detector and image reduction artifacts were excluded by visual inspection.

To select SN Ia from the resulting list of candidates, we fit preliminary light curves using a *BV* template of a normal SN Ia ($\Delta m_{15} = 1.1$ mag) constructed from well sampled low-z SN Ia. This template is a good match to SN Ia observed in *RI* at $z \sim 0.4$, typical for the ESSENCE survey. Using χ^2 minimization, we determined the time of *B* maximum, the *RI* magnitudes at maximum, and the light curve stretch, *s*. These factors allowed us to determine an approximate photometric redshift for the object, which, along with the $R - I$ color and rise-time information where available, was used to select likely SN Ia.

An additional level of selection cuts was imposed by the observers on site. Observers tended to favor candidates thought to be in elliptical or low surface brightness hosts, as the former are reliably SN Ia, while the latter aid in extraction of a clean spectrum. As the various facilities and instruments have different capabilities, and reach different depths, our faintest objects were preferentially observed at larger aperture facilities.

We obtained spectroscopic follow up using a range of facilities including the Blue Channel spectrograph on the MMT (Schmidt et al. 1989); IMACS on Baade (Dressler 2004) and LDSS2 (Allington-Smith et al. 1994) and LDSS3[33] on Clay at the Las Campanas Observatory; GMOS on Gemini North and South (Hook et al. 2003); FORS1 on the 8 m Very Large Telescope (VLT) (Appenzeller et al. 1998); and LRIS (Oke et al. 1995), ESI (Sheinis et al. 2002) and DEIMOS (Faber et al. 2003) at the W. M. Keck Observatory.

[33] http://www.lco.cl/telescopes-information/magellan/instruments/ldss-3/

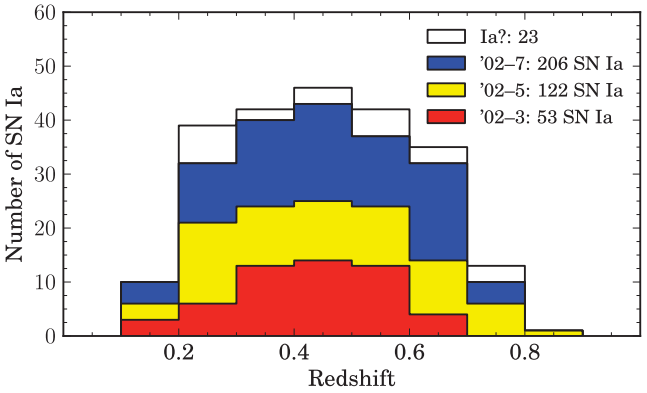

Figure 10. Redshift distribution of spectroscopically identified SN Ia from the ESSENCE survey. Candidates which have a high confidence of being of Type Ia (all objects whose SNID correlations with SN Ia templates exceed 50%) are plotted in the shaded region. The histogram is shown for observing seasons spanning 2002–2003 (red), 2002–2005 (yellow), and 2002–2007 (blue), along with *cumulative* totals, to illustrate the evolution of the redshift distribution over the course of the survey. Candidates for which we have less confidence have been classified "Ia?." Several of these objects have well-measured redshifts from their host galaxies. These are shown in the open region.

Spectra were processed and extracted using standard IRAF routines. Except for VLT data, all spectra were extracted using the optimal algorithm of Horne (1986). VLT spectra were extracted using a novel two-channel Richardson–Lucy restoration algorithm developed by Blondin et al. (2005) to minimize galaxy contamination in the target spectra. Spectra were wavelength calibrated using calibration lamp spectra (usually HeNeAr) fit with low-order polynomials, and were flux-calibrated using a suite of IRAF and IDL procedures, including the removal of telluric lines using the well-exposed continua of spectrophotometric standards.

To avoid relying on subjective assessments of noisy data, we employed the SuperNova Identification (SNID) algorithm (Blondin & Tonry 2007) to determine SN classifications objectively and reproducibly. SNID is based on the cross-correlation techniques of Tonry & Davis (1979). The input spectrum is compared to a large library of template spectra at zero redshift, including nearby SN of all types (SN Ia, Ib, Ic, II, and subtypes such as SN Ia-pec, SN 91 T, and SN 91bg; see Filippenko 1997 for a review of SN spectral classification), as well as other astrophysical sources such as luminous blue variables (LBVs) and other variable stars, galaxies, and AGNs. Where the redshift of the host galaxy is available, we forced SNID to look for correlations at that redshift (±0.02) to determine the SN classification. In general, the spectra of SN with $z > 0.5$ have lower S/N, and thus ambiguities between types occurred mainly in that redshift range.

The SNID algorithm has been presented by Matheson et al. (2005) and Foley et al. (2009), and we refer the reader to these publications for further details.

A list of all objects selected for spectroscopic follow up is provided in Table 6. An analysis of the spectroscopic efficiency of the ESSENCE survey was presented in Foley et al. (2009). The redshift distribution of all ESSENCE SN Ia is shown in Figure 10.

5. SN IA LIGHT CURVES FROM THE ESSENCE SIX-YEAR SAMPLE

Of the 422 objects listed in Table 6, 233 were considered SN Ia candidates based on their preliminary light curves. Spectra were obtained for 229 of those 233 objects. Using the observing spectra, 206 objects have been definitively classified as SN Ia.

Eight objects were observed in non-standard fields, without overlap with the calibration fields used in this paper. Additionally, a few objects were discovered near bright stars, or near the edge of the detector, and suffer from repeated difference imaging failures. We have excluded these objects from further analysis. Despite being classified as a SN Ia (IAUC 8251)[34], an analysis of the spectra of *e315* with `SNID` indicates that it does not meet the criteria used to classify an object as a Ia employed by this work.

The final *RI* photometry of 213 of the original 233 candidate SN Ia objects presented in this paper is listed in Table 7. Full light curves, including non-SN Ia objects, and measurements of the baseline flux will be made available as machine readable tables[35] along with this work. Photometry is presented in linear flux units, ϕ, in the Blanco natural system for each passband, T. Fluxes can be converted to calibrated magnitudes via:

$$m_T = -2.5\log_{10}(\phi_T) + 25. \quad (5)$$

The system throughput curves and zero points required to derive magnitudes in our passbands from SED models using Equation (3) are provided in Appendix B. The ESSENCE SN Ia and "Ia?" light curves are illustrated in Figure 11.

5.1. Light Curve Shape and Color Distributions

Several different algorithms to fit SN Ia optical photometry exist, including MLCS2k2 (Jha et al. 2007), BayeSN (Mandel et al. 2011), SALT2 (Guy et al. 2007, 2010), SiFTO (Conley et al. 2008), and Dm15 (Prieto et al. 2006). Each of these corrects for the shape and color relations, but they diverge when making two choices: the choice of how to train their spectral models and the choice of how to account for intrinsic and extrinsic color variations. This divergence results in a dichotomy between a physical model, where color variation is decomposed into an intrinsic variance and a reddening, attributed to extinction from dust (MLCS2k2 and BayeSN), versus an empirical model, where all color variation is directly correlated with luminosity (SALT2 and SiFTO). In the following subsection, we compare the color and shape parameter distributions derived using MLCS2k2 and SALT2 for the ESSENCE light curve sample presented in this work.

5.1.1. Light Curve Quality Cuts

While all the light curves are fit with both techniques, not all the fits are reliable, as several objects lack high-significance measurements of flux pre- or post-maximum, and these typically exhibit high χ^2/dof. Furthermore, objects in Table 6 without determined redshifts are not fit.

Some selection cuts are common to all SN Ia surveys, and are required to ensure that the light curve fit is well-constrained. These cuts are typically expressed in terms of the rest-frame phase in rest-frame days $\Phi = (T_{\rm Obs} - T_{\rm Max})/(1+z)$. Kessler et al. (2009, hereafter K09) required at least one measurement with $\Phi < 0.0$. Guy et al. (2010, hereafter G10)[36] employed a more flexible cut, only requiring a single measurement in the

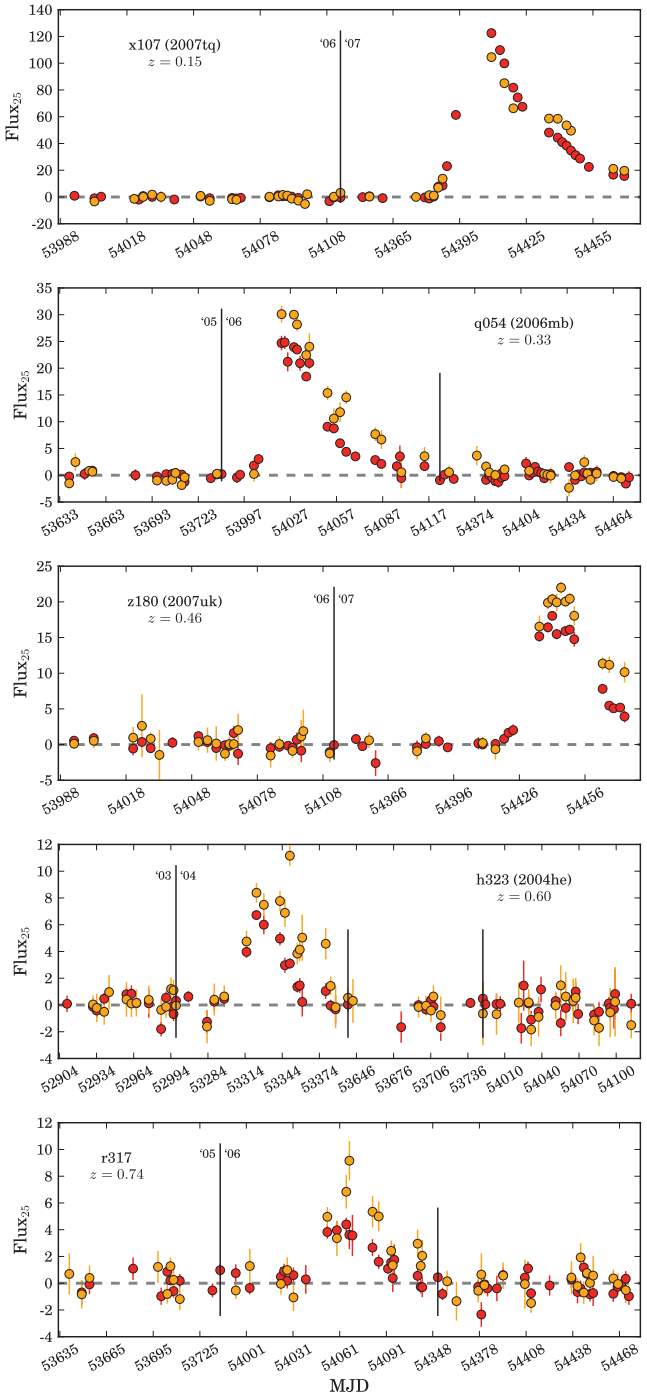

Figure 11. Example ESSENCE *R* (red) and *I* (orange) light curves, in units of linear flux, scaled such that a flux of unity corresponds to magnitude 25. Gaps between observing seasons have been removed, and the reported MJD is discontinuous at the locations of the vertical black lines. The first of these lines is elongated and the year of the observing season is indicated to the left and right of it.

[34] http://www.cbat.eps.harvard.edu/iauc/08200/08251.html

[35] Available through FAS Research Computing at Harvard—http://telescopes.rc.fas.harvard.edu/index_w.html.

[36] http://supernovae.in2p3.fr/salt/

range of $-8 < \Phi < +5$ days, and found that this provided a comparable constraint to the K09 cut. Similarly, WV07 required at least one observation with $\Phi \leqslant +5$ days for both MLCS2k2 and *SALT*, but also demanded that the observation had $S/N > 5$, while requiring that the uncertainty on the fit time of maximum, $\sigma_{T_{\rm Max}}$, be <2 days. The WV07 cut is effective at ensuring that the time and the peak flux are well-constrained, and we adopt it here for ESSENCE SN Ia. The compilation of 441 SN Ia presented by Conley et al. (2011, hereafter C11) uses the weaker G10 cut on observations near maximum. In addition, G10 do not impose any cut on S/N. However, these objects have observations in more passbands than ESSENCE, and the more conservative cut is appropriate.

When the cut on pre-maximum measurements is not applied, both the MLCS2k2 and *SALT2* light curve shape parameters (Δ and x_1, respectively) exhibit a significantly increased scatter as a result of light curve fits being ill-constrained with only the post-maximum decline. Scolnic et al. (2014a) also reports that x_1 shows a trend toward larger values for $z > 0.4$ if the pre-maximum data is excluded. G10 did not find such a trend with high S/N SN Ia at $z < 0.4$, illustrating how the effect of light curve quality cuts varies with median redshift, and therefore with survey.

WV07 and K09 also required that the fit statistic, $\chi^2/{\rm dof}$, be <3 for both light curve fitters. C11 did not impose any quality-of-fit cut, as they felt that the reported uncertainties for low-z photometry are frequently inaccurate, rendering such a cut misleading. They also suggested that several light curves contain the occasional outlying photometric observation that drives $\chi^2/{\rm dof}$ to artificially high values, despite having little to no effect on the derived light curve shape and color parameters. C11 also argues that any χ^2-based cut has an asymmetric effect with an SN Ia sample, and therefore can potentially a introduce bias with redshift. This in turn could lead to systematic bias on w. While there is merit in this argument, upon visual inspection of our light curve fits, we concluded that the $\chi^2/{\rm dof}$ statistic did accurately represent the quality of the fit, and that this cut was well motivated. In future work, we will use Monte Carlo simulations to assess any biases in cosmological inference that result from this cut.

Another common cut is on the minimum number of degrees-of-freedom. Both WV07 and K09 require $N^{\rm min}$ dof $\geqslant 5$. C11 do not explicitly state such a requirement, but the compilation they presented nevertheless satisfies that requirement. We adopt $N^{\rm min}$ dof $\geqslant 5$ for MLCS2k2; however, we found that this cut had the consequence of biasing us toward intrinsically brighter objects. WV07 also required one observation with $\Phi \geqslant +9$ days for MLCS2k2. This cut was intended to ensure that the decline post-maximum is well sampled. As MLCS2k2 also imposes its own cut by requiring observations with $S/N > 5$, this cut is considerably more stringent than was intended. This requirement causes a total of 44 SN Ia and "Ia?" objects to fail the selection cuts—by far the single largest cut on our MLCS2k2 fits. In addition to eliminating observations of faint sources, or sources at high-z with extremely well sampled declines, the S/N cut imposed by MLCS2k2 causes several light curves fits to fail the selection cuts as a result of an insufficient observations, given the requirement of $N^{\rm min}$ dof $\geqslant 5$ in the MLCS2k2 fit.

By contrast, WV07 only required one observation post-*B*-band maximum for *SALT*, and only three objects in our sample do not meet this cut. We believe that this demonstrates that MLCS2k2 is being needlessly conservative by requiring that all observations have $S/N > 5$. However, the intent of the cut on the number of observations post-maximum is to ensure that the light curve extinction or color is well-constrained, and the location of the peak is bounded. We are wary of the relatively weak effect of the post-maximum cut on our SALT2 light curve fits, and require a stricter $N^{\rm min}$ dof $\geqslant 8$ for that fitter. With the ESSENCE four-day cadence, this effectively ensures that there are at least four measurements of the observer frame $R - I$ color. As a result, the number of objects that fail the $N^{\rm min}$ dof cut for MLCS2k2 and SALT2 are similar, and some of the most egregious outliers in x_1 and c are eliminated.

Table 2
Effect of Light Curve Quality Cuts on the ESSENCE Sample

Cut	MLCS2k2	SALT2
Fit Failed	7	…
$\chi^2 > 3$	10	20
$N^{\rm min}$ dof[a]	18	20
$\Phi_{\rm First\ S/N>5}$[b]	9	17
$\sigma_{T_{\rm Max}}$	5	3
$\Phi_{\rm Last}$	44	3
$x_1\vert\Delta$ cut	14	18
c cut[c]	NA	33

Notes. The number of SN Ia and "Ia?" objects that are removed by each selection criterion. Each cut is imposed independently. Many objects fail multiple cuts.
[a] We require $N^{\rm min}$ dof $\geqslant 8$ for SALT2, rather than the weaker cut of 5 for MLCS2k2, as the last phase cut is very ineffective with SALT2 when our well sampled NN2 light curves are fit in flux space.
[b] While at first glance it appears that more objects fail the cut on pre-maximum imaging with SALT2 than with MLCS2k2, this is not the case on closer inspection. MLCS2k2 merely fails catastrophically for objects without pre-maximum imaging, and consequently does not report $T_{\rm Max}$ at all.
[c] WV07 did not employ an extinction cut. While we have not used one in this work, it is likely that we will employ a reasonable cut on this value to remove any highly reddened objects at low-z from the sample for a cosmological, as there is considerable uncertainty about the nature of the dust in the host galaxies of highly extinguished SN Ia.

Based on the results in G10, C11 imposed a restriction on the SALT2 color parameter, and required $-0.25 < c < 0.25$ mag. WV07 did not explicitly impose an equivalent cut on A_V for MLCS2k2. Several groups have used multi-color photometry of highly extinguished low-z SN Ia to demonstrate that the extinction law in the host galaxies of these objects appears to follow the O'Donnell (1994) extinction law with a significantly lower R_V than the Milky Way (Hicken et al. 2009a; Folatelli et al. 2010; Mandel et al. 2011).

Additionally, Scolnic et al. (2014b) employs a requirement that $-3 < x_1 < 3$ for the Pan-STARRS1 SN Ia sample. Both these cuts are well motivated as there are few SN Ia in the SALT2 training sample outside these ranges, and the fits are likely to be ill-conditioned there. WV07 adopted a requirement of $-0.4 \leqslant \Delta \leqslant 1.7$. All objects in our ESSENCE SN Ia sample that fail this requirement also fail other selection cuts.

A summary of the number of light curves that fail each cut for both MLCS2k2 and SALT2 is provided in Table 2.

5.1.2. MLCS2k2 Light Curve Analysis

We employ "v007" of MLCS2k2 with the "tweaked-slowz" vectors. These vectors, and the corresponding matrix of model uncertainties (denoted *S*), are trained using the low-z Hubble-

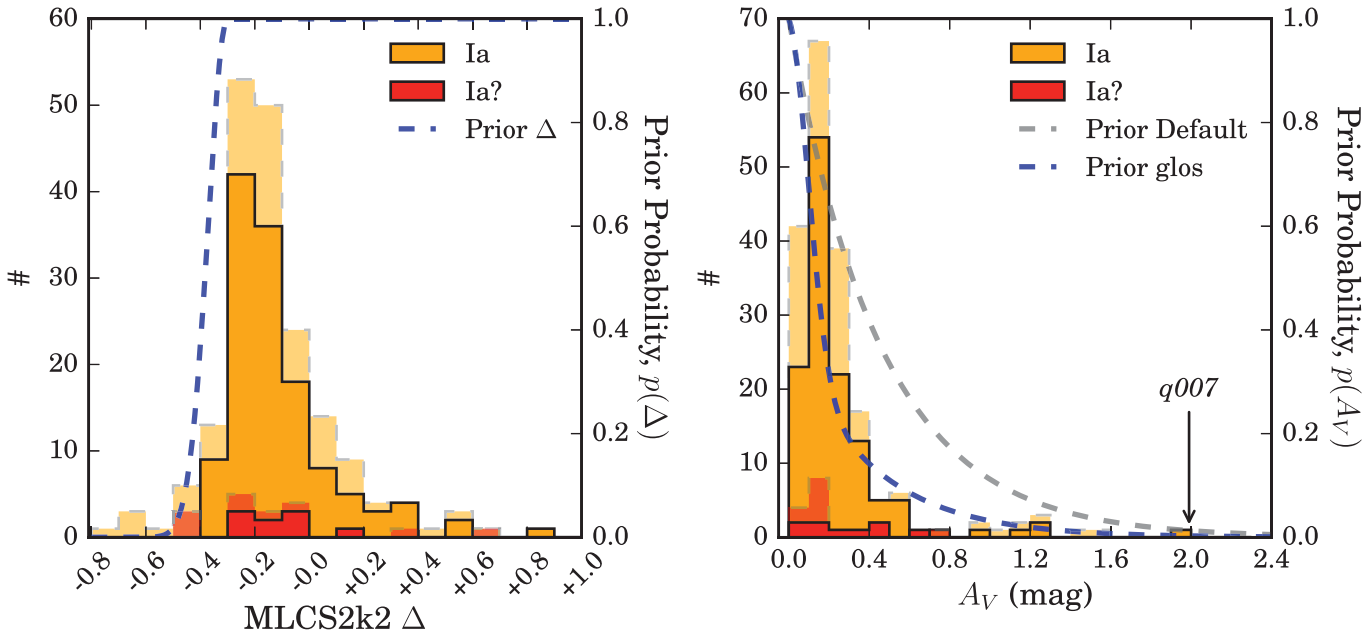

Figure 12. Light curve shape, Δ (left panel), and extinction, A_V (right panel), distributions estimated by MLCS2k2 for ESSENCE SN Ia (orange) and "Ia?" (red) objects. Objects that pass the selection cuts (excepting the cuts on the parameter being plotted itself) imposed in WV07 are indicated in the solid regions, while objects that fail are shown in the light regions bounded by dashed lines. The MLCS2k2 priors employed in the light curve fitting are shown as dashed blue lines. The "default" prior is the extinction distribution derived from low-zSN Ia during the training procedure.

Table 3
MLCS2k2 Light Curve Fit Parameters for ESSENCE SN Ia and "Ia?" Objects

ID	μ[a]	σ_μ	$T^B_{\rm max}$	$\sigma_{T_{\rm max}}$	$\Phi_{\rm First}$[b]	$\Phi_{\rm Last}$	Δ	σ_Δ	A_V[c]	σ_{A_V}	Q[d]
e108	42.370	0.140	52979.48	0.59	−11.768	9.954	−0.338	0.111	0.097	0.102	T
k425	41.207	0.254	53335.19	0.43	−9.535	19.618	−0.087	0.177	0.310	0.236	T
q002	41.212	0.359	54002.83	0.75	−6.340	15.192	0.594	0.279	0.549	0.369	T
x080	42.006	0.440	54384.94	1.54	−4.178	17.699	0.132	0.343	0.315	0.276	T

Notes.
[a] MLCS2k2 reports distance moduli with a $H_0 = 65$ km s^{-1} Mpc^{-1}.
[b] $\Phi_{\rm First|Last}$ is the rest-frame phase of the first and last observation, respectively, and is dependent on the B bandtime of maximum, $T^B_{\rm max}$.
[c] We use the Galactic reddening law of O'Donnell (1994), with R_V fixed to 3.1 to model the extinction in the host galaxy of the supernova.
[d] Flag describing if the object passes (T) or fails (F) the light curve quality cuts described by WV07.

flow sample in Jha et al. (2007; hence "slowz") and "tweaked" with small magnitude offsets (typically <0.005 mag) to match the color–extinction distribution zero point, and extended to −20 days prior to B-band maximum. We follow WV07 in using the "glosz" prior on extinction, and assume $R_V = 3.1$.

The MLCS2k2 light curve shape, Δ, and extinction, A_V, distributions for ESSENCE SN Ia and "Ia?" objects are shown in Figure 12. The MLCS2k2 light curve fit parameters for the ESSENCE sample are provided in Table 3. Additionally, we have indicated if the objects pass the light curve quality cuts used by WV07 for the four-year sample. From our spectroscopically confirmed SN Ia sample, 126 objects pass these cuts and are useful for cosmological inference. This doubles the 4 year ESSENCE sample of 60 SN Ia.

Objects with $\Delta > 1.0$ are underluminous relative to normal SN Ia, and are more rare. Consequently, we are extremely unlikely to find any at the redshifts probed by the ESSENCE survey. Objects that appear to be extremely overluminous (very negative values of Δ) relative to the training sample of Jha et al. (2007) typically have little or no high-significance flux measurements pre-maximum, but have well-measured declines post-maximum. Without a good constraint on the peak and time of maximum, light curve fitters typically explore unphysical regions of parameter space. The χ^2/dof of these light curve fits is often relatively high (>3) and all fail the quality cuts of WV07, either owing to a high χ^2/dof or because of insufficient observations pre-maximum.

The A_V distribution for ESSENCE SN Ia is consistent with the "glos" model discussed employed by WV07. The distribution is significantly narrower than the MLCS2k2 "default" distribution, derived from nearby SN Ia, as we are unlikely to find highly extinguished and therefore faint objects at high-z. As MLCS2k2 is a magnitude based fitter, it rejects measurements with S/N < 5. Most of the objects that fail the selection cuts in the right panel of Figure 12 are extremely faint or at high-z.

Note that Figure 12 shows the distribution for all recovered fits, and several of these objects do not have light curve fits that meet the quality cuts of WV07. Quality cuts are imposed to select spectroscopically confirmed SN Ia, with several high S/N measurements over rest-frame phase $-5 \leqslant \Phi \leqslant 20$ days, to ensure that the derived distance moduli are unbiased, whereas

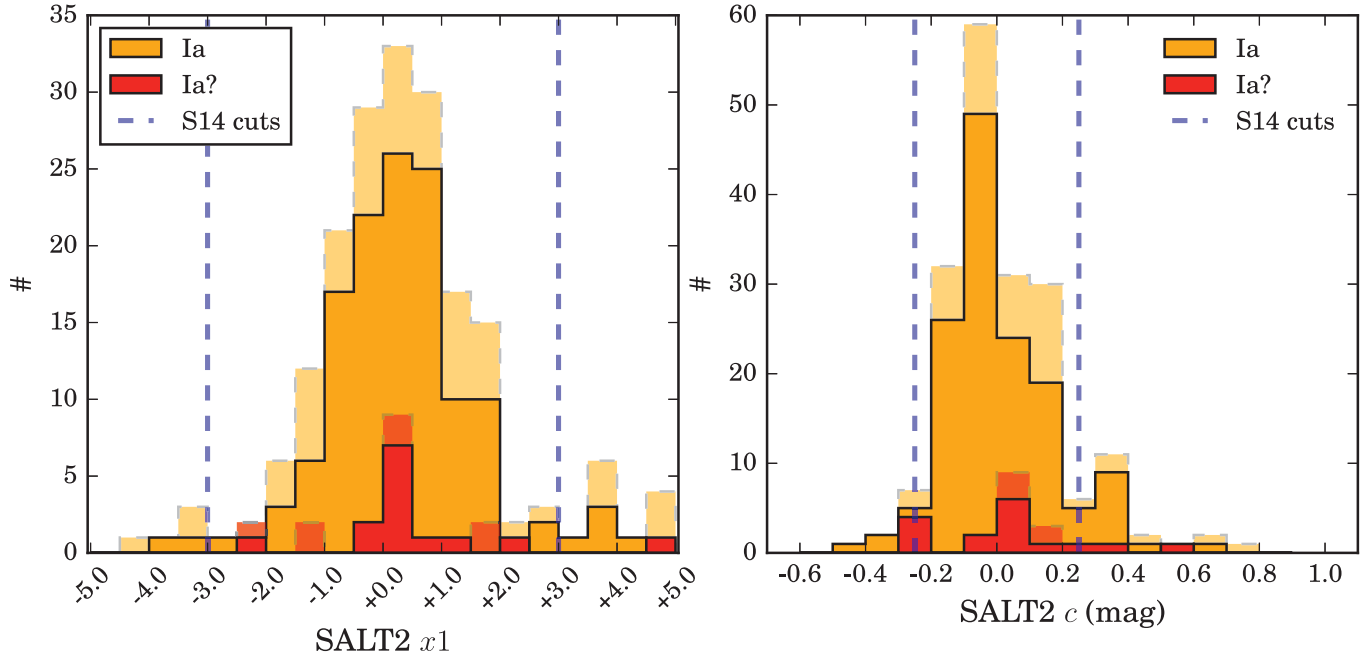

Figure 13. Light curve shape, x_1 (left panel), and color, c (right panel), distributions estimated by SALT2 for ESSENCE SN Ia (orange) and "Ia?" (red) objects. Objects that pass the original *SALT* selection cuts (except the cuts on the parameter being plotted itself) imposed by WV07 are indicated in the solid regions, while objects that fail are shown in the light regions bounded by dashed lines. Only the WV07 cuts relating to the sampling and χ^2/dof of the fit are used here. Based on a visual inspection of all the light curve fits, we required that the fits used at least eight epochs, rather than the weaker cut of at least five epochs employed for *SALT* in WV07. We employ the same cuts as Conley et al. (2011) and Scolnic et al. (2014a) on c and x_1, respectively.

Table 4
SALT2 Light Curve Fit Parameters for ESSENCE SN Ia and "Ia?" Objects

ID	m_B[a]	σ_{m_B}	m_V	σ_{m_V}	$T^B_{\max}$[b]	$\sigma_{T_{\max}}$	x_1	σ_{x_1}	c[c]	σ_c	Cov(c, x_1)[d]	Q[e]
b010	23.4583	0.0666	23.5138	0.0937	52593.2578	0.8841	0.9105	0.7618	−0.0781	0.1012	0.0248	T
g050	23.2239	0.0702	23.4278	0.1084	53302.2280	0.5811	−0.2400	0.5682	−0.2226	0.1069	0.0153	T
h323	23.4921	0.0594	23.3174	0.0873	53329.8365	0.6337	0.6074	0.5493	0.1485	0.0930	0.0094	F
n322	24.3561	0.0919	24.4587	0.2019	53707.8798	1.4726	0.1779	1.0967	−0.1237	0.1342	0.0518	T

Notes.
[a] SALT2 does not directly report distance estimates. The distance modulus is determined using a global fit for all SN Ia together with other cosmological parameters.
[b] While the SALT2 shape estimates are strongly affected by measurements pre-maximum, it uses significantly more low S/N measurements on the decline, as well as measurements for faint and/or high-z objects. Consequently, the cut on number of measurements post-maximum has very little impact. We instead require a total of eight observations be used in the fit to ensure that the measured parameters are reliable.
[c] We use the updated SALT2 color law described by Guy et al. (2010). This differs significantly from the O'Donnell (1994) extinction law in the near-UV.
[d] Covariances between all the fit parameters—Cov(m_B,x_1), Cov(m_B,c), and Cov(x_1, c)—are calculated, and these values will be included in the machine readable tables provided with this work.
[e] Flag describing if the object passes (T) or fails (F) the light curve quality cuts for *SALT* described by WV07 and the shape and color cuts described by Conley et al. (2011).

derived light curve shape and extinction are generally less susceptible to poor phase coverage.

5.1.3. SALT2 Light Curve Analysis

Additionally, we employ version 2.2.0b of SALT2 released together with G10. SALT2 is a flux-based fitter and employs measurements of the baseline flux to restrict the search range for fitted parameters. However, only data within the rest-frame phase range $-15 < \Phi < 45$ days are used in the χ^2 minimization. Measurements in observer frame filters that map to the rest-frame wavelength range $3000 < \lambda < 7000$ Å are used in the fit. Model and K correction uncertainties are propagated into the error matrix, and an additional U band calibration uncertainty of 0.1 mag is added in quadrature for low-z NUV data.

The SALT2 light curve shape, x_1, and color, c, distributions for ESSENCE SN Ia and "Ia?" objects are shown in Figure 13. The SALT2 light curve fit parameters for the ESSENCE sample are provided in Table 4. Additionally, we have indicated whether the objects pass a combination of the light curve quality cuts used by WV07 for the four-year sample, as well as shape and color cuts employed by Conley et al. (2011) and Scolnic et al. (2014b).

Objects with $x_1 < -3.0$ and $x_1 > 3.0$ are poorly represented in the SALT2 training sample. Fits with these values often have unconstrained rises or peaks, and provide unreliable distance estimates.

Table 5
Summary of the Systematic Uncertainties on Calibrated CTIO Blanco Natural Magnitudes from ESSENCE

Effect	Δ_R (mag)	Δ_I (mag)
Errors in the Measurement of Flux		
Shutter precision	<0.001	<0.001
Detector linearity	0.005	0.005
Image De-trending	±0.005	±0.005
Astrometric Uncertainties	0.005	0.005
Errors in the Photometric Calibration		
±10% error in airmass relation	∓0.001	∓0.002
Uncertainties in color term	±0.005	±0.005
Uncertainties in the zero point	0.003	0.001
Uncertainties in extrapolating zero points	<0.001	<0.001
Magnitudes of BD+17°4708	±0.002	±0.002
Total	±0.011	±0.010
SED of BD+17°4708	±0.002	±0.003
Total	±0.012	±0.011

Note. Italicized entries are sources of increased dispersion on distance moduli, but do not introduce systematic bias.

Conley et al. (2011) required that $-0.25 < c < 0.25$ mag to eliminate blue objects that were not adequately represented in the training sample, as well as objects with very red colors, which they believe are the result of a combination of different effects. It is possible that extinction in the host galaxy in the SN Ia is one of these effects. Three objects, *m040*, *m070,* and *m075*, are catastrophic outliers and are not displayed here. All three were discovered near the start of the 2005 observing season, and none has any pre-maximum photometry.

6. SYSTEMATICS AFFECTING THE ESSENCE SURVEY PHOTOMETRY

Here we identify and assess the size of each effect using empirical tests of internal and absolute photometric calibration. Wherever possible, we quantify systematics by directly introducing a bias at either the image or catalog level and propagating the bias through our pipeline to measure the effect on output photometry. We also compare our photometry to SDSS photometry converted to the Landolt system to set an upper limit on our systematic error budget and evaluate our absolute photometric calibration in the different ESSENCE fields.

The systematic effects can be divided into two categories.

1. Effects that cause errors in individual photometric measurements, *and correlate with distance, leading to a bias* in cosmological inference.
2. Effects that cause errors in individual photometric measurements, but are not correlated with distance, and therefore do not bias the cosmological result, but nevertheless lead to *increased dispersion* in Hubble residuals.

We list the various sources of photometric error in Table 5, and detail and estimate the effect of each in the subsections that follow.

6.1. Shutter Precision

The MOSAIC II shutter is described in Section 2. The shutter blades take 23 ms to cover the entire field, leading to a ±0.5% non-uniformity for a one second exposure. This is a negligible correction for the exposure times of all ESSENCE science (200 s in R and 400 s in I) and calibration frames (>10 s in both filters).

6.2. Detector Linearity

We imaged the Ru149 field in R and I varying the exposure times from 2 to 400 s.[37] Fluxes are measured for isolated stars using a fixed 20 pixel aperture radius and corrected for extinction. These stars span the dynamic range of the detector below saturation. We compute residuals to the average magnitude for each star, and compute the 3σ clipped average residuals for all stars. We find that these average residuals are <0.005 mag over the entire range of exposure times for both filters so we infer that the detector is linear to ∼0.5%. We also examined the difference between our measured instruemental magnitudes and catalog magnitudes, at constant exposure time, to check if there was any departure from linearity with flux. We do not see any evidence of nonlinearity with flux below saturation.

6.3. Systematic Uncertainties with Image De-trending

We avoid most long period systematic errors with image pre-processing by using biases and flat fields obtained nightly, rather than a global bias or flat field for a full observing season. Any systematic errors caused by a misestimation of the bias or the flat field will only affect measurements made on a single night. While photometric measurements of objects observed on those nights will be systematically biased, this error does not affect photometric measurements of the same objects from other nights. Consequently, the effect is very unlikely to correlate with distance modulus, and will not lead to a bias in cosmological measurements.

The systematic uncertainties associated with the illumination correction are estimated in Appendix A and found to be <0.3%. We typically obtain ∼10 bias and dome flat images in each filter each observing night. Comparing the combined bias and flat-field images of consecutive nights, we find differences of ∼0.1%. As these errors can occur simultaneously, and affect the image processing additively, we adopt a 0.5% error as the systematic error associated with our image de-trending.

6.4. Astrometric Uncertainties

The astrometric uncertainty of a single detection is composed of a systematic floor and a term that is inversely proportional to the S/N and directly proportional to the FWHM of the detection:

$$\sigma_a^2 = \sigma_{\rm sys}^2 + \sigma_d^2 \left(\frac{\rm FWHM}{\rm SNR}\right)^2. \quad (6)$$

We use the procedure detailed in Rest et al. (2014, Appendix A) and find that the single-epoch positions for supernovae are accurate to within 0.″02. M07 measured the impact of such an offset by identifying sources of known flux with FWHM typical for the survey, and measuring their flux through a PSF

[37] Exposures under 10 s are not used outside this analysis of detector linearity.

Table 6
Transient Objects Considered for Follow-up Observations by the ESSENCE Survey

ESSENCE ID	IAU ID	Type	Subfield	Amp	R.A. (J2000)	decl.	z_{SNID}	σ_z	z_{GAL}	$\sigma_{z_{GAL}}$	$MW_{E(B-V)}$
a002	…	Gal	wxc1	4	23:34:48.580	−10:11:02.260	…	…	0.3155	0.0002	0.02469
b001	…	Unk	wxc1	14	23:36:07.860	−10:02:26.660	…	…	…	…	0.02580
b002	…	Star	wxh1	1	00:12:51.140	−10:38:27.050	…	…	−0.0003	0.0002	0.03826
b003	2002iu	Ia	wx06	14	00:13:33.100	−10:13:09.920	0.115	0.005	…	…	0.03980
b004	2002iv	IaT	wx17	6	02:19:16.110	−07:44:06.720	0.226	0.006	0.2283	0.0006	0.02329
b005	2002iw	Gal	wxd1	11	23:43:07.250	−09:48:05.200	…	…	0.2048	0.0003	0.02989
b006	2002ix	II?	waa7	16	23:31:00.863	−09:29:07.205	…	…	…	…	0.02854
b008	2002jq	Ia	wx01	5	23:35:57.960	−10:05:56.880	0.477	0.005	…	…	0.02647
b010	2002iy	Ia	wdd5	7	02:30:40.022	−08:11:40.469	0.594	0.005	0.587	0.0010	0.03252
b013	2002iz	Ia	wdd5	10	02:31:20.745	−08:36:13.414	0.427	0.003	0.4274	0.0005	0.03283
b014	…	Gal	wdd5	15	02:31:11.408	−08:10:53.113	…	…	0.2689	0.0002	0.03390
b015	…	Gal	wcx1	9	23:36:44.070	−10:24:23.300	…	…	0.2070	0.0002	0.02875
b016	2002ja	Ia	waa7	15	23:30:09.685	−09:35:01.809	0.334	0.008	…	…	0.03111
b017	2002jb	Ia	waa7	6	23:29:44.149	−09:36:34.508	0.272	0.006	…	…	0.03442
b019	…	Gal	wxd1	4	23:40:47.490	−09:42:19.340	…	…	0.2129	0.0007	0.03084
b020	2002jr	Ia	wcc9	1	02:04:41.039	−05:09:40.727	0.431	0.004	…	…	0.02485
b022	2002jc	Ia	wcc2	3	02:07:27.285	−03:50:20.744	0.534	0.008	…	…	0.02457
b023	2002js	Ia	wx18	9	02:20:35.390	−09:34:43.900	0.557	0.003	…	…	0.02399
b024	…	Star	wxc1	16	23:36:31.330	−09:55:01.600	…	…	0.0001	0.0002	0.02861
b025	…	Unk	wxa1	5	23:24:11.150	−09:13:20.120	…	…	…	…	0.03153
b027	2002jd	Ia	wx11	16	00:28:38.390	+00:40:29.290	0.316	0.003	…	…	0.02587
c002	…	Unk	wbb6	14	01:10:05.029	+00:16:31.437	…	…	…	…	0.02483
c003	2002jt	Ia	wx06	15	00:13:36.700	−10:08:24.000	0.565	0.006	…	…	0.03682
c005	…	AGN	waa7	10	23:30:54.777	−09:56:47.863	0.248	0.002	…	…	0.02350
c012	2002ju	Ia	wx18	16	02:20:11.000	−09:04:37.500	0.349	0.005	0.3473	0.0001	0.02649
c014	2002jv	Ib	wcc3	3	02:04:34.815	−03:51:57.919	…	…	0.2203	0.0001	0.02400
c015	2002jw	Ia	wdd5	2	02:30:00.539	−08:36:22.561	0.356	0.007	0.3575	0.0006	0.03399
c016	2002jx	Gal	wxm1	4	00:26:54.136	+00:22:49.750	…	…	0.8446	0.0004	0.02350
c020	…	Unk	wxt2	15	02:20:32.124	−07:36:02.690	…	…	…	…	0.02342
c022	…	Ib	wxu2	15	02:21:06.336	−09:06:51.820	…	…	0.2123	0.0003	0.02529
c023	…	Ia	wx11	15	00:28:03.160	+00:37:50.430	0.412	0.011	0.3987	0.0003	0.02295
c024	…	Gal	wdd5	5	02:29:56.521	−08:23:52.283	…	…	0.3174	0.0001	0.03786
c025	…	AGN	waa7	14	23:30:18.309	−09:38:02.438	0.361	0.002	…	…	0.02845
c027	…	Gal	wxm1	4	00:27:56.787	+00:25:19.760	…	…	0.4534	0.0002	0.02240
c028	…	AGN	wxu2	16	02:20:03.304	−09:05:20.990	2.033	0.004	…	…	0.02664
d009	…	Ia	waa6	16	23:25:55.900	−08:56:41.300	0.351	0.002	0.3535	0.0002	0.03752
d010	2003jp	Ic	waa6	16	23:26:03.281	−08:59:22.829	…	…	0.0829	0.0001	0.03668
d029	…	AGN	waa6	13	23:25:11.206	−09:13:38.505	2.584	0.003	…	…	0.03429
d033	2003jo	Ia	waa6	10	23:25:24.047	−09:26:00.659	0.530	0.008	0.5251	0.0003	0.03621
d034	…	AGN	waa7	10	23:30:31.616	−09:56:24.390	2.285	0.007	…	…	0.02421
d051	…	Gal	wcc8	2	02:06:48.703	−05:08:46.023	…	…	0.3817	0.0002	0.02180
d057	2003jk	Unk	wbb6	3	01:08:06.169	+00:02:20.636	…	…	…	…	0.02948
d058	2003jj	Ia	wbb6	3	01:07:58.519	+00:03:01.918	0.589	0.009	0.5839	0.0002	0.02883
d059	…	Gal	wcc5	3	02:06:49.459	−04:26:47.244	…	…	0.2076	0.0002	0.02262
d060	…	Star	wcc7	3	02:09:02.757	−05:03:39.667	0.001	0.003	…	…	0.02159
d062	…	AGN	wcc9	3	02:04:19.323	−05:01:44.661	2.433	0.004	…	…	0.02430
d083	2003jn	IaT	wdd9	12	02:29:21.199	−09:02:15.490	0.330	0.006	…	…	0.02798
d084	2003jm	Ia	wdd9	11	02:28:50.940	−09:09:58.077	0.516	0.006	0.5221	0.0002	0.02516
d085	2003jv	Ia	waa5	16	23:27:58.197	−08:57:11.687	0.401	0.008	0.4047	0.0001	0.03495
d086	2003ju	Ia	waa5	3	23:27:01.704	−09:24:04.573	0.201	0.003	…	…	0.03459
d087	2003jr	Ia	wbb5	4	01:11:06.232	+00:13:44.210	0.337	0.004	0.3400	0.0003	0.02516
d089	2003jl	Ia	wdd6	8	02:28:28.568	−08:08:44.932	0.425	0.005	…	…	0.02997
d091	…	Unk	wcc1	2	02:09:35.211	−03:56:17.327	…	…	…	…	0.02298
d093	2003js	Ia	wdd5	3	02:29:52.152	−08:32:28.155	0.361	0.003	0.3636	0.0001	0.03212
d097	2003jt	Ia	wdd5	10	02:31:54.595	−08:35:48.609	0.430	0.005	…	…	0.03114
d099	2003ji	Ia	wcc2	16	02:07:54.841	−03:28:28.055	0.216	0.003	…	…	0.02456
d100	2003jq	IaP	waa7	16	23:30:51.191	−09:28:34.044	0.158	0.003	…	…	0.02863
d115	…	Unk	wbb6	11	01:09:45.163	+00:02:02.740	…	…	…	…	0.03106
d117	2003jw	Ia	wdd8	16	02:31:06.836	−08:45:36.535	0.301	0.005	0.2968	0.0002	0.02918
d120	…	AGN	wcc1	2	02:09:44.494	−03:57:02.923	1.279	0.005	…	…	0.02299
d123	…	Gal	wcc9	16	02:06:08.565	−04:39:08.710	…	…	0.4995	0.0004	0.02430
d124	…	AGN	wcc9	15	02:06:04.554	−04:41:45.145	0.617	0.023	…	…	0.02348
d149	2003jy	Ia	wcc4	11	02:10:53.987	−04:25:49.436	0.344	0.008	0.3388	0.0002	0.02020
d150	…	Gal	wcc1	12	02:10:12.486	−03:49:09.928	…	…	0.1910	0.0003	0.02450

Table 6
(Continued)

ESSENCE ID	IAU ID	Type	Subfield	Amp	R.A. (J2000)	decl.	z_{SNID}	σ_z	z_{GAL}	σ_{zGAL}	$MW_{E(B-V)}$
d156	2003jx	Unk	wcc2	4	02:06:33.398	−03:48:39.117	…	…	…	…	0.02311
e018	…	AGN	wbb7	2	01:13:59.547	+00:32:48.750	0.181	0.001	…	…	0.02879
e020	2003kk	Ia	waa6	9	23:25:36.054	−09:31:44.807	0.159	0.006	0.1643	0.0008	0.03411
e022	2003kj	IIP	wbb7	12	01:14:36.556	+00:23:58.180	…	…	0.0784	0.0001	0.02926
e025	…	Gal	wdd3	15	02:29:07.399	−07:36:34.479	…	…	0.1797	0.0002	0.02982
e027	…	Gal	wcc7	16	02:11:09.129	−04:39:19.417	…	…	0.8043	0.0000	0.01969
e029	2003kl	Ia	wbb3	15	01:09:48.798	+01:00:05.496	0.332	0.008	0.3333	0.0009	0.03509
e103	…	Unk	wbb9	2	01:09:32.340	+00:36:43.930	…	…	…	…	0.02437
e106	…	Unk	wbb6	11	01:09:45.163	+00:02:02.740	…	…	0.3219	0.0009	0.03106
e108	2003 km	Ia	wdd8	4	02:30:09.001	−09:04:35.621	0.473	0.009	…	…	0.03216
e118	…	AGN	waa5	11	23:27:48.448	−09:22:53.295	0.552	0.007	…	…	0.03665
e119	…	Gal	wbb1	7	01:14:16.912	+01:03:06.427	…	…	0.5584	0.0002	0.03121
e120	…	Gal	waa5	9	23:28:37.492	−09:30:30.569	…	…	0.2974	0.0002	0.03937
e132	2003kn	Ia	wcc1	7	02:09:15.549	−03:35:41.010	0.235	0.006	0.2443	0.0003	0.02585
e133	…	Gal	wcc1	7	02:09:17.662	−03:35:41.255	…	…	0.2450	0.0003	0.02596
e136	2003ko	Ia	wcc1	12	02:11:06.495	−03:47:55.899	0.348	0.006	0.3602	0.0008	0.02329
e138	2003kt	Ia	wdd4	1	02:33:46.992	−08:36:22.141	0.608	0.006	…	…	0.03294
e140	2003kq	IaT	wdd5	15	02:31:04.089	−08:10:56.603	0.614	0.006	0.6060	0.0002	0.03341
e141	…	Ib	wdd7	2	02:32:30.272	−09:05:53.662	…	…	0.0982	0.0001	0.02972
e143	…	Unk	wdd7	3	02:33:11.715	−09:03:32.183	…	…	0.1107	0.0001	0.02632
e147	2003kp	Ia	wdd5	9	02:31:02.652	−08:39:50.909	0.647	0.008	…	…	0.03419
e148	2003kr	Ia	wdd5	10	02:31:20.960	−08:36:14.195	0.431	0.006	0.427	0.0010	0.03281
e149	2003ks	Ia	wdd5	10	02:31:34.528	−08:36:46.462	0.498	0.008	…	…	0.03166
e309	…	Star	waa9	14	23:25:14.230	−09:44:25.810	0.001	0.003	…	…	0.02968
e315	2003ku	Ia	wbb9	3	01:08:36.253	−00:33:20.780	…	…	…	…	0.03573
e418	…	Unk	wcc2	8	02:07:30.851	−03:30:49.497	…	…	…	…	0.02304
e501	…	Unk	waa1	1	23:29:20.159	−08:54:27.836	…	…	…	…	0.03161
e504	…	AGN	waa3	4	23:25:01.338	−08:41:49.753	0.675	0.005	…	…	0.04289
e510	…	Unk	waa1	13	23:30:59.971	−08:37:34.344	…	…	…	…	0.03116
e528	…	Unk	wcc5	3	02:07:37.767	−04:27:06.738	…	…	…	…	0.02129
e529	…	Unk	wcc5	3	02:06:42.954	−04:26:31.293	…	…	…	…	0.02226
e531	2003kv	Ia?	wcc1	4	02:09:42.519	−03:46:48.442	…	…	…	…	0.02288
e604	…	Gal	waa6	8	23:23:51.868	−08:59:17.456	…	…	0.4357	0.0001	0.03519
f001	2003lg	IIP	wbb7	1	01:13:32.675	+00:36:57.310	0.171	0.006	…	…	0.02730
f011	2003lh	Ia	wcc7	12	02:10:19.505	−04:59:32.063	0.544	0.006	…	…	0.02000
f017	…	AGN	wdd9	10	02:28:38.844	−09:11:09.202	0.725	0.004	…	…	0.02542
f041	2003le	Ia	wbb6	8	01:08:08.739	+00:27:09.580	0.560	0.004	…	…	0.02934
f044	…	Ia	wbb8	8	01:11:20.561	+00:04:10.020	…	…	0.4078	0.0003	0.02544
f076	2003lf	Ia	wbb9	1	01:08:49.807	−00:44:13.490	0.408	0.004	…	…	0.03948
f095	…	Gal	wcc2	8	02:06:56.203	−03:31:07.936	…	…	0.3130	0.0008	0.02336
f096	2003 lm	Ia	waa3	3	23:24:25.501	−08:45:50.834	0.413	0.004	0.4080	0.0001	0.04193
f123	…	Ia	wcc1	7	02:09:57.282	−03:32:26.609	0.534	0.009	0.5261	0.0002	0.02410
f213	…	Unk	wbb4	12	01:14:50.770	+00:14:35.919	…	…	…	…	0.03231
f216	2003ll	Ia	wdd4	15	02:35:41.190	−08:06:29.788	0.595	0.011	0.5958	0.0001	0.03288
f221	2003lk	Ia	wcc4	14	02:11:12.817	−04:13:52.110	0.443	0.004	0.4413	0.0003	0.02044
f231	2003ln	Ia	waa1	13	23:30:27.131	−08:35:46.927	0.615	0.003	…	…	0.02860
f235	2003lj	Ia	wbb5	13	01:12:10.034	+00:19:51.267	0.422	0.006	0.4171	0.0006	0.03243
f244	2003li	Ia	wdd3	8	02:27:47.294	−07:33:46.220	0.546	0.005	0.5403	0.0002	0.02690
f247	…	Gal	wbb8	10	01:12:32.219	+00:31:12.730	…	…	0.4306	0.0003	0.03018
f301	…	Ia	wdd6	1	02:27:26.513	−08:42:24.782	0.514	0.011	…	…	0.03007
f304	…	Unk	wdd6	2	02:28:23.108	−08:34:22.780	…	…	…	…	0.03088
f308	…	Ia	wdd6	10	02:29:22.391	−08:37:38.480	0.388	0.010	…	…	0.02955
f401	…	Gal	waa1	1	23:29:40.692	−08:56:37.030	…	…	0.2023	0.0002	0.02929
f441	…	Unk	wbb6	7	01:08:58.453	+00:22:15.570	…	…	…	…	0.02517
g001	2004fi	Ia	waa1	1	23:29:45.348	−08:54:36.347	0.268	0.002	0.2648	0.0002	0.02895
g004	…	Ic	wbb4	14	01:15:06.214	+00:23:38.571	0.143	0.006	…	…	0.02853
g005	2004fh	Ia	waa2	13	23:28:27.197	−08:36:55.071	0.220	0.006	…	…	0.02759
g009	…	Gal	wbb4	13	01:14:28.998	+00:16:56.247	…	…	0.1831	0.0003	0.02991
g014	…	Gal	wbb1	6	01:13:18.202	+00:57:00.728	…	…	0.1949	0.0003	0.02787
g043	2004fj	IIP	wbb6	16	01:09:51.075	+00:27:20.934	0.190	0.002	0.1874	0.0008	0.02529
g046	…	Gal	wcc9	14	02:05:34.300	−04:46:30.968	…	…	0.1833	0.0002	0.02507
g050	2004fn	Ia	waa7	10	23:30:20.114	−09:58:30.698	0.616	0.008	0.6045	0.0003	0.02444
g052	2004fm	Ia	waa8	7	23:26:58.138	−09:37:19.346	0.381	0.007	…	…	0.03110
g053	2004fl	Ia?	waa8	7	23:26:57.910	−09:37:18.984	…	…	0.6329	0.0022	0.03110

Table 6
(Continued)

ESSENCE ID	IAU ID	Type	Subfield	Amp	R.A. (J2000)	decl.	z_{SNID}	σ_z	z_{GAL}	σ_{zGAL}	$MW_{E(B-V)}$
g055	2004fk	Ia	wbb7	7	01:13:35.842	−00:09:27.500	0.302	0.006	0.2964	0.0004	0.02823
g097	…	Ia	waa8	16	23:27:37.164	−09:35:21.041	0.339	0.004	0.3434	0.0002	0.03130
g108	2004fp	IIP	wdd8	4	02:29:53.012	−09:01:16.554	0.162	0.004	…	…	0.03378
g120	2004fo	Ia	wbb1	1	01:13:28.975	+00:35:16.179	0.507	0.004	…	…	0.02854
g128	…	II?	waa2	5	23:26:43.669	−08:37:31.458	…	…	0.1642	0.0006	0.02539
g133	…	Ia	wcc4	7	02:09:49.626	−04:10:55.064	0.422	0.003	…	…	0.02434
g142	…	Ia	waa2	11	23:28:37.713	−08:45:03.948	0.398	0.013	0.4033	0.0001	0.02842
g151	2004fq	Ic	waa2	14	23:27:45.638	−08:31:12.785	0.455	0.003	0.1462	0.0004	0.02689
g160	2004fs	Ia	wdd8	15	02:31:19.943	−08:49:21.751	0.507	0.019	…	…	0.02952
g166	2004fr	Gal	wdd9	14	02:28:43.772	−08:54:24.030	…	…	0.2016	0.0007	0.02988
g181	…	Unk	wdd9	2	02:28:35.984	−09:13:43.261	…	…	0.5324	0.0002	0.02629
g185	…	II	waa2	1	23:26:56.854	−08:55:12.970	0.345	0.007	…	…	0.03440
g199	2004ft	Gal	wdd4	7	02:33:32.622	−08:09:34.178	…	…	0.7665	0.0002	0.03713
g204	…	Unk	wcc2	13	02:08:26.690	−03:44:44.620	…	…	0.1114	0.0001	0.02356
g213	…	Gal	wbb8	6	01:11:54.176	−00:13:45.690	…	…	0.8423	0.0002	0.02886
g219	…	II?	wbb9	10	01:10:27.165	−00:39:11.615	…	…	…	…	0.03111
g225	…	Ia	waa5	2	23:27:15.685	−09:27:59.728	0.579	0.009	…	…	0.03504
g230	…	Ia	wbb5	3	01:11:56.314	+00:07:27.441	…	…	0.3934	0.0001	0.03077
g240	…	Ia	waa1	14	23:30:41.823	−08:34:10.893	0.696	0.007	…	…	0.02974
g276	…	Gal	wcc1	7	02:09:17.715	−03:35:43.709	…	…	0.2442	0.0002	0.02597
h280	…	II	wbb6	10	01:09:28.330	−00:01:22.880	…	…	0.2633	0.0005	0.03395
h283	2004ha	Ia	wcc9	5	02:04:27.005	−04:52:46.192	0.498	0.008	…	…	0.02678
h293	…	Unk	wcc9	2	02:05:11.580	−05:09:04.692	…	…	0.5462	0.0001	0.02479
h296	…	Gal	wdd6	12	02:28:45.533	−08:27:36.835	…	…	0.0590	0.0003	0.03198
h299	2004hb	Gal	wcc8	15	02:08:09.708	−04:41:51.880	…	…	0.7186	0.0002	0.02098
h300	…	Ia	wdd8	15	02:31:40.680	−08:49:03.377	0.657	0.003	…	…	0.02939
h304	…	Gal	wcc1	2	02:09:10.894	−03:58:00.789	…	…	…	…	0.02352
h311	2004hc	Ia	waa3	4	23:24:32.664	−08:41:03.574	0.752	0.003	…	…	0.04188
h317	…	Gal	wcc8	10	02:08:21.585	−05:05:09.208	…	…	0.6377	0.0001	0.02130
h319	2004hd	Ia	wcc5	11	02:08:48.217	−04:26:10.319	0.478	0.002	0.4903	0.0002	0.02047
h323	2004he	Ia	wdd6	13	02:29:48.797	−08:20:45.875	0.603	0.007	0.5978	0.0003	0.03481
h336	…	Gal	waa3	7	23:24:56.441	−08:28:40.498	…	…	0.3916	0.0005	0.03609
h342	2004hf	Ia	wdd5	9	02:32:00.143	−08:42:23.852	0.421	0.005	…	…	0.02867
h345	2004hg	Unk	wdd4	10	02:34:55.193	−08:30:43.591	…	…	…	…	0.03145
h352	…	Gal	wcc4	13	02:10:48.002	−04:17:54.131	…	…	0.1807	0.0002	0.02172
h353	…	Gal	waa2	15	23:28:14.068	−08:26:54.628	…	…	0.2196	0.0002	0.02513
h359	2004hi	Ia	wcc8	10	02:08:38.835	−05:08:11.825	0.347	0.005	…	…	0.02095
h361	…	Unk	wcc7	13	02:11:14.030	−04:53:40.148	…	…	…	…	0.02149
h363	2004hh	Ia	wcc9	16	02:06:25.028	−04:38:04.035	0.211	0.006	…	…	0.02475
h364	2004hj	Ia	wdd9	16	02:29:41.943	−08:43:49.480	0.344	0.003	…	…	0.03400
k374	…	Gal	wdd9	1	02:27:34.292	−09:17:08.085	…	…	0.1423	0.0004	0.02785
k396	2004hk	Ia?	waa2	5	23:27:04.384	−08:38:45.178	0.271	0.006	…	…	0.02637
k397	…	Unk	wcc1	7	02:09:31.278	−03:34:21.189	…	…	…	…	0.02564
k402	…	Unk	wbb5	12	01:12:54.197	+00:11:25.151	…	…	…	…	0.03139
k411	…	IaP	waa3	10	23:26:11.781	−08:50:17.355	0.562	0.004	…	…	0.03456
k425	2004hl	Ia	wbb7	3	01:13:38.174	−00:27:39.045	0.274	0.003	0.2702	0.0001	0.02922
k426	…	Gal	wdd8	4	02:30:51.203	−09:04:27.406	…	…	0.7572	0.0003	0.02568
k429	2004hm	Ia	wdd3	6	02:28:03.110	−07:42:29.656	0.171	0.006	0.1720	0.0006	0.03060
k430	2004hn	Ia	wbb1	2	01:13:32.382	+00:37:15.455	0.576	0.007	…	…	0.02719
k432	…	Ia	waa2	3	23:26:46.120	−08:45:42.405	0.706	0.010	…	…	0.02786
k437	2004ho	Gal	wcc3	11	02:06:16.041	−03:52:27.803	…	…	0.2878	0.0001	0.02292
k440	…	Unk	wbb4	7	01:14:18.151	+00:29:02.397	…	…	…	…	0.02874
k441	2004hq	Ia	wdd5	5	02:30:18.037	−08:22:25.045	0.669	0.006	…	…	0.04245
k442	…	Unk	wcc3	10	02:06:19.076	−03:58:01.372	…	…	…	…	0.02295
k443	2004hp	Unk	wcc1	4	02:09:35.522	−03:46:23.520	…	…	…	…	0.02244
k444	…	Gal	wdd5	2	02:30:00.763	−08:37:25.930	…	…	0.1921	0.0002	0.03426
k448	2004hr	Ia	wbb6	2	01:08:48.336	+00:00:49.449	0.405	0.007	0.4081	0.0001	0.03243
k453	…	Gal	wdd8	13	02:31:36.957	−08:58:10.962	…	…	0.5418	0.0003	0.02825
k459	…	Unk	wcc7	10	02:10:28.886	−05:07:11.337	…	…	…	…	0.01991
k467	…	Ia?	wdd2	13	02:31:11.801	−07:47:34.124	0.607	0.008	…	…	0.02913
k472	…	Gal	wcc3	15	02:06:29.663	−03:33:08.079	…	…	0.1368	0.0002	0.02320
k485	2004hs	Ia	wcc4	6	02:09:33.689	−04:13:03.931	0.417	0.003	…	…	0.02454
k490	…	Ia	wdd2	4	02:30:24.320	−07:53:20.935	0.709	0.001	0.7147	0.0009	0.03220
k505	…	Gal	wcc3	13	02:06:11.608	−03:44:17.379	…	…	0.2405	0.0001	0.02248

Table 6
(Continued)

ESSENCE ID	IAU ID	Type	Subfield	Amp	R.A. (J2000)	decl.	z_{SNID}	σ_z	z_{GAL}	σ_{zGAL}	$MW_{E(B-V)}$
k509	…	Gal	waa5	10	23:28:31.296	−09:25:39.880	…	…	0.2064	0.0001	0.03928
m001	…	Ia	wbb6	1	01:08:22.010	−00:05:46.654	0.290	0.004	…	…	0.03584
m002	…	Gal	waa6	15	23:26:06.272	−09:05:22.919	…	…	0.3545	0.0002	0.03602
m003	…	IIP	wcc9	15	02:05:27.303	−04:42:53.777	…	…	0.2014	0.0003	0.02508
m004	…	Gal	wcc8	8	02:07:12.708	−04:37:27.898	…	…	0.3834	0.0004	0.02205
m006	…	Ib/c?	wdd8	1	02:30:27.266	−09:16:10.189	0.051	0.001	0.0572	0.0002	0.02980
m010	…	Ib	wdd8	9	02:31:46.238	−09:16:25.667	…	…	0.2156	0.0003	0.02735
m011	…	II	wcc5	16	02:08:06.229	−04:03:51.137	…	…	0.2045	0.0003	0.02310
m012	…	Gal	wdd3	16	02:29:13.485	−07:34:07.335	…	…	0.1138	0.0002	0.02954
m014	…	II	wcc5	3	02:07:12.911	−04:26:40.049	…	…	0.1988	0.0001	0.02264
m022	…	Ia	waa1	14	23:30:02.706	−08:33:36.539	0.238	0.004	…	…	0.03070
m025	…	Gal	waa6	11	23:25:11.601	−09:23:41.144	…	…	0.7008	0.0001	0.03662
m026	…	Ia	waa5	12	23:28:39.960	−09:19:49.986	0.656	0.006	0.6548	0.0003	0.03742
m027	…	Ia	wbb6	12	01:09:15.013	+00:08:14.797	0.285	0.003	0.2885	0.0002	0.02834
m028	…	Gal	wcc5	12	02:08:49.544	−04:23:12.189	…	…	0.6075	0.0001	0.02094
m032	…	Ia	waa7	2	23:29:35.343	−09:58:46.304	0.154	0.003	…	…	0.02911
m034	…	Ia	wdd3	2	02:27:50.324	−07:59:11.705	0.562	0.006	0.5577	0.0002	0.03114
m035	…	AGN	waa1	5	23:28:55.967	−08:38:18.364	1.497	0.009	…	…	0.03167
m037	…	Gal	wdd3	10	02:29:03.971	−07:59:43.697	…	…	0.2397	0.0002	0.02607
m038	…	II	wcc9	6	02:05:10.823	−04:47:13.982	…	…	0.0507	0.0004	0.02412
m039	…	Ia	wdd3	6	02:28:04.636	−07:42:44.373	0.249	0.003	0.2481	0.0002	0.03069
m040	…	Ia	wdd3	6	02:27:30.201	−07:41:49.985	0.481	0.003	…	…	0.03237
m041	…	IIP	wcc7	7	02:09:49.784	−04:45:10.513	0.220	0.006	…	…	0.02231
m042	…	Gal	waa6	3	23:24:23.781	−09:22:12.082	…	…	0.1254	0.0001	0.03098
m043	…	Ia	waa1	1	23:29:51.729	−08:56:46.084	0.266	0.003	0.2654	0.0010	0.02926
m057	…	Ia	wcc4	11	02:10:56.774	−04:27:29.962	0.183	0.004	0.1810	0.0002	0.01992
m062	…	Ia	wbb3	10	01:09:52.911	+00:36:19.019	0.316	0.004	0.3139	0.0001	0.02457
m070	…	Ia	wdd4	7	02:33:46.821	−08:08:26.888	0.214	0.003	0.2122	0.0002	0.03753
m075	…	Ia	waa3	7	23:24:42.288	−08:29:08.021	0.101	0.003	0.0996	0.0002	0.03620
m078	…	Gal	wcc2	5	02:07:05.775	−03:41:28.385	…	…	0.3951	0.0005	0.02350
m082	…	Unk	wcc2	4	02:07:13.757	−03:49:12.890	…	…	0.3472	0.0002	0.02425
m087	…	Ia	wdd4	3	02:33:37.004	−08:27:32.462	0.289	0.006	0.2870	0.0003	0.03448
m095	…	AGN	wdd2	3	02:30:26.427	−07:57:27.227	0.992	0.012	…	…	0.03305
m111	…	AGN	wcc7	11	02:10:36.083	−05:00:57.306	1.001	0.004	…	…	0.02014
m135	…	Gal	waa1	2	23:29:32.878	−08:51:20.312	…	…	0.2887	0.0001	0.02885
m138	…	Ia	wbb3	3	01:08:56.340	+00:39:25.350	0.585	0.004	0.5877	0.0001	0.02758
m139	…	IIn	waa3	7	23:23:57.823	−08:27:08.205	…	…	0.2113	0.0001	0.03730
m142	…	Unk	wbb1	12	01:15:17.691	+00:47:17.513	…	…	…	…	0.03129
m158	…	Ia	waa6	3	23:24:03.540	−09:23:18.267	0.461	0.006	…	…	0.03056
m161	…	Gal	wdd9	4	02:28:23.645	−09:03:12.171	…	…	0.2304	0.0001	0.02661
m166	…	AGN	waa1	5	23:29:20.817	−08:36:48.770	0.304	0.002	…	…	0.02623
m193	…	Ia	wdd3	14	02:28:52.199	−07:42:09.763	0.336	0.006	0.3304	0.0002	0.02804
m219	…	Gal	wdd4	5	02:34:28.090	−08:15:19.399	…	…	0.3104	0.0003	0.03676
m226	…	Ia	wcc9	16	02:06:03.688	−04:39:59.080	0.674	0.008	0.6739	0.0013	0.02413
n244	…	Unk	wdd3	7	02:28:11.797	−07:36:29.340	…	…	…	…	0.02938
n246	…	Ia?	wbb7	11	01:14:33.074	−00:26:23.184	0.503	0.005	0.7055	0.0005	0.03047
n255	…	Gal	wcc7	5	02:09:05.303	−04:53:36.615	…	…	0.1369	0.0002	0.02116
n256	…	Ia	wdd3	5	02:28:09.012	−07:47:49.616	0.620	0.007	…	…	0.02975
n258	…	Ia	wcc5	4	02:06:42.346	−04:22:36.982	0.525	0.008	0.5191	0.0002	0.02257
n260	…	AGN	wcc8	2	02:06:36.320	−05:06:45.964	2.013	0.006	…	…	0.02087
n261	…	AGN	wbb7	16	01:14:59.513	−00:05:55.501	3.540	0.040	…	…	0.03026
n263	…	Ia	wcc9	4	02:05:14.946	−04:56:39.087	0.365	0.003	…	…	0.02569
n268	…	Gal	wdd6	15	02:29:19.971	−08:12:02.467	…	…	0.2791	0.0004	0.03090
n271	…	IIP	wbb5	16	01:13:06.506	+00:30:04.835	0.236	0.003	…	…	0.03371
n278	…	Ia	waa5	11	23:28:17.550	−09:23:12.360	0.308	0.006	0.3037	0.0002	0.03983
n284	…	AGN	waa1	8	23:29:38.374	−08:21:32.166	1.990	0.008	…	…	0.02812
n285	…	Ia	waa3	8	23:23:51.357	−08:23:18.503	0.531	0.009	0.5325	0.0001	0.03738
n295	…	AGN	waa3	3	23:24:03.280	−08:44:36.907	1.235	0.007	…	…	0.03854
n312	…	Gal	wdd9	14	02:28:45.104	−08:55:47.232	…	…	0.2860	0.0002	0.02937
n322	…	Ia	wdd9	12	02:29:00.487	−09:02:52.992	0.753	0.006	…	…	0.02713
n326	…	Ia	waa1	10	23:29:58.590	−08:53:12.468	0.267	0.006	0.2637	0.0002	0.02986
n346	…	IIn	waa1	3	23:28:58.301	−08:46:52.839	…	…	0.2661	0.0002	0.02994
n368	…	Ia	waa7	9	23:30:32.013	−10:03:22.140	0.342	0.006	0.3419	0.0002	0.02315
n395	…	Gal	wcc8	7	02:07:32.469	−04:42:10.706	…	…	0.4617	0.0002	0.02208

Table 6
(Continued)

ESSENCE ID	IAU ID	Type	Subfield	Amp	R.A. (J2000)	decl.	z_{SNID}	σ_z	z_{GAL}	σ_{zGAL}	$MW_{E(B-V)}$
n400	…	Ia	wbb8	12	01:13:13.258	−00:23:25.853	0.421	0.007	0.4250	0.0001	0.03102
n404	…	Ia	wdd8	14	02:31:31.433	−08:55:11.512	0.211	0.005	…	…	0.02875
n406	…	Ia?	wdd8	16	02:31:19.601	−08:45:09.787	0.7700	0.01	…	…	0.02933
n408	…	Gal	wbb9	16	01:09:49.036	−00:07:42.929	…	…	0.9198	0.0003	0.03468
p415	…	Gal	waa3	16	23:26:02.504	−08:21:10.846	…	…	0.3434	0.0002	0.02900
p425	…	Ia	waa1	14	23:29:56.189	−08:34:24.400	0.456	0.004	0.4583	0.0001	0.03095
p429	…	Ia?	waa3	13	23:26:02.216	−08:35:47.978	…	…	0.5482	0.0002	0.02983
p434	…	Ia	wbb5	12	01:12:40.253	+00:14:56.591	…	…	0.3383	0.0004	0.03441
p444	…	Ia	wcc2	5	02:06:36.165	−03:41:33.614	0.633	0.004	…	…	0.02423
p445	…	Ia	wbb1	4	01:13:14.547	+00:48:47.659	0.816	0.002	0.8069	0.0002	0.02458
p454	…	Ia	wcc2	15	02:08:32.461	−03:33:34.241	0.691	0.008	…	…	0.02282
p455	…	Ia	wcc4	15	02:11:00.014	−04:09:37.601	0.285	0.006	0.2974	0.0002	0.02023
p458	…	Unk	waa3	10	23:25:30.268	−08:52:04.940	…	…	…	…	0.03947
p459	…	Ia	wcc4	10	02:10:20.082	−04:33:13.440	0.702	0.004	…	…	0.02173
p461	…	Gal	waa5	6	23:26:42.317	−09:07:28.646	…	…	0.4075	0.0005	0.03451
p520	…	Ia?	wcc2	12	02:08:09.339	−03:48:04.967	…	…	…	…	0.02298
p521	…	Gal	wcc7	14	02:10:17.525	−04:46:52.214	…	…	0.3053	0.0002	0.02171
p524	…	Ia	wdd8	6	02:30:10.156	−08:52:50.856	0.516	0.004	…	…	0.03528
p527	…	Ia?	wcc2	15	02:08:10.469	−03:32:17.637	…	…	0.4351	0.0002	0.02451
p528	…	Ia	wcc2	8	02:07:04.661	−03:28:04.268	0.780	0.009	0.7812	0.0001	0.02355
p534	…	Ia	wcc3	4	02:04:56.094	−03:49:03.645	0.610	0.005	0.6202	0.0011	0.02438
p535	…	Unk	wcc5	13	02:08:28.123	−04:16:34.893	…	…	…	…	0.02216
q002	…	Ia	wcc3	6	02:05:12.945	−03:39:00.723	0.350	0.003	0.3469	0.0002	0.02326
q006	…	Ia?	wcc1	10	02:10:52.276	−03:57:39.374	0.290	0.010	…	…	0.02208
q007	2006lw	Ia	wcc2	10	02:08:33.670	−03:57:12.888	0.210	0.004	0.2135	0.0002	0.02401
q008	2006ly	Ia?	wdd4	10	02:34:42.381	−08:30:39.885	0.287	0.010	0.2913	0.0002	0.03191
q014	2006 lx	Ia	wdd5	8	02:30:10.389	−08:06:54.094	0.270	0.003	0.2693	0.0002	0.03147
q018	…	Ia?	wdd5	14	02:31:39.017	−08:18:05.170	0.270	0.010	…	…	0.03499
q021	…	Ia?	wdd4	7	02:33:43.919	−08:05:50.050	0.360	0.010	…	…	0.03818
q022	…	Ia?	wbb5	9	01:12:03.875	−00:01:29.045	0.226	0.010	…	…	0.03038
q031	…	Gal	wbb6	2	01:08:42.081	−00:00:57.201	…	…	0.2697	0.0002	0.03289
q036	2006lz	II-pec	wdd6	8	02:27:40.742	−08:10:08.182	0.179	0.006	…	…	0.02762
q048	2006ma	Ia	wbb7	11	01:15:11.657	−00:28:03.151	0.440	0.010	0.4371	0.0007	0.03018
q049	2006mc	Ia	wdd8	11	02:32:02.611	−09:07:21.181	0.421	0.005	0.4204	0.0001	0.02963
q054	2006mb	Ia	wdd8	5	02:30:54.298	−08:57:42.078	0.331	0.005	0.3275	0.0003	0.02705
q060	…	IIP	wbb1	11	01:14:48.945	+00:44:47.120	…	…	0.1441	0.0002	0.03191
q061	2006me	Ia	wbb4	11	01:14:47.189	+00:10:13.284	0.302	0.005	0.2996	0.0001	0.03176
q067	2006mf	Ia	wdd2	3	02:30:37.318	−07:57:04.538	0.187	0.007	0.1824	0.0003	0.03380
q069	2006md	Ia?	wbb5	6	01:11:31.492	+00:24:34.163	0.262	0.010	0.2470	0.0004	0.02595
q070	…	Gal	wdd6	6	02:28:04.925	−08:15:40.481	…	…	0.1256	0.0003	0.02960
q075	2006mg	Ia	wdd2	9	02:31:37.750	−08:06:40.098	0.427	0.005	…	…	0.04023
q102	2006mh	Ia?	wbb4	14	01:15:13.398	+00:23:57.312	0.435	0.010	0.4359	0.0008	0.02898
q106	2006mk	Ia	wdd5	1	02:30:16.911	−08:40:47.345	0.477	0.004	0.4754	0.0001	0.03976
q107	2006mj	Ia	wcc1	8	02:09:03.042	−03:28:27.832	0.650	0.009	0.6514	0.0001	0.02406
q108	2006mi	Ia	wcc3	9	02:05:55.040	−04:00:53.216	0.622	0.005	0.6231	0.0001	0.02476
q112	2006ml	Ia	wbb9	3	01:08:43.977	−00:31:36.593	0.637	0.003	…	…	0.03642
q114	2006mm	Ia	wbb6	6	01:08:48.662	+00:17:22.315	0.701	0.011	0.6875	0.0002	0.02730
q125	2006mn	Ia	wbb6	1	01:07:48.392	−00:06:35.454	0.347	0.004	0.3486	0.0004	0.03112
q150	…	Unk	wdd5	16	02:31:18.622	−08:07:11.563	…	…	…	…	0.03639
r184	2006sa	IIP	wcc9	6	02:05:14.944	−04:48:51.685	…	…	0.1609	0.0002	0.02442
r185	…	Ia	wbb8	3	01:11:48.238	−00:29:49.579	0.179	0.006	0.1800	0.0003	0.02423
r186	2006sb	Ia	wcc5	8	02:06:30.312	−04:05:30.553	0.313	0.004	0.3126	0.0001	0.02101
r190	2006sc	Ia	wcc7	15	02:10:10.226	−04:44:12.545	0.355	0.007	0.3568	0.0002	0.02261
r192	…	Gal	wcc9	13	02:05:23.959	−04:52:16.485	…	…	0.6336	0.0001	0.02426
r193	2006sm	Ia	wdd4	2	02:33:29.487	−08:30:11.879	0.609	0.005	…	…	0.03296
r195	2006si	Ia	wcc1	5	02:09:51.320	−03:43:32.520	0.542	0.008	0.5424	0.0001	0.02335
r196	2006sh	IIn	wcc1	5	02:09:11.064	−03:44:42.104	0.260	0.010	0.2639	0.0001	0.02275
r199	2006sl	Ia?	wdd7	6	02:32:15.952	−08:48:34.335	0.410	0.010	0.4180	0.0002	0.02808
r200	2006sd	Ia	wbb1	7	01:14:24.151	+01:02:39.488	0.283	0.007	…	…	0.03124
r204	…	Gal	wcc1	7	02:09:47.393	−03:34:25.676	…	…	0.4212	0.0001	0.02441
r205	…	IIn	wcc1	7	02:09:37.948	−03:31:20.238	…	…	0.0517	0.0004	0.02574
r206	2006se	Ia	wbb4	11	01:14:48.050	+00:06:39.370	0.610	0.010	0.6108	0.0003	0.03126
r207	2006sf	Ia	wcc2	11	02:08:11.658	−03:51:40.230	0.560	0.010	0.5616	0.0006	0.02335

Table 6
(Continued)

ESSENCE ID	IAU ID	Type	Subfield	Amp	R.A. (J2000)	decl.	z_{SNID}	σ_z	z_{GAL}	σ_{zGAL}	$MW_{E(B-V)}$
r209	2006sg	Ia	wcc2	12	02:08:13.041	−03:46:21.937	0.428	0.003	0.4451	0.0002	0.02290
r212	2006sj	Ia	wcc1	15	02:10:22.419	−03:33:09.269	…	…	0.6535	0.0004	0.02468
r213	2006sk	Ia	wcc4	16	02:10:33.800	−04:04:03.845	0.321	0.008	0.3270	0.0001	0.02228
r215	…	Unk	wcc7	4	02:08:55.716	−04:59:46.063	…	…	…	…	0.02095
r225	2006sn	Ia	wcc9	13	02:06:18.251	−04:51:33.148	0.415	0.006	0.4149	0.0001	0.02228
r230	2006so	Ia	wdd7	12	02:33:49.152	−08:59:15.768	0.259	0.005	…	…	0.03030
r311	2006sp	Ia	wbb8	3	01:10:55.171	−00:27:52.289	…	…	0.7989	0.0002	0.02510
r314	…	Gal	wcc4	5	02:09:59.003	−04:18:53.926	…	…	0.1092	0.0003	0.02445
r317	…	Ia	wbb1	5	01:13:24.658	+00:51:27.757	0.736	0.005	0.3361	0.0004	0.02550
r318	2006sq	Ia	wcc2	2	02:07:11.267	−03:57:07.942	0.222	0.002	…	…	0.02526
r322	2006tg	Ia	wcc9	8	02:04:14.168	−04:40:18.623	0.521	0.010	0.5138	0.0002	0.02531
r328	2006th	II	waa1	1	23:29:00.954	−08:54:04.953	…	…	0.1463	0.0002	0.03533
r329	…	Gal	wcc2	16	02:07:48.017	−03:29:12.632	…	…	0.6209	0.0001	0.02405
r331	…	Gal	waa1	14	23:30:49.841	−08:32:37.728	…	…	0.4225	0.0003	0.02973
r334	2006ti	II	waa1	3	23:29:13.133	−08:47:57.762	…	…	0.2051	0.0004	0.02897
s340	2006tj	Ia	wbb3	4	01:09:23.284	+00:42:42.313	0.528	0.006	…	…	0.02954
s346	2006tl	Ia	wbb9	1	01:09:17.282	−00:40:27.967	0.270	0.010	0.2721	0.0006	0.03367
s347	2006tk	Ia	wbb6	8	01:07:52.640	+00:27:55.293	0.313	0.003	…	…	0.02954
s349	2006tm	Ia	wbb6	12	01:09:17.297	+00:09:11.389	0.220	0.007	0.2156	0.0002	0.02782
s350	2006to	Ia	wcc2	1	02:07:34.387	−04:00:04.177	0.682	0.010	0.6834	0.0001	0.02453
s351	2006tp	Ia	wcc4	1	02:09:14.040	−04:37:11.970	0.720	0.006	0.7275	0.0002	0.02118
s353	2006tr	Ia?	wdd3	4	02:28:29.532	−07:53:28.493	0.581	0.010	0.5956	0.0002	0.02658
s354	…	Ia?	wcc9	10	02:06:10.482	−05:05:23.000	…	…	0.5588	0.0004	0.02130
s355	2006tn	Ia	wcc9	10	02:05:36.019	−05:08:46.272	0.670	0.010	0.6734	0.0002	0.02461
s362	2006tq	Ib-pec	wcc4	8	02:10:00.697	−04:06:00.903	0.262	0.001	0.2622	0.0001	0.02390
s370	2006tu	Ia	wdd2	2	02:29:56.534	−07:59:50.850	0.439	0.005	0.4394	0.0002	0.03014
s371	…	II?	wbb8	11	01:12:57.431	−00:26:54.525	…	…	0.2499	0.0001	0.02858
s372	…	Ia	wcc2	16	02:08:24.257	−03:27:32.636	0.706	0.010	0.7076	0.0014	0.02480
s373	2006tt	Ia	wcc4	12	02:10:47.935	−04:24:56.952	0.630	0.003	…	…	0.02041
s374	2006tv	Ia?	wdd4	9	02:35:34.225	−08:34:22.069	0.757	0.010	0.7581	0.0002	0.02855
s375	2006ts	IaT	wcc1	15	02:10:18.687	−03:32:26.335	0.551	0.006	0.5569	0.0003	0.02473
s377	2006tw	IaT	wbb6	6	01:08:54.227	+00:17:56.510	…	…	0.3987	0.0005	0.02658
s378	2006tx	SN?	wbb9	11	01:10:26.793	−00:34:07.640	…	…	0.5005	0.0002	0.02851
s379	2006ty	Ia	wbb3	10	01:10:45.361	+00:34:04.408	0.181	0.004	0.1923	0.0001	0.02689
s380	…	Ia	wcc7	2	02:09:00.048	−05:07:41.787	…	…	0.6355	0.0002	0.02096
s383	2006tz	SN?	wcc4	13	02:10:27.034	−04:17:08.159	…	…	0.3920	0.0001	0.02371
x005	2007sz	IIP	wcc8	2	02:07:00.230	−05:06:08.212	0.046	0.005	…	…	0.02235
x016	2007td	IIn	wcc3	5	02:04:26.895	−03:44:18.859	…	…	0.3442	0.0002	0.02666
x017	2007ta	Ia	wbb4	1	01:13:15.801	−00:01:31.428	0.418	0.006	0.4222	0.0004	0.02770
x020	2007te	Ia	wcc1	7	02:09:29.402	−03:35:35.054	0.686	0.008	…	…	0.02540
x022	2007sx	IIP	wbb9	9	01:10:09.249	−00:42:08.035	0.12	0.01	0.1171	0.0004	0.03418
x024	2007sy	II?	wbb1	12	01:15:25.989	+00:49:06.597	0.19	0.01	0.1936	0.0002	0.03165
x025	2007tb	Ia	wbb1	12	01:14:41.252	+00:46:51.824	0.372	0.008	0.3553	0.0001	0.03295
x027	…	Unk	wcc2	12	02:08:15.486	−03:49:35.804	…	…	…	…	0.02259
x028	2007tc	Ia	wbb4	13	01:14:46.894	+00:17:06.778	0.609	0.007	0.600	0.0010	0.03209
x033	2007tf	Ia	wbb6	10	01:09:59.349	−00:01:06.947	0.405	0.007	0.4062	0.0012	0.03114
x034	2007th	Ia	wcc7	11	02:10:57.582	−05:00:24.789	0.508	0.003	…	…	0.02021
x035	…	Gal	wcc9	11	02:05:24.988	−05:03:33.228	…	…	0.4029	0.0002	0.02415
x038	2007tg	Ia	wcc9	15	02:06:10.505	−04:42:23.286	0.512	0.008	…	…	0.02367
x039	…	Ia	wdd3	15	02:29:18.063	−07:39:01.433	0.771	0.004	…	…	0.02975
x055	2007tk	Ia?	wdd5	6	02:30:24.609	−08:17:54.401	…	…	0.3495	0.0002	0.03726
x066	2007tj	Ia	wcc4	14	02:11:04.611	−04:11:50.056	0.331	0.003	0.3286	0.0002	0.02047
x068	…	Gal	wdd5	14	02:31:12.905	−08:18:18.552	…	…	0.4350	0.0002	0.03451
x071	2007ti	Ia	wcc7	16	02:10:09.836	−04:39:49.342	0.476	0.008	0.4865	0.0002	0.02324
x072	…	Gal	wcc8	16	02:08:37.294	−04:37:35.354	…	…	0.1919	0.0001	0.02107
x076	2007tn	II	wdd6	2	02:28:14.790	−08:36:32.198	…	…	…	…	0.03026
x077	2007tp	Ia	wdd8	2	02:30:23.940	−09:13:39.846	0.517	0.009	0.520	0.0010	0.03026
x080	2007tl	Ia	wbb8	6	01:11:04.912	−00:15:43.364	0.374	0.008	0.3731	0.0002	0.02838
x084	…	Gal?	wdd3	12	02:29:20.643	−07:51:00.932	…	…	…	…	0.02666
x085	2007to	Ia	wdd9	12	02:29:42.061	−09:02:05.252	0.648	0.008	0.6345	0.0001	0.03208
x089	2007tm	IaT	wcc3	15	02:06:04.748	−03:32:29.261	0.5	0.05	0.4919	0.0001	0.02307
x093	…	Ia	wdd9	11	02:29:43.134	−09:06:54.931	…	…	0.5004	0.0001	0.03314
x103	…	Ia?	wbb5	4	01:10:48.009	+00:13:36.806	…	…	…	…	0.02585
x107	2007tq	Ia	wdd3	12	02:29:23.345	−07:52:27.686	0.145	0.002	0.1462	0.0009	0.02682

Table 6
(Continued)

ESSENCE ID	IAU ID	Type	Subfield	Amp	R.A. (J2000)	decl.	z_{SNID}	σ_z	z_{GAL}	σ_{zGAL}	$MW_{E(B-V)}$
x113	…	II?	wdd4	16	02:34:36.128	−08:01:11.116	…	…	…	…	0.03962
y117	…	Unk	wcc5	16	02:08:14.332	−04:05:09.772	…	…	…	…	0.02299
y118	2007tu	IIP	wbb7	1	01:14:05.219	−00:36:25.629	0.222	0.007	…	…	0.02995
y122	2007tx	Ic	wdd6	2	02:28:33.314	−08:35:25.690	0.674	0.006	0.6764	0.0001	0.03035
y123	…	Gal	wdd7	2	02:32:56.953	−09:08:21.287	…	…	0.1939	0.0007	0.02755
y125	2007tv	Ia	wcc9	3	02:05:13.326	−05:01:42.415	0.310	0.006	0.3108	0.0003	0.02459
y126	…	Gal	wcc9	3	02:04:27.408	−05:01:59.892	…	…	0.7944	0.0002	0.02355
y127	2007ty	Ia	wdd6	5	02:28:34.381	−08:23:49.491	0.518	0.003	…	…	0.03131
y131	2007tw	SN?	wcc9	11	02:05:32.964	−05:02:46.626	…	…	0.6654	0.0001	0.02404
y134	2007ts	Ia	wbb6	8	01:07:58.159	+00:27:48.972	0.336	0.006	0.3149	0.0002	0.02953
y136	2007tz	Ia?	wdd8	8	02:30:07.153	−08:43:09.354	…	0.001	0.5200	0.0010	0.03795
y137	2007tt	Ia	wbb8	6	01:11:20.516	−00:12:19.423	0.368	0.009	0.3741	0.0004	0.02732
y142	2007ud	Ia	wdd8	1	02:30:13.145	−09:15:39.519	0.592	0.006	0.5820	0.0010	0.02938
y143	2007ub	Ia	wcc2	3	02:07:24.132	−03:51:55.226	0.466	0.008	0.4642	0.0003	0.02487
y145	2007 ua	Ia	wbb3	10	01:10:31.955	+00:35:49.434	0.555	0.001	0.5514	0.0003	0.02788
y146	…	Unk	wdd6	12	02:29:26.184	−08:27:52.797	…	…	…	…	0.03430
y151	2007uc	Ia?	wcc4	16	02:10:15.529	−04:04:06.465	…	…	0.5837	0.0006	0.02255
y154	2007ug	Ia?	wcc7	5	02:09:36.845	−04:51:52.280	…	…	0.6540	0.0001	0.02246
y155	…	PISN?	wbb6	6	01:07:56.085	+00:17:41.484	…	…	0.7973	0.0000	0.03096
y156	2007ue	Ia	wbb9	7	01:09:09.843	−00:14:01.124	…	…	0.6614	0.0004	0.03364
y158	2007uf	Ia	wcc5	7	02:06:30.881	−04:09:55.047	…	…	0.4856	0.0001	0.02182
y163	2007uh	Ia	wcc3	9	02:06:05.200	−04:01:37.458	0.640	0.003	0.630	0.0010	0.02411
y173	…	Ic?	wdd4	13	02:35:34.821	−08:19:07.016	…	…	0.4078	0.0002	0.03593
y175	2007ui	Ia	wdd4	16	02:34:57.445	−08:03:57.919	0.421	0.009	0.4130	0.0002	0.03688
y177	2007uj	Ia	wdd4	2	02:33:19.036	−08:32:30.217	0.303	0.004	…	…	0.03212
z179	…	Gal	wbb8	4	01:11:21.637	−00:22:45.114	…	…	0.4462	0.0007	0.02664
z180	2007uk	Ia	wbb8	4	01:10:55.006	−00:22:53.197	0.447	0.004	…	…	0.02561
z181	2007ul	Ia	wcc8	7	02:07:16.534	−04:42:23.201	0.604	0.004	0.620	0.0010	0.02248
z183	2007un	Ia	wbb1	8	01:14:22.736	+01:07:45.632	0.287	0.006	0.2806	0.0001	0.03050
z184	2007up	Gal	wcc4	3	02:09:56.068	−04:28:57.352	…	…	0.6116	0.0002	0.02245
z185	2007uv	Ia	wbb4	9	01:15:11.994	−00:02:08.387	0.414	0.005	0.4068	0.0001	0.02924
z187	2007um	Ia	wbb5	13	01:12:29.210	+00:17:01.211	0.293	0.004	…	…	0.03491
z195	…	Unk	wdd9	12	02:29:47.674	−09:01:08.431	…	…	…	…	0.03279
z200	2007uo	Ia	wbb1	13	01:14:43.186	+00:54:27.657	0.457	0.005	0.4548	0.0002	0.03175
z202	2007uq	Ia	wcc3	3	02:04:21.320	−03:54:10.960	0.220	0.005	0.2205	0.0002	0.02510
z203	2007ur	Ia?	wcc2	15	02:08:41.591	−03:34:10.527	…	0.001	0.2500	0.0010	0.02317
z204	2007us	Ia	wdd3	2	02:27:54.863	−08:00:55.479	…	…	0.6201	0.0002	0.03008
z205	2007ut	Ia	wdd8	2	02:30:23.642	−09:12:20.022	0.416	0.020	…	…	0.03042
z208	2007uu	Ia	wbb1	5	01:14:01.011	+00:53:47.598	0.502	0.008	0.5300	0.0010	0.03017

Notes. 1. Ia—type Ia supernova, no sub-type reported. 2. IaT—similar to the overluminous type Ia supernovae SN 1991 T or SN 1999aa. 3. IaP—similar to peculiar type Ia supernovae SN 2000cx or SN 2002cx. 4. Ib—type Ib supernova, no sub-type reported. 5. Ib-pec—type Ib supernova with peculiar spectral features. 6. Ic—type Ic supernova, no sub-type reported. 7. II—type II supernova, no sub-type reported. 8. IIn—type II supernova with narrow emission lines. 9. IIP—type II supernova with a "plateau" in the light curve. 10. II-pec—type II supernova with peculiar spectral features. 11. Classifications followed by a "?" are not definitively spectroscopically typed. 12. PISN?—Possible pair-instability supernova (P. Garnavich 2016, private communication). 13. Gal—Galaxy, sub-types are reported in B. E. Tucker et al. (2014, in preparation). 14. AGN—Active galactic nucleus. 15. Unk—Not observed or could not be classified based on spectra. z_{SNID} and z_{GAL} are reported in the heliocentric frame, and must be converted into the cosmic microwave background (CMB) frame, while accounting for local peculiar velocities at low-z. For this work, we have employed the Milky Way reddening values from Schlegel et al. (1998), rather than the updated values provided by Schlafly et al. (2012), to facilitate the combination of our objects with literature samples.

offset by $1''$. As this is much larger than the typical astrometric uncertainty, we adopt the procedure used by Rest et al. (2014), and find that an offset of 0.3 pixels produces a sub-percent impact on photometry. Since the uncertainty is related to the SNR, we expect increased dispersion at high-z; however, our cadence provides $S/N > 10$ for even our highest redshift objects, and we do not find any net bias in the recovered astrometry of known sources with magnitude. We adopted a fixed valued of 0.005 mag in both filters to account for the systematics arising from astrometric uncertainties.

6.5. Uncertainties in Determining the Airmass Relation

An error in the slope of the airmass relation would lead to an error in extrapolating the zero points from the Landolt standard fields to the ESSENCE fields, and between the ESSENCE fields. We mitigate this uncertainty by requiring the images we use to extrapolate the zero point for a given image to have a difference in airmass smaller than 0.5. We introduce a 10% error in the airmass relation and propagate the error to our photometric catalogs. Such a large error is extremely unlikely, and would be visually apparent, as we obtained images of standard fields over an extended range in airmass, but allows us

Table 7
Photometry of ESSENCE Objects

MJD	Passband	$Flux_{25}$	σ_{Flux}
	k425		
52990.0582	*R*	−0.331500	0.561100
52990.0745	*I*	−0.013500	1.108300
52994.0601	*R*	0.468100	0.468700
52994.0772	*I*	1.395600	0.782300
53268.1072	*R*	0.029500	0.836900
53268.1484	*I*	−0.254100	1.248500
53283.1311	*R*	−0.815500	0.746300
53283.1629	*I*	1.064200	1.631700
53289.0561	*R*	0.149500	0.764900
53289.0726	*I*	−1.360000	1.253400
53293.0558	*I*	1.089600	1.544700
53297.0640	*R*	−0.521300	0.616900
53297.0809	*I*	−1.181900	0.945800
53301.0728	*R*	0.085300	1.094000
53301.0973	*I*	−1.519200	1.085500
53315.0736	*R*	0.777700	0.493500
53315.0906	*I*	0.207800	0.852200
53323.0829	*R*	10.472000	0.477600
53323.1006	*I*	11.788600	0.649700
53329.0363	*R*	17.830900	0.655000
53329.0533	*I*	24.461000	0.892200
53342.0814	*R*	24.361700	0.582500
53342.0984	*I*	30.781000	0.963700
53346.0734	*R*	20.966300	0.543200
53346.0919	*I*	25.465800	1.022600
53350.0550	*R*	17.523900	1.083800
53350.0724	*I*	21.250500	1.189000
53358.0431	*R*	10.427300	0.720000
53358.0720	*I*	16.345000	0.915900
53360.0755	*R*	10.464500	1.257200
53360.1073	*I*	14.251400	2.462600
53385.0554	*R*	1.924400	0.784900
53385.0589	*I*	4.661300	1.151400
53639.0843	*R*	−0.178200	0.629700
53639.1007	*I*	0.131800	0.934900

to place an upper limit on the resulting systematic error in magnitudes.

We find that a $\pm 10\%$ error in the airmass term causes a ∓ 0.001 mag error in *R* and a ∓ 0.002 mag error in *I* (see Figure 14). The slightly larger effect in *I*, despite the weaker extinction coefficient, is a result of the smaller number of *I* images overall, and the larger fraction of *I* calibration images that were observed at high airmass, relative to *R*.

We also compute the mean difference as a function of magnitude to look for any residual trends. This is critical for SN Ia measurements which span a wide range in magnitude as a function of redshift, light curve shape, and host-galaxy extinction. We find weak $<0.1\%$ trends as a function of magnitude.

6.6. Uncertainties in Determining the Photometric Transformation to the Landolt System

Extinction caused by dust in the host galaxies of the supernovae makes them appear fainter than predicted for their redshift, mimicking the effect of the dark energy. Accurate measurements of SN Ia color are critical in constraining the reddening, and allow us to disentangle the effect of dust from the dark energy signal.

Because high-redshift SN Ia surveys are deep, but cover a small solid angle, they are inefficient at finding large numbers of nearby supernovae. Analysis of the high-*z* samples requires low-*z* SN Ia from the literature as an anchor for cosmological measurements (Hamuy et al. 1993; Riess et al. 1999; Jha et al. 2006; Hicken et al. 2009b, 2012; Contreras et al. 2010; Ganeshalingam et al. 2010; Stritzinger et al. 2011). Thus, any *absolute* zero point offsets, even if arising from inaccuracies in the nearby sample, are a common source of systematic error for high-redshift surveys. Because most nearby surveys are tied to the Landolt network, we can estimate a lower bound to this offset by examining how the ESSENCE data are tied to the Landolt system.

In addition, any errors in our *R* and *I* flux scaling *relative* to each other would distort the observed color of the entire sample. At the typical redshifts probed by ESSENCE, our *RI* photometry covers the rest-frame *BV*, and our inferred host galaxy extinction is related to the measured rest-frame color excess, $E(B-V)$. If we assume that the slope of the reddening law, R_V, in the host galaxies of our SN Ia is similar to our own Galaxy ($R_V \approx 3.1$), then any error in our measured color would lead to an error $\sim$3 times larger in the extinction, A_V, and the distance modulus, μ.

SN Ia surveys like ESSENCE are therefore particularly sensitive to systematics affecting measured colors. An error in the photometric transformation can take the form of an error in determining the slope of the color law, or a residual difference in magnitudes around the intercept. The effect of an error in the slope of the color relation is small, as the error is on the order of the product of the error in the color term and the difference between the mean color of our field stars and the color of BD $+17°4708$. We measure the effect of an error in the color term using synthetic photometry, as described in Appendix B.2, and find that a ± 0.02 error in the slope of the color relation would lead to a $\sim\pm 0.003$ mag systematic error in the magnitudes of field stars and derived zero points. We conservatively adopt an error of 0.005 mag as the systematic error resulting from an error in the estimate of the color term.

We measure the residual difference in magnitudes, $m_{4\,\mathrm{m}} - m_{\mathrm{Landolt}}$, for our calibration fields around $R - I = 0.32$ mag in our standard fields and find these to be -0.003 mag and -0.001 mag in *R* and *I,* respectively, with an uncertainty of $\sim$0.001 mag in both bands (see Figure 15). The dispersions about the mean residual are $\sim 1\%$ in both *R* and *I*. The residual is consistent with zero in *I*, and of low significance in *R*. We adopt these values as systematic uncertainties in the absolute zero point.

6.6.1. Comparison to the Sloan Digital Sky Survey

While we cannot directly compare our magnitudes to Landolt magnitudes in our science fields, we use stars selected from SDSS DR7 and converted onto the Landolt network using transformation equations. This procedure has some limitations: the SDSS imaging is not as deep as MOSAIC II images of the ESSENCE fields, and SDSS magnitudes converted onto the Landolt network have large statistical uncertainties associated with the transformation between two dissimilar photometric systems. In addition, the *wcc* field is outside the SDSS footprint, and is not included in the analysis. However, as the SDSS photometry was not used in determining our photometric

Table 8
Quantum Efficiency of the MOSAIC II Imager

Wavelength	Transmission (%)								
(Å)	CCD 1	CCD 2	CCD 3	CCD 4	CCD 5	CCD 6	CCD 7	CCD 8	Average
3000	8.90	9.70	7.60	7.80	9.50	9.40	8.40	9.60	8.86
3200	18.00	18.90	15.80	16.10	18.50	18.50	18.50	19.30	17.95
3340	22.70	27.90	22.40	23.00	26.40	27.10	25.40	27.60	25.31
3650	48.40	52.60	42.10	43.50	53.00	52.70	49.20	54.90	49.55
3800	62.80	56.10	56.20	57.10	62.10	61.90	58.20	65.80	60.02
4050	67.50	68.80	57.90	60.90	63.90	66.90	63.40	72.10	65.17
4500	74.00	74.40	63.60	65.60	70.70	72.50	70.20	78.30	71.16
5000	77.90	79.40	69.90	73.60	76.10	77.80	75.00	81.40	76.39
5500	83.20	83.90	75.30	77.70	81.60	81.40	80.30	86.50	81.24
6000	86.80	87.00	80.30	84.40	88.30	87.70	85.10	89.70	86.16
6500	87.80	88.70	82.70	86.60	89.70	89.20	87.10	90.60	87.80
7000	84.70	86.20	82.80	84.50	88.40	86.30	85.70	88.10	85.84
7500	78.20	78.30	76.40	77.00	81.50	80.50	79.00	80.30	78.90
8000	68.40	68.80	67.00	68.00	71.90	68.10	69.50	70.10	68.97
8500	54.00	54.50	54.70	55.30	57.60	54.00	56.50	56.10	55.34
9000	39.30	40.30	40.20	44.10	41.90	39.20	41.30	40.90	40.90
9500	24.50	25.40	25.40	25.50	26.20	24.50	26.20	26.00	25.46
10000	10.90	11.60	11.80	12.20	12.00	10.60	11.80	11.70	11.57

Table 9
Photon Transmission Function of the ESSENCE Survey

Wavelength	Transmission (%)				
(Å)	QE	Filter	Optics	Atmosphere	Total
		R (c6004)			
5470	0.8018	0.0000	0.9087	0.8400	0.0000
…	…	…	…	…	…
6240	0.8760	0.7764	0.9021	0.8700	0.5338
…	…	…	…	…	…
7005	0.8546	0.4846	0.8904	0.9160	0.3378
…	…	…	…	…	…
7775	0.7454	0.1784	0.8725	0.9410	0.1092
…	…	…	…	…	…
8540	0.5431	0.0409	0.8719	0.9530	0.0185
…	…	…	…	…	…
9310	0.3111	0.0000	0.9133	0.8530	0.0000
		I (c6028)			
6940	0.8592	0.0000	0.8916	0.9060	0.0000
…	…	…	…	…	…
7635	0.7721	0.9348	0.8763	0.5660	0.3580
…	…	…	…	…	…
8330	0.6052	0.9563	0.8674	0.9420	0.4729
…	…	…	…	…	…
9030	0.3959	0.0070	0.9007	0.9330	0.0023
…	…	…	…	…	…
9725	0.1912	0.0047	0.9275	0.9490	0.0008
…	…	…	…	…	…
10425	0.0000	0.0047	0.9365	0.9690	0.0000

calibration, it provides a useful, independent test on our photometric accuracy.

We cross-match stars from Stetson (2005) in SDSS, and extract Übercal (Padmanabhan et al. 2008) corrected magnitudes. We select from SDSS only objects with clean photometry, point-source PSFs, *gri* uncertainties <0.1 mag and $\sigma_z < 0.15$ mag without a corresponding entry in the DR7 QSOBest catalog, satisfying

$$\begin{aligned} 0.95 < u - g < 2.75\,\mathrm{mag},\\ -0.01 < g - r < 1.78\,\mathrm{mag},\\ -0.12 < r - i < 2.74\,\mathrm{mag},\ \text{and}\\ -0.13 < i - z < 1.58\,\mathrm{mag}, \end{aligned}$$

and close proximity to the stellar locus are selected from SDSS (see Figure 16).

We use simple linear transformations for stars with $r - i < 0.8$, determined using the "LINMIX_ERR" routine (Kelly 2007) available in the IDL Astronomy Library.[38] We derive the following transformations (see Figure 17) using >1300 measured stars:

$$\begin{aligned} R_L &= r - (0.303 \pm 0.006)(r - i) - (0.133 \pm 0.002)\\ I_L &= i - (0.213 \pm 0.007)(r - i) - (0.388 \pm 0.002). \end{aligned} \quad (7)$$

We find large intrinsic dispersions of ~0.025 mag in the relations between the SDSS and Landolt photometry for both R_L and I_L. This dispersion is inherent in the transformation between two photometric systems with very dissimilar transmissions, and significantly different dynamic ranges, and further justifies our choice to base the calibration of the Blanco natural system on the Landolt standard network. We do not find any significant trend in the residuals of transformed R_L with $g - r$, or I_L with $i - z$. We apply these transformations to SDSS stars in our science fields, selected using the same criteria, to derive their Landolt magnitudes.

We compare our tertiary photometric catalogs for the science fields to SDSS stars, selected using the same criteria as above, converted to Landolt using our derived transformations. No significant field-to-field differences are found. We measure the offset between the CTIO Blanco natural system and these transformed stars around $R - I = 0.32$ mag as in the standard fields, and found offsets (in the sense of Blanco magnitude *minus* transformed SDSS magnitude) of 0.009 ± 0.03 mag in *R*, and 0.013 ± 0.03 mag in *I*, consistent with zero. The large

[38] http://idlastro.gsfc.nasa.gov/

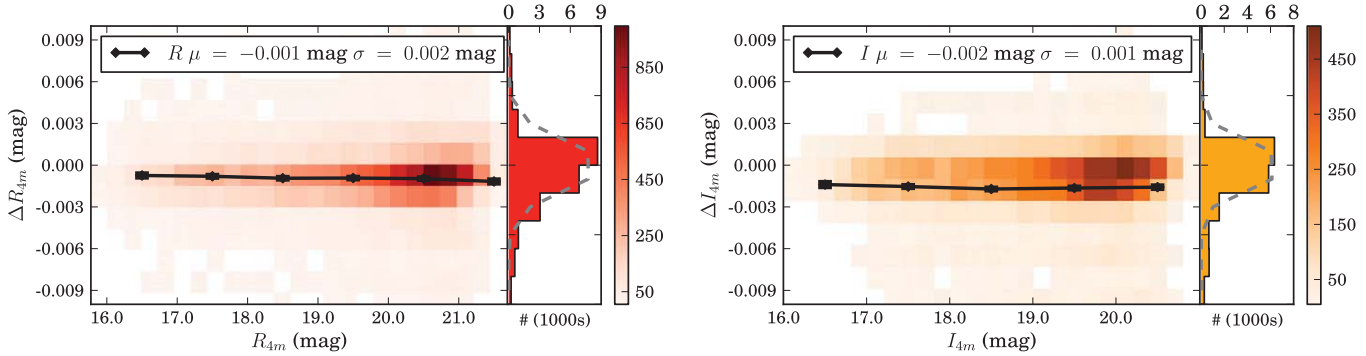

Figure 14. Differences in (left) *R*- and (right) *I*-band photometry with a 10% error in the slope of the airmass relation (in the sense of with offset *minus* no offset), binned as a function of magnitude (left) and for all amplifier images (right). The color bars indicate the number of amplifier images in each bin. The means in bins with 1 mag widths are overplotted (black diamonds). We find a resulting −0.001 mag difference in the *R* band, and a −0.002 mag difference in the *I* band. Dispersions are computed using a Gaussian fit to the histogram shown at right.

uncertainties arise from the intrinsic dispersion in the transformation to *R* and *I*, as well as the *r* and *i* uncertainties that are propagated into the uncertainty on the $R - I$.

6.7. Uncertainties in Extrapolating Photometric Zero Points

We evaluate the error in determining the photometric zero point for a single amplifier by extrapolating the zero point of the image using the average of all other amplifiers of the same image, and the average of all other images that are within ±0.5 in airmass and ±100 s in exposure time, adjusted for both the difference in airmass and the difference in exposure time. We find the difference between the zero point and the extrapolated zero point to be <0.001 mag. We also construct this statistic field by field and amplifier by amplifier and find no significant difference in these sub-samples. The histogram of differences between the extrapolated and directly fitted zero points are shown in Figure 18.

Additionally, we find that the images with the largest differences between fitted and extrapolated zero points are typically taken in non-photometric conditions and fail quality tests for difference imaging. We find no significant trends in the difference between direct and extrapolated zero points with airmass, aperture correction error, exposure time, FWHM, or sky background. The standard deviations of the un-clipped data are ∼0.01 mag in both *R* and *I*. Either 3σ clipping extreme outliers or using a Gaussian to model the data reduces the estimate of the standard deviation to <0.01 mag. This is a strong indication that our internal photometric calibration is no worse than 1%.

6.8. Uncertainties in Determining the Natural System Magnitudes of BD+17°4708

The CTIO Blanco natural magnitude system adopted in this work utilizes BD+17°4708 as the fundamental spectrophotometric standard and consequently, the magnitudes of BD+17° 4708 in the natural system are close to its Landolt magnitudes by construction. However, there are several astrophysical differences between BD+17°4708 and the "typical" Landolt standard star. We determine the corrections to the first order magnitudes of BD+17°4708 in Appendix B.3. Systematic errors in the magnitudes of BD+17°4708 would lead to an error in the synthetic zero points and *k*-corrections, and the uncertainty budget is dominated by the impact of a potential unresolved binary companion.

6.9. Uncertainties in the SED of BD+17°4708

While the derivation of the magnitudes of BD+17°4708 in Appendix B relies on the PHOENIX synthetic spectral library (Hauschildt et al. 1997; Sordo et al. 2010, and references therein), the derivation of synthetic zero points requires its true SED. We use the CALSPEC determination of the SED of the BD+17°4708 and adopt a 0.5% uncertainty over 3000–10000 Å. These translate into 0.002 and 0.003 mag differences in the synthetic *R* and *I* Blanco magnitudes.

7. CONCLUSIONS

We have re-calibrated the CTIO Blanco and MOSAIC II system, with a focus on minimizing the systematic errors that originate from photometry and affect the high-redshift SN Ia measurements from ESSENCE. This calibration supersedes that presented by Miknaitis et al. (2007), and improves on it by deriving photometric transformations between the Landolt network and the Blanco natural system without employing any observations from the CTIO 0.9 m, avoiding cross-telescope systematics.

Additionally, we have selected BD+17°4708 as the fundamental spectrophotometric standard in this work. The $R - I$ color of this standard is considerably closer to the average color of Landolt network stars, as well as SN Ia around the median redshift of ESSENCE. This choice minimizes systematic errors arising from errors in determining the photometric transformation between the Landolt and Blanco natural systems.

We employed these transformations to derive secondary photometric catalogs for our Landolt calibration fields that span the MOSAIC II field of view. We demonstrated that we could accurately extrapolate zero points between the different amplifiers of the imager. Tertiary catalogs were derived for ESSENCE fields, and zero points were established for our imaging. The zero points in both passbands are stable relative to each other over the entire duration of the survey. We have provided a model of the system response of the *R* and *I* passbands used by ESSENCE, and made a comprehensive estimate of the effect of various systematics on magnitudes in both passbands.

The primary application of this work is the calibration of light curves of SN Ia discovered by ESSENCE to derive the equation of state parameter of the dark energy, *w*. We have outlined our spectroscopic follow up, and classification program to identify SN Ia within survey data, and presented

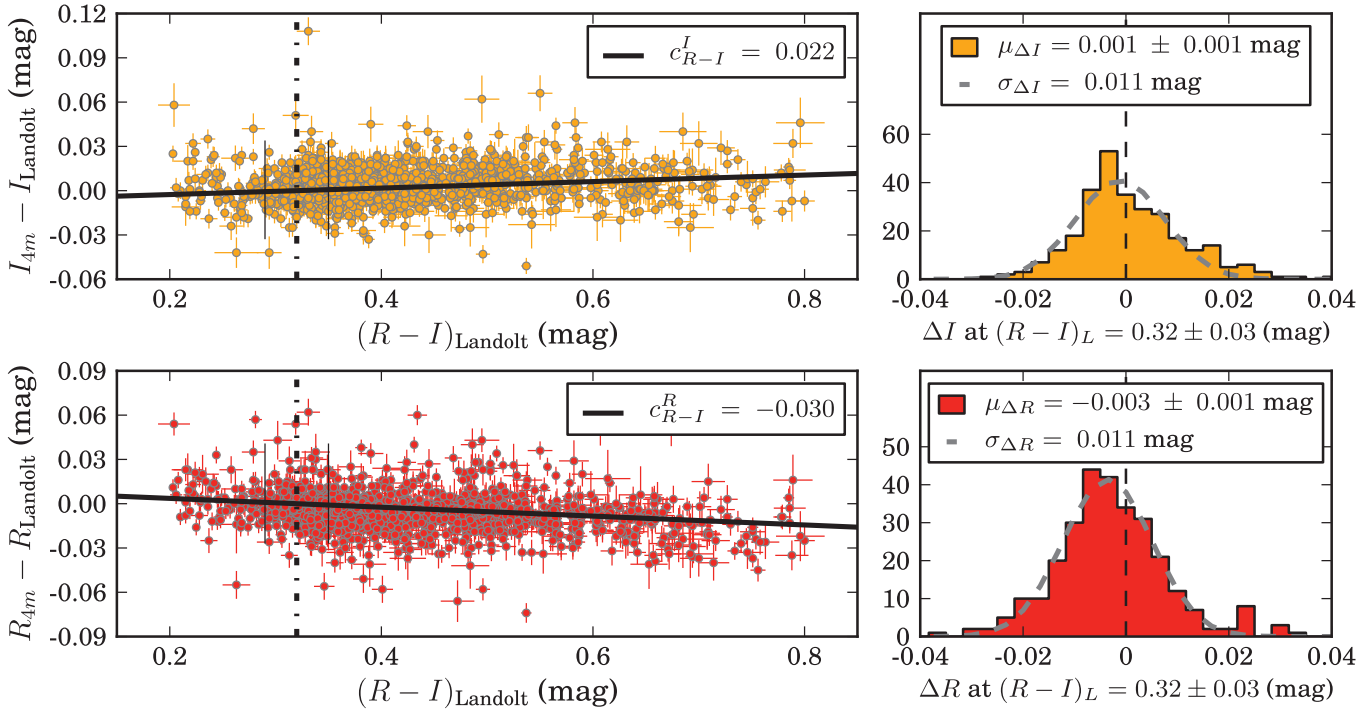

Figure 15. Differences in the (upper left) *I*- and (lower left) *R*-band magnitude between the CTIO Blanco and the Landolt network in the standard fields. The solid line indicates the slope of the color relation. The slopes are determined at an intercept of $R - I = 0.32$ mag. We examine the residuals in a range of ± 0.03 mag (this range is indicated by short vertical lines in the left panels) around the color intercept. We find the differences in both *R* (lower right) and *I* (upper right) are consistent with zero, indicating that there is no significant residual offset after the color transformation is determined.

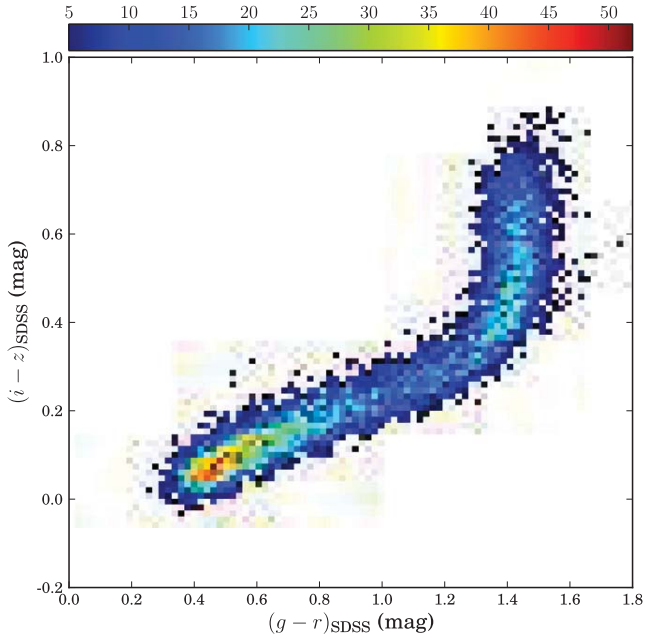

Figure 16. Color–color diagram of SDSS stars in ESSENCE fields. Only stars with $r - i < 0.8$ are used to derive transformations to Landolt and assess our absolute photometric consistency.

calibrated light curves in the CTIO Blanco natural system of 213 SN Ia discovered by ESSENCE.

There remain several potential areas for improvement where the calibration presented in this paper may be further refined. Our imaging of Landolt standard fields was obtained during our 2006–2007 observing seasons. Consequently, we only use science images obtained on the same nights to derive our tertiary catalogs, rather than all survey images. While there are clear changes in the zero points over the course of the survey, the lack of standard field imaging covering the same range of time prevents us from deriving the absolute CTIO-to-Landolt photometric transformation as a function of time. As our fundamental spectrophotometric standard, BD+17°4708, was not directly observed using the CTIO Blanco, we derived estimates of its natural system magnitudes using the CTIO-to-Landolt transformations, together with Landolt photometry and the PHOENIX synthetic spectral library, to characterize the effect of metallicity, surface gravity, and extinction. However, the principal shortcoming of the ESSENCE SN Ia photometry remains its lack of multi-color information. This increases our sensitivity to priors on the colors or extinction of SN Ia. Nevertheless, this work demonstrates that the systematic errors from photometry are ~1% in both *R* and *I*. This represents a better understanding of the systematic errors arising from photometric calibration, and an overall reduction of its impact on the ESSENCE systematic error budget.

In future work, we will combine our calibrated light curves with our spectroscopic observations as well as SN Ia host galaxy information (B. E. Tucker et al. 2014, in preparation) to derive accurate distance moduli from ESSENCE. We will combine our measurements with those from other low and high-redshift SN Ia surveys to place constraints on cosmological parameters.

G.N. is supported by NSF award AST-0507475 and the Department of Energy. Based in part on observations obtained at the Cerro Tololo Inter-American Observatory (CTIO), part of the National Optical Astronomy Observatory (NOAO),

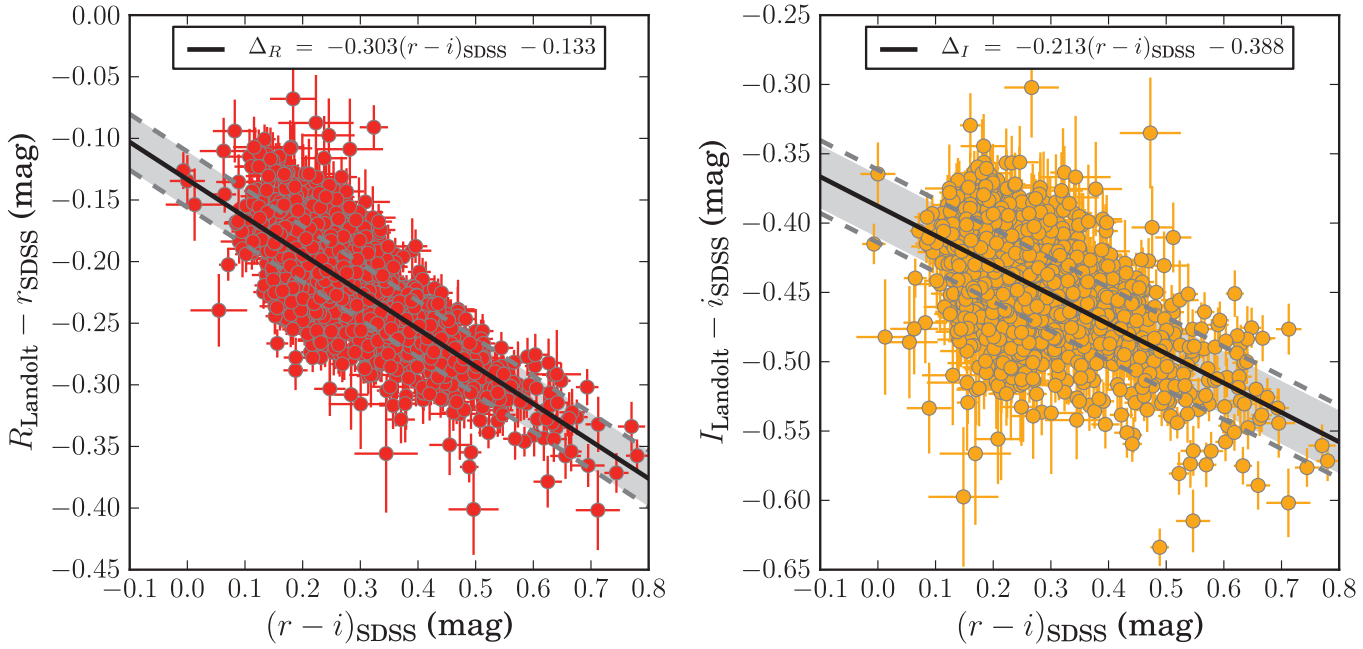

Figure 17. Transformations between the Landolt and SDSS photometric system using stars observed by Stetson for *R* (left) and *I* (right). The shaded gray region enclosed between dashed gray lines indicates the intrinsic dispersion in the fit and is ∼0.025 mag for both transformations.

which is operated by the Association of Universities for Research in Astronomy, Inc. (AURA) under cooperative agreement with the National Science Foundation (NSF); the European Southern Observatory, Chile (ESO Programmes 170. A-0519 and 176.A-0319); the Gemini Observatory, which is operated by the Association of Universities for Research in Astronomy, Inc., under a cooperative agreement with the NSF on behalf of the Gemini partnership: the NSF (United States), the Particle Physics and Astronomy Research Council (United Kingdom), the National Research Council (Canada), CONICYT (Chile), the Australian Research Council (Australia), CNPq (Brazil) and CONICET (Argentina) (Programs GN-2002B-Q-14, GS-2003B-Q-11, GN-2003B-Q-14, GS-2004B-Q-4, GN-2004B-Q-6, GS-2005B-Q-31, GN-2005B-Q-35); the *Magellan* Telescopes at Las Campanas Observatory; the MMT Observatory, a joint facility of the Smithsonian Institution and the University of Arizona; and the F.L. Whipple Observatory, which is operated by the Smithsonian Astrophysical Observatory. Some of the data presented herein were obtained at the W. M. Keck Observatory, which is operated as a scientific partnership among the California Institute of Technology, the University of California, and the National Aeronautics and Space Administration. The Observatory was made possible by the generous financial support of the W. M. Keck Foundation.

A.V.F.'s group at UC Berkeley received additional assistance from NSF grants AST-0908886 and AST-1211916, the TABASGO foundation, and the Christopher R. Redlich fund. The Dark Cosmology Centre is funded by the Danish National Research Foundation. The ESSENCE survey team is very grateful to the scientific and technical staff at the observatories we have been privileged to use.

The survey is supported by the U.S. National Science Foundation through grants AST-0443378 and AST-0507475. The Dark Cosmology Centre is funded by the Danish National Research Foundation.

Our project was made possible by the survey program administered by NOAO, and builds upon the data reduction pipeline developed by the SuperMACHO collaboration. `IRAF` is distributed by the National Optical Astronomy Observatory, which is operated by AURA under cooperative agreement with the NSF.

We made extensive use of the Odyssey Cluster administered by the FAS-IT Research Computing Group at Harvard, and are very grateful to the staff there.

J.M.S. is supported by an NSF Astronomy and Astrophysics Postdoctoral Fellowship under award AST-1302771. A.C. acknowledges support from grant IC120009 awarded to the Millennium Institute of Astrophysics, MAS, by the Ministry of Economy, Development and Tourism, and grant Basal CATA PFB 06/09 from CONICYT..

Facilities: Blanco (MOSAIC II), CTIO:0.9 m (CFCCD), Gemini:South (GMOS), Gemini:Gillett (GMOS), Keck:I (LRIS), Keck:II (DEIMOS, ESI), VLT (FORS1), Magellan: Baade (IMACS), Magellan:Clay (LDSS2).

APPENDIX A
ESTIMATION AND PROPERTIES OF THE ILLUMINATION CORRECTION

Flat-field images obtained with the CTIO Blanco are corrected using an illumination correction derived from science images as described in Section 3.1. Here we detail the estimation of the illumination corrections and their time dependence, and quantify the associated systematic errors.

A.1. Deriving the Illumination Correction

We create our illumination corrections using the following prescription.

1. Create a master dome flat from the set of dome flats, F_D.
2. Calibrate science frames, F_S, with the master dome flats.
3. Mask out all stars in the resulting science frames.

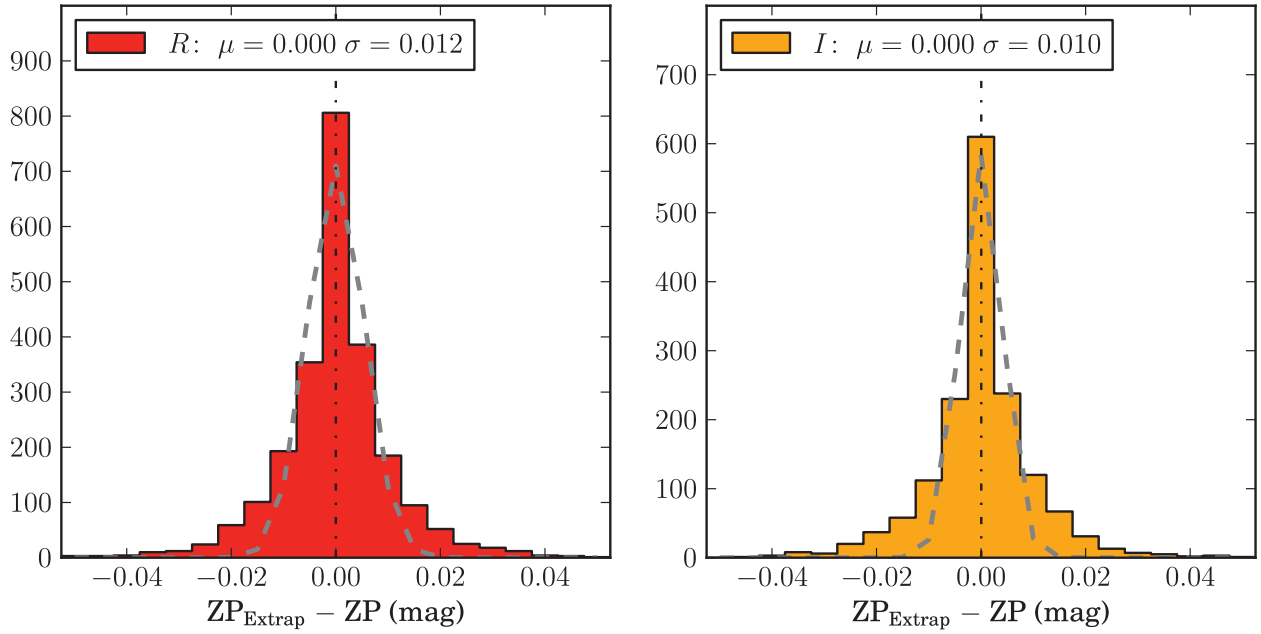

Figure 18. Differences between the fitted zero point of an amplifier image and the zero point extrapolated from the average of the other amplifiers of the same image, in *R* (left) and *I* (right). We find no net offset between the directly fitted and extrapolated zero points. In addition, the standard deviation of the residuals normalized by the uncertainties is close to 1, indicating that the uncertainties are well modeled.

4. Normalize the masked science frames to the same average sky value.
5. Average the resulting frames to produce one combined image.
6. Normalize the combined image to a mean of unity, and take the multiplicative inverse.
7. Smooth the normalized combined image with a large kernel to the generate final illumination correction.
8. Multiply the dome flat with the illumination correction.

Mathematically, we can describe our final illumination correction, $I(t)$, as:

$$I = S_K\left(\left\langle \frac{F_S}{\langle F_D\rangle}\right\rangle^{-1}\right), \quad (8)$$

where S_K represents the smoothing kernel used in the stage, and angled braces denote the average. We bin each 1024 × 4096 pixels amplifier image by a factor of 4, and smooth the binned image with 30 × 30 pixels, before re-expanding the binned image to the original dimensions. This effective 120 pixel scale is larger than the small scale structures of the flat field, such as out-of-focus dust "donuts," while retaining the large-scale gradients that we seek to correct for. Finally, we construct a master illumination-corrected flat-field image, F_I, via

$$F_I(t) = F_D(t) \times I(t), \quad (9)$$

where I and F_D are normalized to an average value of 1.0, and we introduce t denotes the night of observation. The illumination-corrected flat-field image is used to flatten the science images from the night.

A.2. Temporal Stability of the Illumination Correction

We distinguish two types of changes affecting the optical system.

1. Global changes that affect all images, including new dust grains on the optics, changes in instrument mounting, and mechanical changes in the mirror support.
2. Flat field changes that only affect our dome flat images, including ghosting, non-uniformity of the flat-field screen, as well as instances where a flat-field lamp burnt out.

We examine the temporal stability of the illumination-corrected flat fields when subjected to both types of changes. From Equations (8) and (9), provided the global changes are small, the product $F_I(t)$ should not be sensitive to changes in the dome flats. We determine the ratios of dome flat, illumination correction, and illumination-corrected flat fields for all nights within an observing run. This is illustrated in Figure 19, where we compare frames between 20030927 and 20031020. The ratio of the illumination-corrected flat-field images is within 0.1% of unity, despite differences at the 0.5% level between the flat field and illumination correction frames. We calculate the standard deviation of the ratio images, as well as the maximum difference between the ratio image and the average of the ratio. Nights for which the standard deviation of the ratio is consistently >0.1%, or the maximum error of the ratio is consistently >0.3%, are flagged. Comparing our flagged nights to subjective observing logs for the nights, we find that flagged nights have excessive moonlight. This difference presumably arises from non-focusing light paths producing stray light illumination of the focal plane, with an intensity pattern different from the light path for focused celestial sources. We find that the illumination corrections degrade more rapidly toward full moon in *R* than *I*, and attribute this to the steeper gradients in the sky brightness in *R*. This temporal stability is exploited to estimate an illumination correction for flagged nights using other nights within the observing run. A 0.3% error is adopted as the systematic on the illumination-correction frames.

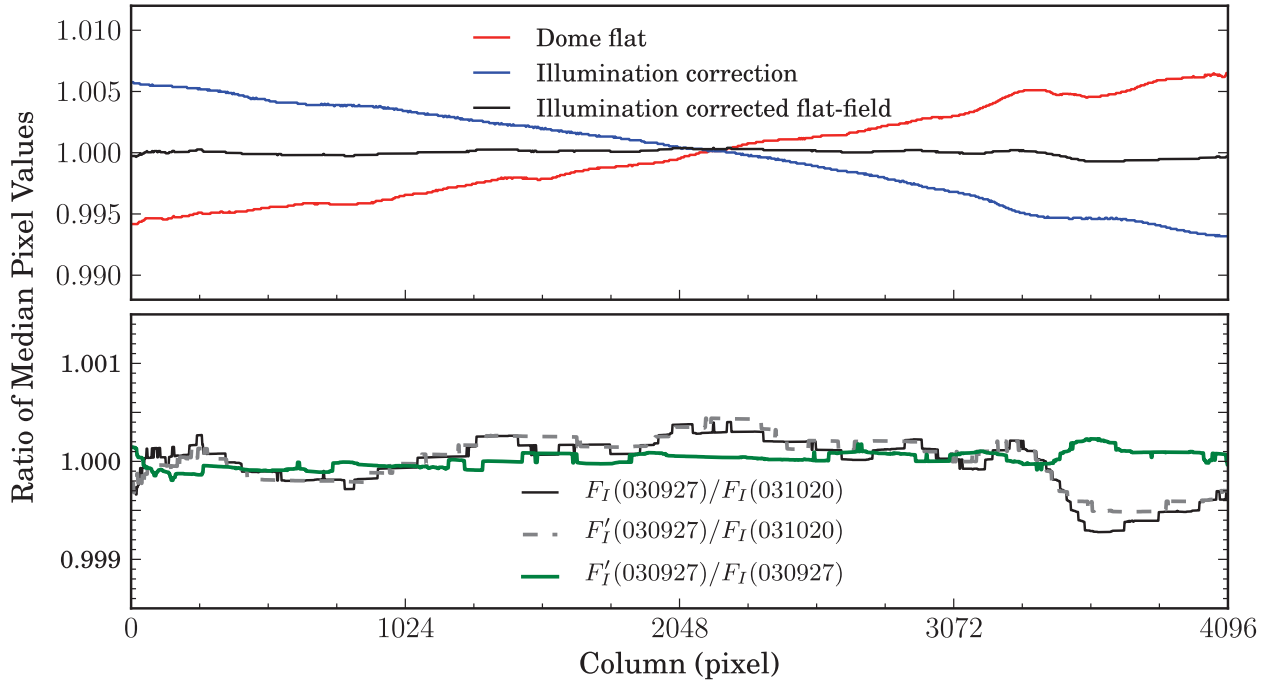

Figure 19. Illustration of the stability of the illumination corrections from 20030927 (randomly selected) and 20031020 (~1 month later). Top: The ratio of the dome flat frames is shown in red, while the ratio of the illumination correction frames is shown in blue. Both ratios indicate that there are differences at the ~0.5% level between these two nights. The ratio of the illumination-corrected flat field between the two nights, shown in black, is within 0.1% of unity, indicating that the illumination correction is accurately accounting for the variations in the dome flat images, despite being separated by almost a month. Bottom: The ratio of the illumination-corrected flat fields between 20030927 and 20031020 is again shown in black on a finer scale to illustrate the structure. We construct an estimated illumination correction for 20030927, F_I', using the flat and bias images from 20031020, and the science frames from 20030927. The ratio of the flat-field image processed with the estimated illumination correction and the illumination-corrected flat field for 20031020 is shown as a dashed gray line. The ratio of the derived and the estimated illumination-corrected flat fields on 20030927 is shown in green, and illustrates that the illumination-corrected flat fields are stable to better than 0.1% between the two dates.

APPENDIX B
PROPERTIES OF THE CTIO 4 M NATURAL SYSTEM

We describe the properties of the CTIO Blanco natural system in the following subsections. We derive the system transmission and compute synthetic color terms to the Landolt system. We use our determined transmission along with synthetic photometry of model SEDs to study the differences between our fundamental spectrophotometric standard, BD +17°4708, and "typical" Landolt stars at similar colors. Finally, we establish synthetic zero points to derive natural system magnitudes from flux-calibrated SEDs.

B.1. Transmission

We model the transmission, T, of the CTIO Blanco system by the product of four components: the atmosphere (Atm), optics (Opt), filter (PB), and the Quantum Efficiency of the MOSAIC II CCDs (QE).

$$T(\lambda) = T_{\rm Atm}(\lambda) \times T_{\rm Opt}(\lambda) \times T_{\rm PB}(\lambda) \times {\rm QE}(\lambda). \quad (10)$$

B.1.1. Detector Quantum Efficiency

The eight Tek CCDs that comprise the MOSAIC II have slightly different quantum efficiencies (listed in Table 8). However, we find the differences in synthetic photometry from using different quantum efficiency curves is <0.001 mag, for both R and I over a wide range of color. Consequently, we elect to use a single average value of the quantum efficiency for all the CCDs.

B.1.2. R and I Optical Filters

The MOSAIC II uses filters that are 146 × 146 mm and ~12 mm thick. The transmissions of the R (NOAO code c6004) and I filter (c6028) were measured by CTIO staff[39] using an OceanOptics S2000 spectrometer. The S2000 is a crossed Czerny-Turner spectrometer, configured with a 600 ln/mm grating, blazed at 750 nm, for measurements over 600–1200 nm. Measurements were obtained through a 10 μm wide slit coupled to a fiber optic with 400 μm core diameter. The resulting optical resolution is ~10 nm FWHM. The filters are illuminated with a General Electric 787 halogen lamp with quartz bulb, identical to those used to illuminate the Blanco flat-field screen, through a ground glass diffuser. The spectrum is projected onto a 1 × 2048 pixel CCD array and digitized. An OceanOptics HG-1 He–Ar lamp produces reference spectral features to determine the pixel-to-wavelength transformation. The transformation is modeled as a simple cubic polynomial. The central wavelength of the filters is shifted ~15 Å to the blue when mounted in the prime focus of the $f/2.87$ beam with ADC, relative to measurements at normal incidence. The shift is included in the provided transmission curve.

[39] http://www.ctio.noao.edu/noao/content/mosaic-filters

B.1.3. Telescope Optics

As the MOSAIC II is mounted at prime focus, the transmission of the optics is dominated by the wavelength-dependent reflectivity of the primary mirror, and is well modeled by the reflectivity of aluminium. The transmission of the ADC[40] was measured to above 85% in the range 3500-8500 Å. The transmission of the ADC does fall significantly in the ultraviolet, but this has no effect on our *RI* photometry. The drop off at the red end is very gradual and the transmission at 10000 Å is ∼75%.

B.1.4. Atmospheric Transmission

M07 used a model of the atmospheric transmission derived from observations of spectrophotometric standards, with the removal of telluric features. The resulting atmospheric model, while reasonably precise, depends on the standard used, and the details of the reduction, particularly on the fit of a smooth psuedocontinuum. We generate an atmospheric model using the `MODTRAN4` code. The generated atmosphere is appropriate for an airmass of 1, and consists of 2 mm PMW of water vapor at an altitude of 2 km, convolved with the atmospheric scattering function and the transmission from aerosols. The differences between our atmospheric model and that employed by M07 are primarily in the strength of the absorption features, with the largest differences on the red wing of the I band (>9500 Å). The differences result in an <0.001 mag change in synthetic colors over a wide range (note that the M07 transmission is provided in erg/Å and must be divided by λ for comparison with this work).

The total system throughput at an airmass of unity is listed in Table 9. Measurements of the system throughput using a tunable laser, calibrated to a NIST photodiode, were consistent with the product of each component (Stubbs et al. 2007). We could not measure the system throughput of the I filter (c6005) used very early in the survey and replaced after significant damage in 2002 November.

B.2. Synthetic Color Relations

We derive synthetic color terms between the CTIO natural system and the Landolt network using a procedure similar to that of Stritzinger et al. (2005). We approximate the Landolt passbands using the Cousins R_C and I_C transmissions published in Bessell (1990), convolved with a model atmosphere, and shifted in wavelength by a small amount $\Delta\lambda$. The shifts are determined by comparing the observed Landolt photometry of the non-variable standards in the spectral library of Stritzinger et al. (2005) to their synthetic photometry, and shifting the passbands, without shifting the atmospheric features, until the R and I synthetic and observed photometry agreed, with a color term consistent with zero in $V - R$, $V - I$, and $R - I$. We find that the R and I Bessell filters have to be *blueshifted* by 36 Å and 12 Å in R and I, respectively. Using our determination of the CTIO system throughput in Table 9, we compare synthetic photometry of the spectral library to synthetic photometry through the shifted Bessell passbands. We derive synthetic Landolt-to-CTIO color transformations, finding $c^R_{R-I}(\mathrm{Syn}) = -0.033$ and $c^I_{R-I}(\mathrm{Syn}) = 0.047$. The results of this analysis are presented in Figure 20.

[40] http://www.ctio.noao.edu/mosaic/manual/pfadc_paper.ps

The synthetic color term in R is in excellent agreement with the color term determined from photometric observations, but there is a significant discrepancy in I. A blueshift of ∼40 Å to the I Bessell transmission is required to reproduce the observed Landolt-to-CTIO color term in I, but a shift of this size introduces a non-zero $R - I$ color term between the observed and synthetic Landolt magnitudes. There is no wavelength shift for the Bessell determination of I, such that the synthetic and observed Landolt magnitudes and the synthetic CTIO and synthetic Landolt magnitudes simultaneously agree with non-zero color terms. Fundamentally, approximating the Landolt I passband by a shifted Bessell I filter is not accurate, as the shapes of these filters differ. Specifically, the transmission in the I band is significantly affected by the roll-off in the detector quantum efficiency, which is not included in the Bessell determination. The detector quantum efficiency is effectively constant over R, and therefore has an insignificant effect on the shape of the transmission. Current and future surveys observing in *griz* will be able to calibrate to photometric systems such as SDSS, Pan-STARRS, and SkyMapper, which have well-measured system responses.

B.3. The Magnitudes of BD+17°4708 in the CTIO Blanco Natural System

The transformations defined by Equation (4) are constructed such that, to first order, the natural system magnitudes of BD +17°4708 are equal to its Landolt magnitudes in R and I. However, since we could not observe BD+17°4708 directly, we determine the coefficients of the transformation equations using the Landolt network of stars. In this subsection, we quantify the difference in natural system magnitudes between BD+17°4708, and Landolt stars having $R - I$ color similar to it by:

$$\delta L_T = M_{4\,\mathrm{m}} - M_L - c^{M_{4\,\mathrm{m}}}_{(R-I)_L}((R-I)_L - 0.32). \quad (11)$$

By construction, the average residual $\langle \delta L \rangle = 0$ for average Landolt stars. Following Regnault et al. (2009), we consider the photometric residual arising from metallicty and surface gravity, extinction differences between BD+17°4708 and the average Landolt star, and consider the systematic effect of a possible faint, unresolved companion. The various effects considered are illustrated in Figure 21.

B.3.1. Metallicity and Surface Gravity

We determine the difference in synthetic R and I 4 m magnitudes residuals between BD+17°4708 and "typical" Landolt stars with metallicity, $[\mathrm{M/H}] = -0.5$ and $\log(g) = 4.0$ as a function of the difference in synthetic $R - I$ color, over $5600\,\mathrm{K} < T_{\mathrm{eff}} < 6500\,\mathrm{K}$. We find the relationship between the mean magnitude residual, and difference in $R - I$ color to be linear for both R and I. We determine the intercept at $R - I = 0.32$, and find (in the sense of BD+17°4708 mag *minus* Landolt mag) that $\delta L < 0.001$ mag for both R and I.

To measure the effect of surface gravity alone, we select synthetic SEDs with the same parameters as above, except at $\log(g) = 4.5$. We measure the difference in the residual to normal Landolt stars, δL_M, caused by perturbing the synthetic SEDs from $\log(g) = 4.0$ to $\log(g) = 4.5$. We find the effect of changing surface gravity on the difference in residual (in the sense of residual at $\log(g) = 4.5$ *minus* residual at $\log(g) = 4.0$) is $\delta L_R < 0.001$ mag, while $\delta L_I \approx +0.002$ mag.

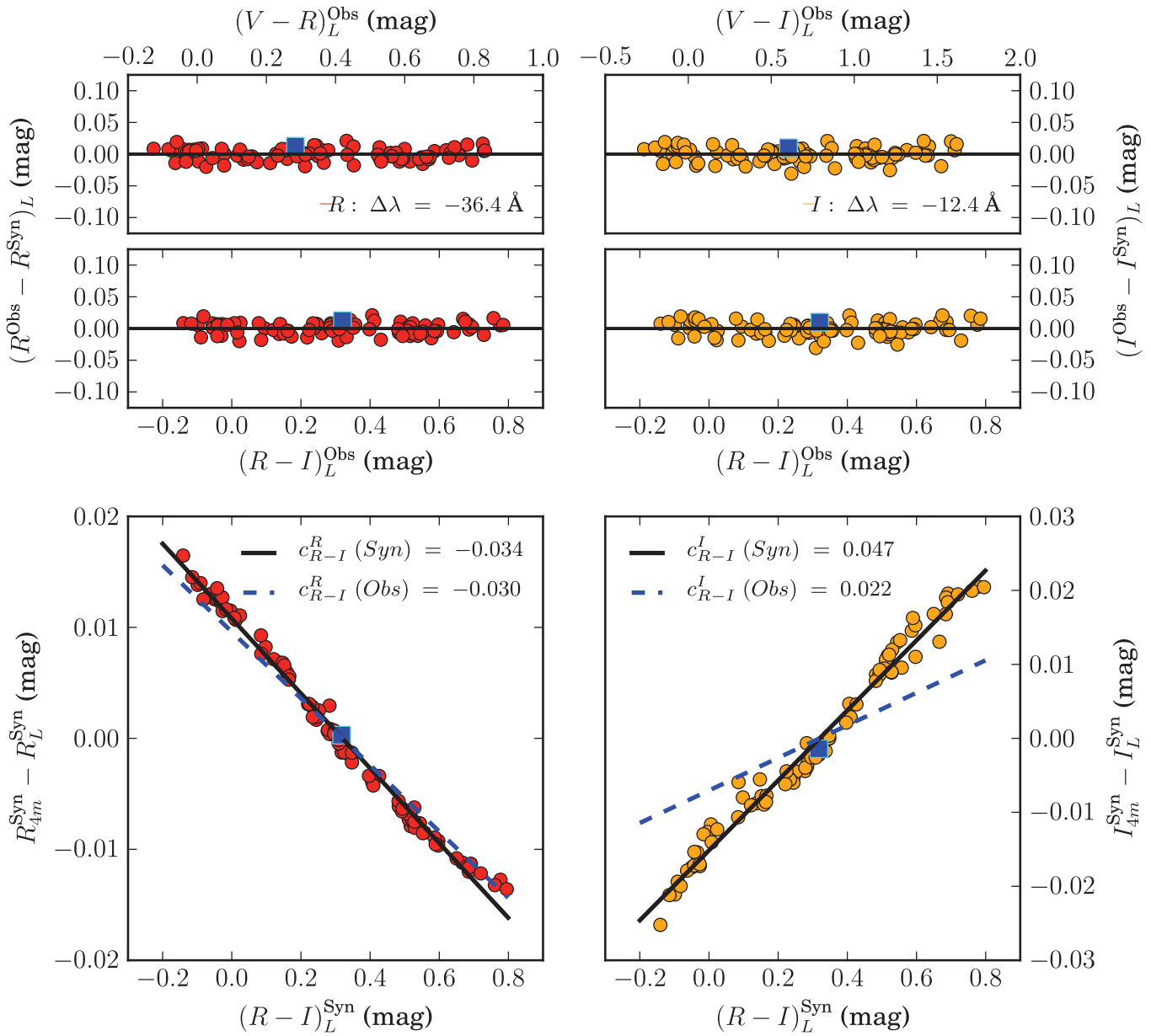

Figure 20. Top and middle: Residuals between observed (Obs) Landolt magnitudes and synthetic (Syn) magnitudes of 99 non-variable stars in the spectral library of Stritzinger et al. (2005) as a function of the observed Landolt color indicated for *R* (left panels) and *I* (right panels). The Landolt passbands are modeled by shifting the Bessell (1990) determinations in wavelength by $\Delta\lambda = -36$ Å and -12 Å in *R* and *I*, respectively. A solid black line at $\Delta M = 0$ is included as a visual guide. Bottom: Synthetic color transformations between our determination of the CTIO system throughput and the model Landolt system throughput for *R* (left) and *I* (right), respectively. The observed color relations from photometric measurements is indicated by dashed blue lines, while the best-fit relation to the synthetic photometry is indicated by a solid black line. There is excellent agreement in *R*. We believe that the disagreement in *I* is a result of not modeling the roll-off in the detector quantum efficiency for the model Landolt throughput. A blueshift of -40 Å is sufficient to recover the observed Landolt-to-CTIO color term in *I*, but introduces a small color term between the observed and synthetic Landolt measurements in $R - I$. The observed and synthetic photometry of BD+17°4708, using the CALSPEC SED, is indicated by a blue square in all the plots. There is a ∼1% offset between the flux calibration of the CALSPEC BD+17°4708 SED, and the mean flux calibration of the Stritzinger et al. (2005) spectral library.

The combined effect of metallicity and surface gravity leads to a negligible difference in *R* and a net δL_I of ∼0.001 mag.

B.3.2. Extinction

Regnault et al. (2009) express the distance of BD+17°4708 from the stellar locus in $V - R$, $R - I$ in terms of the effect of the difference in extinction and the difference in metallicity (the effect of surface gravity being negligible over the color range in question). Having determined the effect of a difference in metallicity using a procedure similar to that above, they found the difference in the reddening between BD+17°4708 and Landolt stars of similar color to be $\Delta E\,(B - V) \sim 0.045$ mag.

We redden the synthetic SED of BD+17°4708 by this amount, and examine the difference in the residual to normal Landolt stars (in the sense of residual with reddened SED *minus* residual with un-reddened SED) to be less than 0.001 mag in *R* and ≈0.001 mag in *I*.

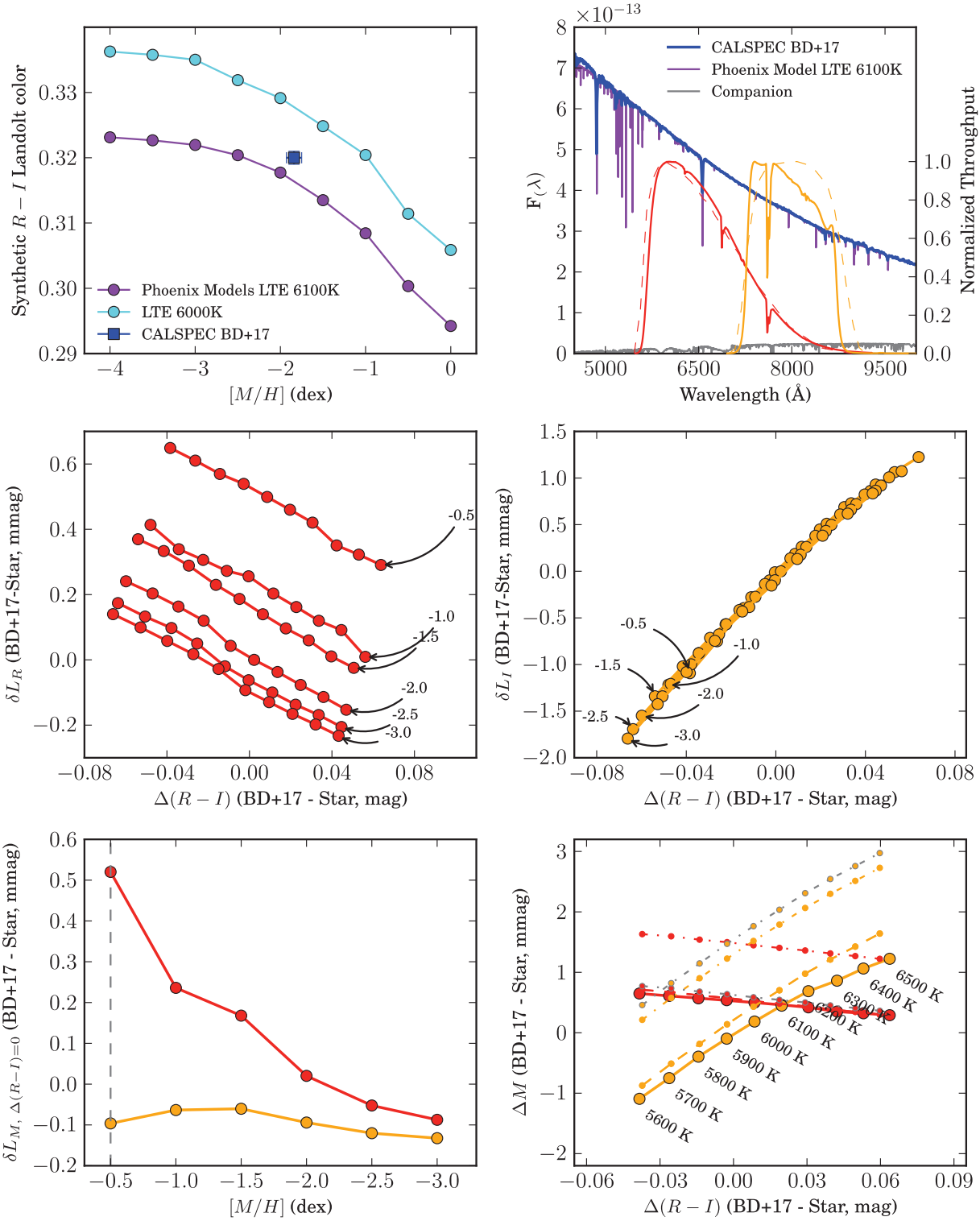

Figure 21. Synthetic magnitudes of BD+17° 4708 in the CTIO Blanco Natural System. Top left: Synthetic colors of Phoenix SEDs as a function of metallicity, compared to the synthetic color of the CALSPEC SED of BD+17°4708. The best model has $T_{\rm eff}$ = 6100 K and [M/H] = −2.0 dex. Top right: Comparison of the CALSPEC SED and the adopted Phoenix model. The adopted model for the companion of BD+17°4708 has $T_{\rm eff}$ = 3000 K and [M/H] = −2.0 dex. Normalized CTIO Blanco (solid) and Bessell (dashed) transmissions in *R* (red) and *I* (orange) are shown for comparison. Middle: Difference in photometric residual, δL, (in the sense of BD+17 mag *minus* Landolt mag ($T_{\rm eff}$, [M/H])) over a range of temperature and metallicity for *R* (mid left) and *I* (mid right) vs. the difference in $R-I$ color (in the sense of BD+17 color *minus* Landolt color). The effect of changing metallicity is negligible in *I*. Bottom left: The values of δL at $\Delta(R-I)=0$ for the different metallicities. The typical metallicity of Landolt stars ([M/H] = −0.5 dex) is indicated by the vertical line. Bottom right: Deviations from the relation of δL at [M/H] = −0.5 dex are shown for changes in surface gravity (dashed), extinction (dot–dashed), and the addition of a companion (dot–dashed gray) for *R* (red) and *I* (orange).

The combined effect of the difference in metallicity, surface gravity, and extinction is found to be $\delta L_R = 0.001$ mag and $\delta L_I = 0.002$ mag. These offsets are added to the first order estimates of the magnitudes of BD+17°4708.

B.3.3. Binarity

Using the estimates from Ramírez et al. (2006) for the companion of BD+17°4708 ($T_{\rm eff} = 3000k$, $\log(g) = 4.5$, and $[{\rm M/H}] = -2$), we compute the difference in photometric residuals and find (in the sense of with companion *minus* without companion) than $\delta L_{R,I} \approx 0.001$ mag. As we do not know the fraction of Landolt stars that are also in binaries, we treat these offsets as systematic errors.

B.4. Photometric Zero Points

With the Landolt magnitudes of BD+17°4708 ($R = 9.166$ mag and $I = 8.846$ mag) and the photometric residuals caused by the differences in metallicity, surface gravity, and extinction to typical Landolt stars computed in the previous subsection, we invert Equation (3) to derive synthetic passband zero points for R and I and find:

$$\begin{aligned} {\rm ZP}_{R_{4\,\rm m}} &= -21.649 \pm 0.001 \text{ mag} \\ {\rm ZP}_{I_{4\,\rm m}} &= -22.305 \pm 0.002 \text{ mag}. \end{aligned} \quad (12)$$

These values differ from the values determined using the Stritzinger et al. (2005) SED library by 0.012 mag. This discrepancy is likely the result of a difference in flux calibration between CALSPEC and Stritzinger et al. (2005), as illustrated in Figure 20. We use the CALSPEC SED of BD+17°4708 for the determination of passband zero points, as its flux calibration is not affected by atmospheric transmission, and has been carefully studied by several groups.

B.5. Differences in Natural System Definition to the Four-year Data Release

M07 tied the natural system of the Blanco to Landolt using α Lyr as their fundamental standard, with $(R-I)_{\rm Landolt} = 0$. In addition, a slightly steeper c^I_{R-I} color term was employed in that work, and we expect a difference on the order of the product of difference of the color terms, and the average color of Landolt stars, $\langle (R-I)_{\rm Landolt} \rangle$.

To first order, the differences between the photometry of stars in this work and M07 are the result of the differences between the *definition* of the photometric system in Equation (4) and the M07 definition:

$$\begin{aligned} \Delta R &\approx c^R_{R-I} \times (R-I)_{\rm BD+17} \\ &\approx -0.030 \times 0.32 \\ &\approx -0.01 \text{ mag} \\ \Delta I &\approx c^I_{R-I} \times (R-I)_{\rm BD+17} \\ &\quad + \Delta c^I_{R-I} \times (\langle (R-I)_{\rm Landolt} \rangle - (R-I)_{\rm BD+17}) \\ &\approx (0.030 \times 0.32) - 0.008 \times (0.47 - 0.32) \\ &\approx 0.009 \text{ mag}. \end{aligned} \quad (13)$$

However, we have taken various measures to improve the calibration of the natural system, with a view to minimizing our overall photometric error budget, as discussed is Section 3. Consequently, the methodology used in this paper differs substantially from that used by M07. In particular, this work uses observations of the ESSENCE fields tied directly to Landolt fields, whereas M07 tied the Blanco photometry to 0.9 m observations of field stars, that were in turn tied to Landolt. This is a potential source of additional differences above the expected 1% level.

REFERENCES

Abazajian, K. N., Adelman-McCarthy, J. K., Agüeros, M. A., et al. 2009, ApJS, 182, 543
Albert, J., Brown, Y., Stubbs, C., et al. 2014, in American Astronomical Society Meeting Abstracts 224, 40501
Albrecht, A., Bernstein, G., Cahn, R., et al. 2006, arXiv:astro-ph/0609591
Allington-Smith, J., Breare, M., Ellis, R., et al. 1994, PASP, 106, 983
Appenzeller, I., Fricke, K., Fürtig, W., et al. 1998, The ESO Messenger, 94, 1
Astier, P., Guy, J., Regnault, N., et al. 2006, A&A, 447, 31
Barone-Nugent, R. L., Lidman, C., Wyithe, J. S. B., et al. 2012, MNRAS, 425, 1007
Barris, B. J., Tonry, J. L., Novicki, M. C., & Wood-Vasey, W. M. 2005, AJ, 130, 2272
Bertin, E., Mellier, Y., Radovich, M., et al. 2002, in ASP Conf. Ser. 281, Astronomical Data Analysis Software and Systems XI, ed. D. A. Bohlender, D. Durand, & T. H. Handley (San Francisco, CA: ASP), 228
Bessell, M. S. 1990, PASP, 102, 1181
Betoule, M., Kessler, R., Guy, J., et al. 2014, A&A, 568, A22
Betoule, M., Marriner, J., Regnault, N., et al. 2013, A&A, 552, A124
Blondin, S., & Tonry, J. L. 2007, ApJ, 666, 1024
Blondin, S., Mandel, K. S., & Kirshner, R. P. 2011, A&A, 526, A81
Blondin, S., Walsh, J. R., Leibundgut, B., & Sainton, G. 2005, A&A, 431, 757
Bohlin, R. C. 2014, AJ, 147, 127
Bohlin, R. C., Gordon, K. D., & Tremblay, P.-E. 2014, PASP, 126, 711
Conley, A., Guy, J., Sullivan, M., et al. 2011, ApJS, 192, 1
Conley, A., Sullivan, M., Hsiao, E. Y., et al. 2008, ApJ, 681, 482
Contreras, C., Hamuy, M., Phillips, M. M., et al. 2010, AJ, 139, 519
Davis, T. M., Mörtsell, E., Sollerman, J., et al. 2007, ApJ, 666, 716
Dressler, A. 2004, A User's Manual for IMACS
Faber, S. M., Phillips, A. C., Kibrick, R. I., et al. 2003, Proc. SPIE, 4841, 1657
Fernie, J. D. 1981, PASP, 93, 333
Filippenko, A. V. 1997, ARA&A, 35, 309
Fischler, M. A., & Bolles, R. C. 1981, Commun. ACM, 24, 381
Folatelli, G., Phillips, M. M., Burns, C. R., et al. 2010, AJ, 139, 120
Foley, R. J., & Kasen, D. 2011, ApJ, 729, 55
Foley, R. J., Filippenko, A. V., Kessler, R., et al. 2012, AJ, 143, 113
Foley, R. J., Matheson, T., Blondin, S., et al. 2009, AJ, 137, 3731
Freedman, W. L., Burns, C. R., Phillips, M. M., et al. 2009, ApJ, 704, 1036
Fukugita, M., Ichikawa, T., Gunn, J. E., et al. 1996, AJ, 111, 1748
Ganeshalingam, M., Li, W., Filippenko, A. V., et al. 2010, ApJS, 190, 418
Garg, A., Stubbs, C. W., Challis, P., et al. 2007, AJ, 133, 403
Goldhaber, G., Groom, D. E., Kim, A., et al. 2001, ApJ, 558, 359
Guy, J., Astier, P., Baumont, S., et al. 2007, A&A, 466, 11
Guy, J., Sullivan, M., Conley, A., et al. 2010, A&A, 523, A7
Hamuy, M., Maza, J., Phillips, M. M., et al. 1993, AJ, 106, 2392
Hamuy, M., Phillips, M. M., Suntzeff, N. B., et al. 1996, AJ, 112, 2391
Hauschildt, P. H., Baron, E., & Allard, F. 1997, ApJ, 483, 390
Hayes, D. S., & Latham, D. W. 1975, ApJ, 197, 593
Hicken, M., Challis, P., Jha, S., et al. 2009b, ApJ, 700, 331
Hicken, M., Challis, P., Kirshner, R. P., et al. 2012, ApJS, 200, 12
Hicken, M., Wood-Vasey, W. M., Blondin, S., et al. 2009a, ApJ, 700, 1097
Hook, I., Allington-Smith, J. R., Beard, S. M., et al. 2003, Proc. SPIE, 4841, 1645
Horne, K. 1986, PASP, 98, 609
Ivezić, Ž., Smith, J. A., Miknaitis, G., et al. 2007, AJ, 134, 973
Jha, S., Kirshner, R. P., Challis, P., et al. 2006, AJ, 131, 527
Jha, S., Riess, A. G., & Kirshner, R. P. 2007, ApJ, 659, 122
Johnson, H. L., & Morgan, W. W. 1953, ApJ, 117, 313
Kelly, B. C. 2007, ApJ, 665, 1489
Kelly, P. L., Hicken, M., Burke, D. L., Mandel, K. S., & Kirshner, R. P. 2010, ApJ, 715, 743
Kessler, R., Becker, A. C., Cinabro, D., et al. 2009, ApJS, 185, 32
Krisciunas, K., Bastola, D., Espinoza, J., et al. 2013, AJ, 145, 11
Krisciunas, K., Hastings, N. C., Loomis, K., et al. 2000, ApJ, 539, 658

Krisciunas, K., Phillips, M. M., & Suntzeff, N. B. 2004, ApJL, 602, L81
Lampeitl, H., Smith, M., Nichol, R. C., et al. 2010, ApJ, 722, 566
Landolt, A. U. 1983, AJ, 88, 439
Landolt, A. U. 1992, AJ, 104, 340
Landolt, A. U., & Uomoto, A. K. 2007, AJ, 133, 768
Maguire, K., Sullivan, M., Ellis, R. S., et al. 2012, MNRAS, 426, 2359
Mandel, K. S., Narayan, G., & Kirshner, R. P. 2011, ApJ, 731, 120
Mandel, K. S., Wood-Vasey, W. M., Friedman, A. S., & Kirshner, R. P. 2009, ApJ, 704, 629
Matheson, T., Blondin, S., Foley, R. J., et al. 2005, AJ, 129, 2352
Miknaitis, G., Pignata, G., Rest, A., et al. 2007, ApJ, 666, 674
Nordin, J., Östman, L., Goobar, A., et al. 2011, ApJ, 734, 42
O'Donnell, J. E. 1994, ApJ, 422, 158
Oke, J. B., Cohen, J. G., Carr, M., et al. 1995, PASP, 107, 375
Oke, J. B., & Schild, R. E. 1970, ApJ, 161, 1015
Padmanabhan, N., Schlegel, D. J., Finkbeiner, D. P., et al. 2008, ApJ, 674, 1217
Perlmutter, S., Aldering, G., Goldhaber, G., et al. 1999, ApJ, 517, 565
Peterson, D. M., Hummel, C. A., Pauls, T. A., et al. 2006, Natur, 440, 896
Phillips, M. M. 1993, ApJL, 413, L105
Phillips, M. M., Lira, P., Suntzeff, N. B., et al. 1999, AJ, 118, 1766
Prieto, J. L., Rest, A., & Suntzeff, N. B. 2006, ApJ, 647, 501
Ramírez, I., Allende Prieto, C., Redfield, S., & Lambert, D. L. 2006, A&A, 459, 613
Regnault, N., Conley, A., Guy, J., et al. 2009, A&A, 506, 999
Rest, A., Scolnic, D., Foley, R. J., et al. 2014, ApJ, 795, 44
Rest, A., Stubbs, C., Becker, A. C., et al. 2005, ApJ, 634, 1103
Riess, A. G., Filippenko, A. V., Challis, P., et al. 1998, AJ, 116, 1009
Riess, A. G., Kirshner, R. P., Schmidt, B. P., et al. 1999, AJ, 117, 707
Riess, A. G., Press, W. H., & Kirshner, R. P. 1996, ApJ, 473, 88
Riess, A. G., Strolger, L.-G., Casertano, S., et al. 2007, ApJ, 659, 98
Sako, M., Bassett, B., Becker, A. C., et al. 2014, arXiv:1401.3317
Schechter, P. L., Mateo, M., & Saha, A. 1993, PASP, 105, 1342
Schlafly, E. F., Finkbeiner, D. P., Jurić, M., et al. 2012, ApJ, 756, 158
Schlegel, D. J., Finkbeiner, D. P., & Davis, M. 1998, ApJ, 500, 525
Schmidt, G. D., Weymann, R. J., & Foltz, C. B. 1989, PASP, 101, 713
Scolnic, D., Rest, A., Riess, A., et al. 2014b, ApJ, 795, 45
Scolnic, D. M., Riess, A. G., Foley, R. J., et al. 2014a, ApJ, 780, 37
Sheinis, A. I., Bolte, M., Epps, H. W., et al. 2002, PASP, 114, 851
Silverman, J. M., Ganeshalingam, M., Li, W., & Filippenko, A. V. 2012, MNRAS, 425, 1889
Sordo, R., Vallenari, A., Tantalo, R., et al. 2010, Ap&SS, 328, 331
Stetson, P. B. 2000, PASP, 112, 925
Stetson, P. B. 2005, PASP, 117, 563
Stritzinger, M. D., Phillips, M. M., Boldt, L. N., et al. 2011, AJ, 142, 156
Stritzinger, M., Suntzeff, N. B., Hamuy, M., et al. 2005, PASP, 117, 810
Stubbs, C. W., Doherty, P., Cramer, C., et al. 2010, ApJS, 191, 376
Stubbs, C. W., Slater, S. K., Brown, Y. J., et al. 2007, in ASP Conf. Ser. 364, The Future of Photometric, Spectrophotometric and Polarimetric Standardization, ed. C. Sterken (San Francisco, CA: ASP), 373
Stubbs, C. W., & Tonry, J. L. 2006, ApJ, 646, 1436
Sullivan, M., Conley, A., Howell, D. A., et al. 2010, MNRAS, 406, 782
Taylor, B. J. 1986, ApJS, 60, 577
Tonry, J., & Davis, M. 1979, AJ, 84, 1511
Tonry, J. L., Stubbs, C. W., Lykke, K. R., et al. 2012, ApJ, 750, 99
Tucker, D. L., Annis, J. T., Lin, H., et al. 2007, in ASP Conf. Ser. 364, The Future of Photometric, Spectrophotometric and Polarimetric Standardization, ed. C. Sterken (San Francisco, CA: ASP), 187
Walker, E. S., Hook, I. M., Sullivan, M., et al. 2011, MNRAS, 410, 1262
Wang, X., Filippenko, A. V., Ganeshalingam, M., et al. 2009, ApJL, 699, L139
Wood-Vasey, W. M., Friedman, A. S., Bloom, J. S., et al. 2008, ApJ, 689, 377
Wood-Vasey, W. M., Miknaitis, G., Stubbs, C. W., et al. 2007, ApJ, 666, 694
Zacharias, N., Urban, S. E., Zacharias, M. I., et al. 2004, AJ, 127, 3043